ANALYSIS OF BOUNDARY-LAYER INSTABILITIES IN HYPERSONIC, THREE-DIMENSIONAL FLOWS

A Dissertation

by

ANDREW KELLY RIHA

Submitted to the Graduate and Professional School of
Texas A&M University
in partial fulfillment of the requirements for the degree of

DOCTOR OF PHILOSOPHY

Chair of Committee,	Helen Reed
Committee Members,	Rodney Bowersox
	Edward White
	Freddie Witherden
Head of Department,	Ivett Leyva

December 2022

Major Subject: Aerospace Engineering

ABSTRACT

Spatial BiGlobal (SBG) theory was used to study boundary-layer transition on a hypersonic finned cone. A new solver, BLAST, has been developed to apply the equations in a nonorthogonal manner, which extends its applicability to realistic flight vehicles. After verification of the code with previous literature, it was applied to the finned cone at conditions corresponding to quiet wind-tunnel experiments. Boundary-layer instabilities in a horseshoe vortex emanating from the fin-cone intersection are the focus of this study.

Through this investigation, opportunities for improvement were identified regarding SBG and its interpretation. Specifically, the definition of the N factor was used to account for general-group velocity directions. The nonorthogonal equations were used to decouple the orientation of the stability grid from the direction of minimum basic-state change, which allows more control over the most important assumption inherent in spatial BiGlobal. This formulation also allowed computation of the first SBG results to fully include a geometric feature like a full fin in its domain, which is found to be necessary to achieve accurate solutions. The effects of other choices were examined as well, such as the inclusion of streamwise curvature, placement of the azimuthal boundaries, and choice of growth direction. Best practices are developed and discussed.

SBG results are compared with experiments where possible, with particularly good agreement found for a laminar experimental condition at Mach 6 and $Re' = 5.9 \times 10^6$ m^{-1}. The correct frequencies are predicted as most-amplified in different regions of the vortex, with the hand-off from one dominant frequency to the other also correctly reproduced computationally. Features of these instabilities are identified, along with their characteristics and how they are affected by the basic state.

ACKNOWLEDGMENTS

I have had so many amazing people help me to get to where I am today. I would like to thank Professor Helen Reed for her unwavering support. Since I first started working with her, she has never missed an opportunity to share her knowledge and thought processes, and has patiently listened to and worked through my questions and ideas. Her guidance and ability to see different perspectives has made me a better engineer, and given me tools that will I use in all of my work moving forward. I am in her debt for changing the trajectory of my professional career and introducing me to so many new people and opportunities. I would also like to thank the other members of my committee: Profs. Rodney Bowersox, Edward White, and Freddie Witherden. I was able to take your classes or work with you in a research setting, and I have taken away lessons that were directly used in my dissertation research and will continue to be used elsewhere.

To my mom, my dad, and my brother Zachary: I could not have done this without you. You have believed in me every step of the way for my entire life. You helped me to celebrate the little milestones, encouraged me during the rough patches, and helped me keep everything in perspective as to what is most important. My aunts, uncles, and grandparents have also played an pivotal role in supporting me along the way. I have the most incredible family.

I would like to thank Madeline Peck for her invaluable help with BLAST. The code would not be in the state it is today without your contributions, and I would likely have spent much more time chasing bugs. Thank you to Ethan Beyak for humoring my incessant math and Fortran questions, and for assisting with my code as well. Thank you to Alex Moyes and Travis Kocian, who helped get me up to speed in the lab when I did not know the first thing about boundary-layer stability. A special thank you goes to Pedro Paredes for openly sharing his knowledge and experiences. You gave excellent technical advice at critical junctures in my research that was very helpful. Thank you to all the other past members of the Computational Stability and Transition lab: Daniel Mullen, Koen Groot, Danny Heston, and Jay Patel. You all made the lab a fun place to work hard and provided friendships outside of it as well. And last but not least, thank you to Kristofer Rice

and Andrea Lloyd for being excellent friends for many years. You both helped me stay sane, have some fun along the way, and make it to the finish line.

CONTRIBUTORS AND FUNDING SOURCES

Contributors

This work was supported by a dissertation committee consisting of Professors Helen Reed, Rodney Bowersox, and Edward White of the Department of Aerospace Engineering and Professor Freddie Witherden of the Department of Ocean Engineering.

Madeline Peck assisted with the basic-state and stability calculations in section 4.2.1, and provided the basic states in Chapters 5 and 6. Madeline Peck and Ethan Beyak also contributed code to BLAST, particularly in the nonorthogonal sections. All other work conducted for the dissertation was completed by the student independently.

Funding Sources

This work is supported by the Office of Naval Research under ONR grants N00014-16-1-2434 and N00014-19-1-2500 with Program Manager Eric Marineau. The author is grateful to Pointwise for providing the mesh software and to NASA for providing DPLR. Portions of this research were conducted with the advanced computing resources provided by Texas A&M High Performance Research Computing. The author also acknowledges the Texas Advanced Computing Center at The University of Texas at Austin for providing HPC and storage resources that have contributed to the research results reported within this paper.

NOMENCLATURE

Abbreviations

(1, 2, 3)-D	(One, Two, Three)-Dimensional
BAM6QT	Boeing/AFOSR Mach-6 Quiet Tunnel
BLAST	Boundary Layer Analysis using Surface Techniques
BOLT	Boundary-Layer Transition
CFD	Computational Fluid Dynamics
COO	Coordinate format
DPLR	Data-Parallel Line Relaxation
DNS	Direct Numerical Simulation
GICM	Groot–Illingworth–Chebyshev–Malik
HIFiRE	Hypersonic International Flight Research Experimentation
HPC	High Performance Computing
HyTRV	Hypersonic Transition Research Vehicle
(L, N)PSE	(Linear, Nonlinear) Parabolized Stability Equations
LST	Linear Stability Theory
MUSCL	Monotonic Upstream Schemes for Conservation Laws
NASA	National Aeronautics and Space Administration
ODE	Ordinary Differential Equation
ONR	Office of Naval Research
PDE	Partial Differential Equation
RMS	Root-Mean-Square
SBG	Spatial BiGlobal

TAMU	Texas A&M University

Variables

$\boldsymbol{0}$	Zero matrix
A	Amplitude of perturbation
	Amplification function
(a, b, c)	First, second, and third coordinates of a computational coordinate system
$(\boldsymbol{a}_\xi, \boldsymbol{a}_\eta, \boldsymbol{a}_\zeta)$	Basis vectors for a nonorthogonal coordinate system
$\boldsymbol{\mathcal{A}}$–$\boldsymbol{\mathcal{F}}$	SBG equation matrices
$(\boldsymbol{b}_\chi, \boldsymbol{b}_r, \boldsymbol{b}_\Theta)$	Basis vectors for a cylindrical coordinate system
C	Cartesian coordinate frame
c	Coefficient
c_{BL}	Edge of $\tanh$ function
c_p	Specific heat at constant pressure
c_{ph}	Phase speed
c_v	Specific heat at constant volume
$c.c.$	Complex conjugate
$\boldsymbol{c}$	Curve vector
$(\boldsymbol{e}_x, \boldsymbol{e}_y, \boldsymbol{e}_z)$	Basis vectors for an orthogonal coordinate system
Ec	Eckert number
$\boldsymbol{F_{NR}}$	Newton–Raphson vector
$\boldsymbol{f_{NR1}}, f_{NR2}$	Parts of Newton–Raphson vector
g	Metric tensor
h	Scale factors in an orthogonal coordinate system
	Spacing between grid points along a coordinate

$\boldsymbol{\mathcal{H}}$	Hessenberg matrix
$\boldsymbol{\mathcal{I}}$	Identity matrix
$\boldsymbol{\mathcal{I}}^{\dagger}$	Partial identity matrix
$\left(\hat{\boldsymbol{\imath}}, \hat{\boldsymbol{\jmath}}, \hat{\boldsymbol{k}}\right)$	Unit basis vectors for a body-fitted coordinate system (Chapter 2)
	Unit basis vectors for the Cartesian frame (Chapters 3–7)
J	Determinant of the Jacobian
	Joules
J_j^i	Jacobian
$\boldsymbol{\mathcal{J}_{NR}}$	Jacobian matrix for Newton–Raphson algorithm
K	Kelvin
k	Thermal conductivity
kg	Kilograms
kHz	Kilohertz
$\boldsymbol{k}$	Wave vector
L	Length scale
M	Mach number
m	Meters
m_1, m_2	Coefficients in algebraic clustering scheme
$\boldsymbol{\mathcal{M}_1}, \boldsymbol{\mathcal{M}_2}$	SBG generalized-eigenvalue-problem matrices
N	N factor
	Nonorthogonal reference frame
	Newtons
n_{Approx}	Order of approximation of finite difference
$n_{Arnoldi}$	Number of Arnoldi iterations
n_{Order}	Order of derivative of finite difference

n_y, n_z	Number of points used in the second and third coordinates, respectively
$\boldsymbol{n}$	Normal vector
O	Orthogonal reference frame
p	Pressure
Pr	Prandtl number
R	Specific gas constant
	Cylindrical reference frame
	Radius of curvature
Re	Reynolds number
Re'	Unit Reynolds number
S	Sutherland's constant
	Surface function
s	Seconds
	Distance along a curve
T	Temperature
	Computational coordinate frame
t	Time
u, v, w	First, second, and third components of velocity
$\boldsymbol{v}_g$	Group-velocity vector
(X, Y, Z)	First, second, and third coordinates of an inertial Cartesian coordinate system
(x, y, z)	First, second, and third coordinates of a body-fitted orthogonal coordinate system
Y_Δ, Z_Δ	Distortion parameters
α	Angular wavenumber and growth rate along first coordinate

β	Angular wavenumber and growth rate along second coordinate
Γ	Christoffel symbol of the second kind
γ	Ratio of specific heats
$\Delta\eta$, $\Delta\zeta$	Discrete distance along a dimension
δ	Kronecker-Delta tensor
ϵ	Levi-Civita tensor (absolute)
ε	Relative error
θ	Phase function
θ_g	Angle between group-velocity vector and first-coordinate direction
λ	Bulk viscosity
	Wavelength
λ_{Buffer}, λ_{Max}, λ_{Ramp}, λ_1–λ_4	Variables in buffer function
μ	Dynamic viscosity
ν	Kinematic viscosity
(ξ, η, ζ)	First, second, and third coordinates in a body-fitted orthonormal coordinate system (Chapter 2)
	First, second, and third coordinates in a general nonorthogonal coordinate system (Chapters 3–7)
ρ	Density
$\boldsymbol{\sigma}$	Growth vector
Φ	Energy dissipation term
ϕ	General quantity
$\mathbf{\Phi}$	Perturbation vector for generalized eigenvalue problem
$\boldsymbol{\phi}$	Perturbation vector
(χ, r, Θ)	First, second, and third coordinates in a cylindrical coordinate system

ω	Angular frequency
ω_h	Wavenumber based on grid spacing
ω_{relax}	Relaxation factor
$\in$	Contained in
$\mathbb{C}$	Complex numbers

Operators

∂	Partial derivative
d	Total derivative
∇	Gradient operator
$\cdot$	Dot (inner) product
:	Double inner product
$\times$	Cross (outer) product
	Multiplication
Σ	Summation
$\lvert\ \rvert$	Magnitude
$\Im$	Imaginary part

Accents

$\bar{}$	Basic-state quantity
$\hat{}$	Eigenfunction quantity
	Unit version of vector
$\breve{}$	Physical component
$\tilde{}$	Discretized form
$\breve{}$	Filtered quantity

Superscripts

$'$	Perturbation quantity
	Derivative
$*$	Dimensional quantity
T	Transpose

Subscripts

0	Initial
C	Cartesian frame component
c	Clustering height
e	Edge height
FD	Finite difference
$Filter$	Filter
$Guess$	Guess in convergence algorithm
i	Imaginary part
L	Left
Max	Maximum
N	Nonorthogonal frame component
O	Orthogonal frame component
$Orth$	Distribution from orthogonal grid
R	Cylindrical frame component
	Right
r	Real part
ref	Reference quantity
S	Constant in Sutherland's formula
	Surface

$Shift$	Related to shift-and-invert algorithm
$Stencil$	Related to location within finite-difference stencil
t	True

TABLE OF CONTENTS

Page

LIST OF FIGURES

FIGURE Page

LIST OF TABLES

TABLE Page

1. INTRODUCTION

Boundary-layer transition is a very active area of research that has the potential for large payoffs in the aerospace industry. Turbulent boundary layers can have significantly increased viscous drag and heat transfer into the wall. They also have increased efficiency in mixing fluids, and a higher resistance to separation in adverse pressure gradients. These characteristics of turbulence make control of transition a desirable tool, but one that has remained largely out of reach. This research aims to help continue the maturation of transition-prediction methodologies so that the goal of controllable boundary-layer transition can eventually be achieved.

Considerable effort has been put into categorizing the different types of transition seen in experiments. A series of pathways were identified and presented in their current form by Morkovin et al. [1]. They are typically presented as shown in figure 1.1. Five different pathways are available, and the amplitude of initial disturbances help to determine which one is followed. These disturbances can take different forms; typical examples include acoustic waves, vortical disturbances, thermal fluctuations, and wall roughness. The disturbance environment has been shown to be low enough in flight that boundary-layer transition will most often be dominated by paths A–C [2]. This work is concerned with path A, where small disturbances cause exponential growth of modal instabilities. Initial growth is linear in the sense that different perturbations neither affect each other nor the mean laminar flow. Once the disturbance has amplified enough, nonlinear interactions will occur that distort the flow, and lead either to secondary disturbances or directly to breakdown. Here, transition can be investigated by understanding the primary or secondary disturbances and their growth. If a disturbance mechanism can be identified, then this knowledge can then be used to delay or induce transition. For instance, the stationary-crossflow instability is very common in three-dimensional (3-D) boundary layers. It manifests as co-rotating vortices aligned with the freestream that grow and significantly distort the boundary layer. Once secondary instabilities on these vortices become unstable, the boundary layer will soon transition to turbulence. Through experiments by Saric et al. [3] and computations by Haynes & Reed [4], it has been proven that by

inciting a different wavelength to grow than that which is most amplified, boundary-layer transition can be delayed. This level of control of transition is currently limited to certain instabilities, and more information is needed to inform strategies for more complex flow features.

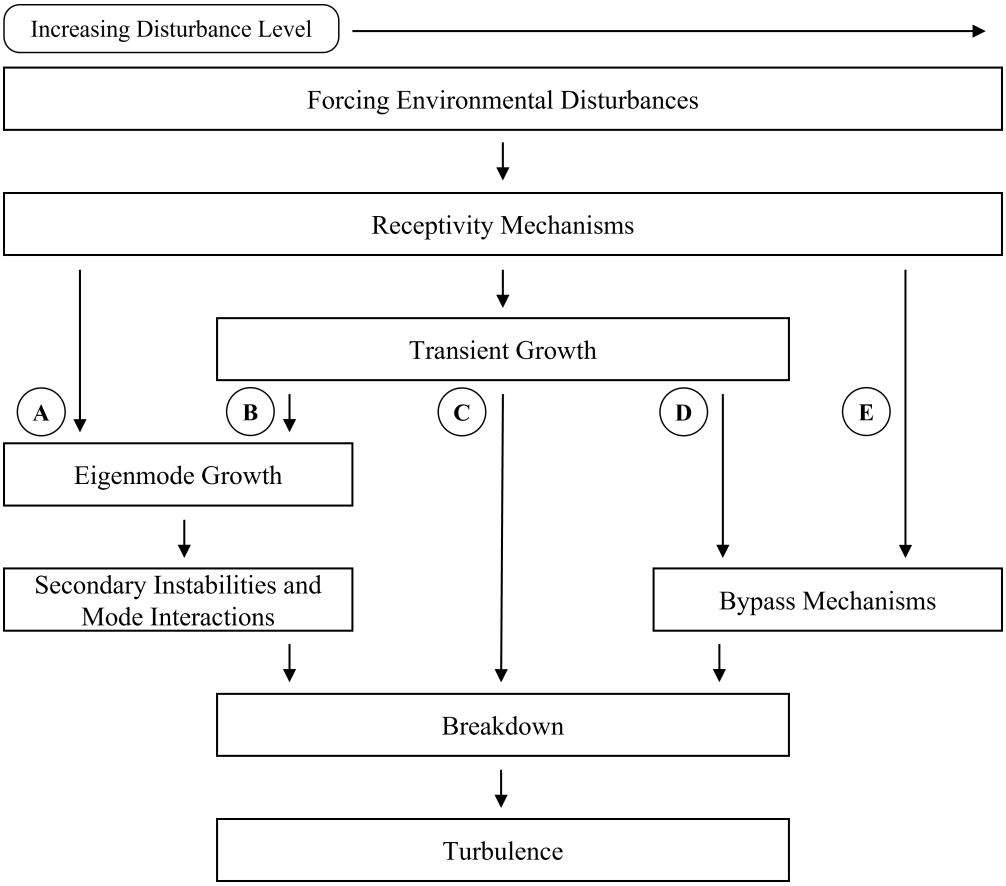

Figure 1.1: Pathways to transition. Adapted from Morkovin et al. [1].

The focus of this work will be on instabilities that appear on a hypersonic cone with a highly-swept fin. The fin adds a feature that will be present on most, if not all, hypersonic vehicles. It also brings its own set of additional flow features not present on the cone alone. These will be elaborated on in Chapters 5 and 6, but the main feature of interest is a vortex pair that appears on the fin and the cone body. The boundary-layer vortex on the cone is seen to transition earlier than the rest of the flow in experiments by Turbeville & Schneider [5]. The instabilities within the cone

vortex will be investigated with spatial BiGlobal (SBG), to ensure that the two dimensions with significant variation are fully considered. Resulting instabilities will be tracked and comparisons will be made to existing experimental and computational results.

There is a large body of work regarding two-dimensional (2-D) and quasi-3-D boundary layers and their instabilities. (Here, a quasi-3-D boundary layer refers to one in which all three velocity profiles are present, but the flow is constant in one dimension.) This covers situations such as a flat plate, an infinite swept wing, or a cone. Most primary instabilities that occur in these flows consist of Tollmein–Schlichting waves, crossflow, Görtler vortices, the first mode, and the second mode. At speeds from roughly Mach 0–0.8 in 2-D boundary layers, 2-D Tollmein–Schlichting waves dominate [6]. These waves become oblique at high subsonic speeds, and the first mode is considered to be its extension into supersonic flow. When a pressure gradient is not aligned with the local inviscid streamline direction, the crossflow instability can lead to transition [7]. The Görtler instability can be induced through concave curvature in the streamwise direction, leading to counter-rotating streamwise vortices [8]. The second mode, or Mack mode instability, is primarily dominant in 2-D boundary layers at speeds beyond Mach 4 [6, 9]. It consists of an acoustic wave trapped in the boundary layer. More details on these instabilities (except for second mode) and their associated transition paths can be found in Reed et al. [10]. The primary instabilities that will be most relevant to this work are crossflow, Görtler, and second mode.

The Görtler and crossflow instabilities both result in streamwise vortices that heavily distort the unperturbed boundary layer. Görtler disturbances are typically steady, while crossflow can exist for zero and nonzero frequencies. Linear Stability Theory (LST) predicts that unsteady crossflow should be more unstable than stationary crossflow [6], however, receptivity seems to play the most important role here. Experiments such as those performed by Deyhle & Bippes [11] and White et al. [12] show that for low freestream-turbulence environments, stationary crossflow is observed to dominate over traveling crossflow. The result of this phenomenon is that boundary layers that support Görtler and stationary-crossflow disturbances both transition to turbulence in a similar manner: nonlinear distortion of the boundary layer through the primary instability occurs,

followed by high-frequency secondary instabilities rapidly leading to breakdown.

These high-frequency secondary instabilities were first identified in the experiments of Poll [13], in which these frequencies were detected after stationary streaks appeared on the geometry, and were noted to be an order of magnitude higher than predictions of traveling crossflow. Predicting these instabilities were outside of the capabilities of the tools of the day, which relied on the flow being at most quasi-3-D. The saturation of crossflow vortices leads to large distortion of the boundary layer, requiring a theory that correctly accounts for two directions with strong spatial variation. The first attempt to solve this problem generally was by Malik et al. [14]. They formed a 2-D eigenvalue problem that used the original boundary layer with crossflow vortices superimposed on top as the basic state. This is still a linear theory, but it was able to display for the first time the kind of modes that were later mapped out by experiments like White & Saric [15], for instance.

As an aside, there were other prior attempts at finding secondary instabilities with linear theory, such as Herbert [16] and Balachandar et al. [17]. They used Floquet theory to add additional 1-D Fourier modes to a finite-amplitude primary instability. With regards to the primary instabilities, one could argue that Pierrehumbert's [18] work was the first use of the 2-D eigenvalue problem. Pierrehumbert sought the instabilities of an inviscid vortex, using a particular wavenumber limit to make the problem tractable. However, Malik et al. [14] is closest to the theory that will be used here, in that the 2-D perturbation equations were solved generally.

This 2-D LST methodology has been used in both temporal and spatial forms, and is reviewed by Theofilis [19, 20]. The theory is sometimes called a "2-D eigenvalue problem" or a "partial-differential-equation-based eigenvalue problem" [21]. However, Theofilis uses the name BiGlobal to describe the theory, and that is the name adopted here. It is important to note that global in this context does not imply an absolute instability, as the theory can be applied to both convective and absolute instabilities. It simply refers to the spatial extent of the mode shape, as opposed to the "local" instabilities of 1-D LST. Theofilis [19] further elaborates on this concept.

In multiple results by Malik et al. [22,23], temporal BiGlobal analysis was applied to crossflow

vortices on an incompressible swept wing. They identified two families of secondary instabilities that have since been observed in a range of vortical flows. The first is dominated by spanwise shear stress, and the second is dominated by wall-normal shear stress. They are known as Type-I and Type-II modes, respectively. Figure 7 in reference [23] shows an excellent example of how these modes typically manifest. For the Type-I mode, the streamwise-velocity perturbation is concentrated on what is sometimes called the shoulder of the vortex, near a saddle point with regards to the in-plane basic-state velocity. On the other hand, the Type-II mode typically has its streamwise-velocity perturbation concentrated near the peak of the vortex.

Recently, SBG has been applied to a series of hypersonic configurations. A yawed cone in Mach-6 flow was studied under quiet conditions at Texas A&M University by Craig & Saric [24]. They were able to record detailed hot-wire measurements that provided both the distorted mean flow and high-frequency perturbations that developed within crossflow vortices on the cone. Similar experiments were also performed by Ward et al. [25] at Purdue University, with a focus on capturing wall-pressure and heat flux measurements. These experiments were analyzed by multiple research groups. Moyes et al. [26] used Nonlinear Parabolized Stability Equations (NPSE) to reproduce the stationary crossflow, and SBG to analyze its secondary instabilities. They found both the same Type-I and Type-II modes as discussed by Malik et al. [22], but also modified primary instabilities inside the vortex. Specifically, traveling-crossflow and second-mode instabilities were found, and were able to be tracked from their origin upstream in the undisturbed boundary layer. Type-I and traveling crossflow are confirmed as the modes detected by Craig & Saric [24]. Much of the experimental and computational analysis from these groups was summed up in Kocian et al. [27]. Li et al. [28] and Choudhari et al. [29] analyzed similar crossflow vortices that were generated through Direct Numerical Simulation (DNS) with SBG and its PSE extension, PSE-3D. This modification of BiGlobal allows nonparallel effects to be correctly modeled, and has been shown to agree very well with full DNS results. They also note that like LST under-predicts growth rates due to nonparallel effects, SBG also under-predicts amplification relative to plane-marching PSE and DNS.

Other applications of SBG (and PSE-3D) to hypersonic flowfields include analysis of the HIFiRE-5b elliptic-cone flight experiment by Choudhari et al. [30]. The theory was used at the semi-minor axis, where spanwise pressure gradients cause a mushroom structure to appear that has different stability characteristics than other boundary-layer vortices. Paredes et al. [31] analyzed the same vehicle, including regions away from the semi-minor axis, and compared LST with SBG in regions of moderate spanwise inhomogeneity. They showed when the boundary-layer distortion is small, LST can predict the correct frequency band for unstable modes, but the growth rate can be significantly different. BOLT, another hypersonic flight experiment, has similar spanwise pressure gradients to HIFiRE-5b, but they originate from concave curvature as opposed to convex [32]. The center region was analyzed by Li et al. [33], finding second mode and shear instabilities in the complicated center-line structure. Chen et al. [34] have analyzed the HyTRV geometry, which features a variety of 3-D boundary layers across its surface. They reported a series of instabilities detected with SBG and N factors at which they predict transition might occur, based off an accompanying DNS.

As the flowfields have become more complex, so has the application of spatial BiGlobal. Methods that worked on a swept wing might not work on BOLT, and methods that work on BOLT will not work on the finned cone mentioned previously. This dissertation expands on the application of SBG in a few ways, focusing on operating under the core assumptions as accurately as possible. In Chapter 2, the theory surrounding modal instabilities will be discussed. LST will be explained in order to build up spatial BiGlobal theory, which is be the main tool used in this dissertation. In Chapter 3, the theory and algorithms that are necessary to compute numerical solutions of the SBG problem are described. Verification of the tools developed is shown in Chapter 4. Chapters 5 and 6 will cover a cone with a single swept fin in hypersonic flow at two different Reynolds numbers. This geometry has been the subject of multiple experimental and computational investigations already, and is an excellent proving ground for the application of SBG to complex flowfields. Stability results will be compared with experiments where possible. Finally, the main findings of this work are summarized in Chapter 7.

2. STABILITY THEORY

2.1 Linear Stability Theory

As mentioned in Chapter 1, instabilities that grow along path A of figure 1.1 can be predicted by Linear Stability Theory. LST is derived by perturbing the governing equations for fluid flow and solving for the perturbation. This derivation and its associated assumptions will now be discussed in detail.

In order to nondimensionalize the equations, the following reference variables are used: ρ_{ref}, u_{ref}, L_{ref}, T_{ref}, μ_{ref}, k_{ref}, $c_{p,ref}$, $c_{v,ref}$, and R_{ref}. Equation 2.1 shows how each dimensional variable, those with a *, are made nondimensional.

$$\rho = \frac{\rho^*}{\rho_{ref}} \tag{2.1a}$$

$$u = \frac{u^*}{u_{ref}} \tag{2.1b}$$

$$T = \frac{T^*}{T_{ref}} \tag{2.1c}$$

$$p = \frac{p^*}{\rho_{ref} u_{ref}^2} \tag{2.1d}$$

$$t = \frac{t^* L_{ref}}{u_{ref}} \tag{2.1e}$$

$$\mu = \frac{\mu^*}{\mu_{ref}} \tag{2.1f}$$

$$\lambda = \frac{\lambda^*}{\lambda_{ref}} \tag{2.1g}$$

$$k = \frac{k^*}{k_{ref}} \tag{2.1h}$$

$$c_p = \frac{c_p^*}{c_{p,ref}} \tag{2.1i}$$

$$c_v = \frac{c_v^*}{c_{v,ref}} \tag{2.1j}$$

$$R = \frac{R^*}{R_{ref}} \tag{2.1k}$$

The equations for the conservation of mass, momentum, and energy, along with the thermodynamic relations are shown in nondimensional form in equations 2.2.

$$\frac{\partial \rho}{\partial t} + \nabla \cdot \rho \boldsymbol{v} = 0 \tag{2.2a}$$

$$\rho \left(\frac{\partial \boldsymbol{v}}{\partial t} + (\boldsymbol{v} \cdot \nabla)\boldsymbol{v} \right) = -\nabla p + \frac{1}{Re} \nabla \cdot \left[\mu \left(\nabla \boldsymbol{v} + (\nabla \boldsymbol{v})^T \right) + \lambda (\nabla \cdot \boldsymbol{v}) \boldsymbol{\mathcal{I}} \right] \tag{2.2b}$$

$$\begin{gathered} \rho \left(\frac{\partial T}{\partial t} + (\boldsymbol{v} \cdot \nabla) T \right) = -\gamma Ec \, p (\nabla \cdot \boldsymbol{v}) + \frac{\gamma}{RePr} \nabla \cdot (k \nabla T) + \frac{\gamma Ec}{Re} \Phi, \\ \Phi = \mu \left[\nabla \boldsymbol{v} : \nabla \boldsymbol{v} + \nabla \boldsymbol{v} : (\nabla \boldsymbol{v})^T \right] + \lambda (\nabla \cdot \boldsymbol{v})^2 \end{gathered} \tag{2.2c}$$

$$p = \frac{1}{\gamma M^2} \rho T \tag{2.2d}$$

$$\mu = \frac{\mu_S}{\mu_{ref}} \left(\frac{T T_{ref}}{T_S} \right)^{3/2} \frac{T_S + S}{T T_{ref} + S} \tag{2.2e}$$

$$\lambda = \frac{-2}{3}\mu \tag{2.2f}$$

$$k = \mu \tag{2.2g}$$

In equation 2.2c, the double inner product is defined as $\boldsymbol{\mathcal{A}} : \boldsymbol{\mathcal{A}} = \sum_i \sum_j A_{ij} A_{ij}$. The nondimensional numbers used in equations 2.2 are defined as follows:

$$M = \frac{u_{ref}}{\sqrt{\gamma R T_{ref}}} \tag{2.3a}$$

$$Re = \frac{\rho_{ref} u_{ref} L_{ref}}{\mu_{ref}} \tag{2.3b}$$

$$Pr = \frac{c_{p,ref} \mu_{ref}}{k_{ref}} \tag{2.3c}$$

$$Ec = \frac{u_{ref}^2}{c_{p,ref} T_{ref}} \tag{2.3d}$$

$$\gamma = \frac{c_{p,ref}}{c_{v,ref}} \tag{2.3e}$$

Equations 2.2a–2.2c are the mass, momentum, and energy equations in vector form, collectively referred to here as the Navier–Stokes equations. All flows are assumed to follow the ideal gas law (equation 2.2d), which is valid as long as extremely low densities or high pressures are not present. Sutherland's Law is used for viscosity, which is accurate up to 2% from 170 K to 1900 K [35]. The particular constants used in this equation are $\mu_S = 1.716 \times 10^{-5}$ Ns/m^2, $T_S = 273$ K, and $S = 111$ K. Stokes hypothesis is used for bulk viscosity. The gas is assumed to be calorically perfect, and thermal diffusivity is then determined from a constant Prandtl number, typically $Pr = 0.72$.

The equations can then be perturbed in each variable, neglecting any quadratic or higher-order perturbations. This assumption is based on the idea that any perturbation remains small (infinitesimal) relative to the base flow ($T' \ll \bar{T}$). This leads to:

$$\frac{\partial \rho'}{\partial t} + \nabla \cdot \rho' \bar{\boldsymbol{v}} + \nabla \cdot \bar{\rho} \boldsymbol{v}' = 0 \tag{2.4a}$$

$$\begin{aligned}
&\rho' \left(\frac{\partial \bar{\boldsymbol{v}}}{\partial t} + (\bar{\boldsymbol{v}} \cdot \nabla) \bar{\boldsymbol{v}} \right) + \bar{\rho} \left(\frac{\partial \boldsymbol{v}'}{\partial t} + (\boldsymbol{v}' \cdot \nabla) \, \bar{\boldsymbol{v}} + (\bar{\boldsymbol{v}} \cdot \nabla) \boldsymbol{v}' \right) = \\
&- \nabla p' + \frac{1}{Re} \nabla \cdot \left[\mu' \left(\nabla \bar{\boldsymbol{v}} + (\nabla \bar{\boldsymbol{v}})^T \right) + \bar{\mu} \left(\nabla \boldsymbol{v}' + (\nabla \boldsymbol{v}')^T \right) + \left(\lambda' (\nabla \cdot \bar{\boldsymbol{v}}) + \bar{\lambda} \, (\nabla \cdot \boldsymbol{v}') \right) \boldsymbol{\mathcal{I}} \right]
\end{aligned} \tag{2.4b}$$

$$\begin{aligned}
&\rho' \left(\frac{\partial \bar{T}}{\partial t} + (\bar{\boldsymbol{v}} \cdot \nabla) \bar{T} \right) + \bar{\rho} \left(\frac{\partial T'}{\partial t} + (\boldsymbol{v}' \cdot \nabla) \, \bar{T} + (\bar{\boldsymbol{v}} \cdot \nabla) T' \right) = \\
&- \gamma Ec \, (p' (\nabla \cdot \bar{\boldsymbol{v}}) + \bar{p} \, (\nabla \cdot \boldsymbol{v}')) + \frac{\gamma}{RePr} \nabla \cdot \left(k' \nabla \bar{T} + \bar{k} \nabla T' \right) + \frac{\gamma Ec}{Re} \Phi', \\
&\Phi' = \mu' \left[\nabla \bar{\boldsymbol{v}} : \nabla \bar{\boldsymbol{v}} + \nabla \bar{\boldsymbol{v}} : (\nabla \bar{\boldsymbol{v}})^T \right] + \bar{\mu} \left[2 \nabla \boldsymbol{v}' : \nabla \bar{\boldsymbol{v}} + 2 \nabla \boldsymbol{v}' : (\nabla \bar{\boldsymbol{v}})^T \right] + \lambda' (\nabla \cdot \bar{\boldsymbol{v}})^2 \\
&+ 2 \bar{\lambda} \, (\nabla \cdot \boldsymbol{v}') \, (\nabla \cdot \bar{\boldsymbol{v}})
\end{aligned} \tag{2.4c}$$

$$p' = \frac{1}{\gamma M^2} \left(\rho' \bar{T} + \bar{\rho} T' \right) \tag{2.4d}$$

$$\mu' = \frac{d \bar{\mu}}{d \bar{T}} T' \tag{2.4e}$$

$$\lambda' = \frac{-2}{3} \mu' \tag{2.4f}$$

$$k' = \mu' \tag{2.4g}$$

With the viscosity perturbation, a linear Taylor-series expansion is used instead of perturbing Sutherland's formula. The algebraic relations 2.4d–2.4g are used to eliminate their respective variables from the perturbed Navier–Stokes equations to simplify the problem.

Next, a reference frame must be chosen to take advantage of some simplifying physics. Let (ξ, η, ζ) be a body-fitted orthonormal coordinate system on some aerodynamic vehicle. For instance, if a flat plate at zero angle of attack and zero sweep was considered, ξ would point in the same direction as the freestream, η would be normal to the wall, and ζ would complete the right-handed system. $(\hat{\boldsymbol{\imath}}, \hat{\boldsymbol{\jmath}}, \hat{\boldsymbol{k}})$ will be the unit vectors along the three directions. Various assumptions about the underlying laminar flow and perturbation will be employed with reference to these directions in this chapter. (In Chapter 3, the coordinate systems and reference frames will be redefined. However, it is easier to delay the more complex frames until then and work with the system defined above.)

With LST, the total flow is assumed to consist of a laminar basic-state ($\bar{\phi}$) and a perturbation (ϕ') as in equation 2.5. (For this discussion, ϕ can be considered any of the primitive flow variables.) $\bar{\phi}$ is assumed to be steady and only vary in the η direction, while ϕ' has full spatial and temporal dependence. However, ϕ' must take the form shown in equation 2.6.

$$\phi(\xi, \eta, \zeta, t) = \bar{\phi}(\eta) + \phi'(\xi, \eta, \zeta, t) \tag{2.5}$$

$$\phi'(\xi, \eta, \zeta, t) = A_0 \hat{\phi}(\eta) e^{i(\alpha\xi + \beta\zeta - \omega t)} + c.c. \tag{2.6}$$

While ϕ' must be real since ϕ is real, $\hat{\phi}$, α, β, and ω may all be complex. ($c.c.$ is the complex conjugate.) In essence, this means that ϕ' is a wave in ξ, ζ, and t, with a particular shape in η. A_0 is a (potentially complex) constant initial amplitude. Applying $\partial\bar{\phi}/\partial\xi = \partial\bar{\phi}/\partial\zeta = 0$ and equation 2.6 to equations 2.4 leads to the classic LST equations. Then, for a particular base flow, $\hat{\phi}$ is computed as an eigenvector of the system, and the wave component gives information about the perturbation's growth or decay.

At this point, LST has historically split into two categories: temporal and spatial analysis. For temporal stability, ω is a complex eigenvalue solved as a function of real α and β. This is akin to a wave that is constant in space but growing in time. On the other hand, spatial stability restricts ω to real frequencies, while the wavenumbers α and β are complex. Transformations have been derived to convert between temporal and spatial stability for convective instabilities [36,37], which are the kind that are considered in this work. However, spatial stability is considered to be the more physical interpretation of the physics at play, so that is the method chosen here.

Spatial LST is formulated as $\alpha = \alpha(\omega, \beta)$. This leaves 5 unknowns (α_r, α_i, β_r, β_i, and ω), with two relations provided by LST. Frequency and spanwise wavenumber should be provided as part of the problem specification, which leaves an uncertainty in how to handle β_i. In Nayfeh [38], it is shown that a solvability condition can be used to complete the system. Namely, $d\alpha/d\beta$ must be real. (As a result, the group velocity is also real.) The perturbation problem can then be solved by specifying ω, β_r, and β_i, calculating $d\alpha/d\beta$, then iterating on β_i until the solvability condition is met.

This mathematical form for the perturbation imbues certain properties. First, there is a wave vector, defined as $\boldsymbol{k} = \alpha_r \hat{\boldsymbol{\imath}} + \beta_r \hat{\boldsymbol{k}}$. This is the direction that the wavefront is oriented. Since α and β are complex, there is also a growth direction defined as $\boldsymbol{\sigma} = -\alpha_i \hat{\boldsymbol{\imath}} - \beta_i \hat{\boldsymbol{k}}$. Finally, the associated group velocity is shown in equation 2.7. The group velocity is the direction that energy travels when the wave is considered as one part of a sum of various frequencies and wavenumbers. All of these vectors can be oriented in different directions, and the physics will dictate what the directions are for a specific problem. Figure 2.1 shows an example of how the different vectors may be oriented.

$$\boldsymbol{v}_g = \frac{\partial \omega}{\partial \alpha} \hat{\boldsymbol{\imath}} + \frac{\partial \omega}{\partial \beta} \hat{\boldsymbol{k}} \tag{2.7}$$

Once the growth rates are known, they can be used to find the spatial growth of that perturbation. Since the perturbation is formally infinitesimal, the amplification of a mode can only be calculated relative to itself, as opposed to some base-flow quantity. When calculating the amplifi-

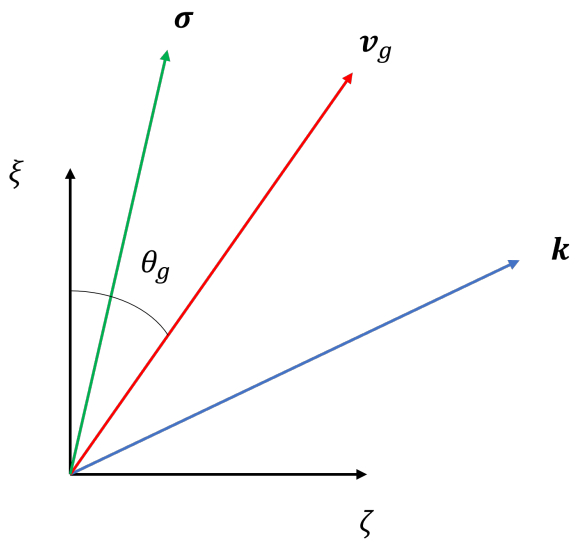

Figure 2.1: Definition of vectors associated with an instability. $\boldsymbol{k}$ is the wave vector, $\boldsymbol{v}_g$ is the group-velocity vector, and $\boldsymbol{\sigma}$ is the growth vector.

cation of an instability, the result is typically reported as an N factor, which will now be derived.

The LST perturbation can be written in an alternative way that removes complex numbers:

$$\phi' = 2|A_0|e^{-\alpha_i\xi-\beta_i\zeta}|\hat{\phi}|\sin(\alpha_r\xi+\beta_r\zeta-\omega t+\theta) \tag{2.8a}$$

$$\theta = \tan^{-1}\left(\frac{A_{0i}\hat{\phi}_i - A_{0r}\hat{\phi}_r}{A_{0r}\hat{\phi}_i + A_{0i}\hat{\phi}_r}\right) \tag{2.8b}$$

The amplitude of the wave can be identified as the part that premultiplies the sine function in 2.8a. Equation 2.9 shows that the amplitude is a function of all three coordinates, with contributions from α_i, β_i, and $\hat{\phi}$.

$$A(\xi,\eta,\zeta) = 2|A_0|e^{-\alpha_i\xi-\beta_i\zeta}|\hat{\phi}| \tag{2.9}$$

According to Nayfeh [38], the amplitude of a wave should be tracked along its group-velocity direction, $\boldsymbol{v}_g$. This leads to a line integral that must be evaluated along a curve tangent to $\boldsymbol{v}_g$. For a curve $\boldsymbol{c}$ parameterized by s, a generic line integral is defined by equation 2.10. Substituting in

the growth of the perturbation along s for f leads to equation 2.11 as the general formula for the N factor.

$$\int_{\boldsymbol{c}} f(x,y)ds = \int_{s_0}^{s_1} f(\boldsymbol{c}(s))|\boldsymbol{c}'(s)|ds \tag{2.10}$$

$$N = \int_{\boldsymbol{c}} \frac{1}{A(\xi,\eta,\zeta)} \frac{\partial A(\xi,\eta,\zeta)}{\partial s} ds = \int_{s_0}^{s_1} \frac{1}{A(\boldsymbol{c}(s))} \frac{\partial A(\boldsymbol{c}(s))}{\partial s} |\boldsymbol{c}'(s)| ds \tag{2.11}$$

This curve is actually a ray for parallel flow, and can be parameterized as follows:

$$\xi = s\cos\theta_g \tag{2.12a}$$

$$\eta = \eta_0 \tag{2.12b}$$

$$\zeta = s\sin\theta_g \tag{2.12c}$$

$$\boldsymbol{c}(s) = s\cos\theta_g \hat{\boldsymbol{\imath}} + \eta_0 \hat{\boldsymbol{\jmath}} + s\sin\theta_g \hat{\boldsymbol{k}} \tag{2.12d}$$

Note that η does not change along the curve, as the definition of group velocity in equation 2.7 is for a plane wave propagating normal to $\hat{\boldsymbol{\jmath}}$. In order to specialize equation 2.11 to LST, $A(\boldsymbol{c}(s))$ and $|\boldsymbol{c}'(s)|$ must be defined.

$$A(\boldsymbol{c}(s)) = 2|A_0| e^{(-\alpha_i \cos\theta_g - \beta_i \sin\theta_g)s} |\hat{\phi}(\eta_0)| \tag{2.13}$$

$$|\boldsymbol{c}'(s)| = \sqrt{\cos^2\theta_g + \sin^2\theta_g} = 1 \tag{2.14}$$

Finally, substituting equations 2.13 and 2.14 into equation 2.11, leads to:

$$
\begin{aligned}
N &= \int_{s_0}^{s_1} \frac{(-\alpha_i \cos\theta_g - \beta_i \sin\theta_g) 2|A_0| e^{(-\alpha_i \cos\theta_g - \beta_i \sin\theta_g)s} |\hat{\phi}(\eta_0)|}{2|A_0| e^{(-\alpha_i \cos\theta_g - \beta_i \sin\theta_g)s} |\hat{\phi}(\eta_0)|} ds \\
&= \int_{s_0}^{s_1} (-\alpha_i \cos\theta_g - \beta_i \sin\theta_g) ds \\
&= (-\alpha_i \cos\theta_g - \beta_i \sin\theta_g)(s_1 - s_0)
\end{aligned}
\tag{2.15}
$$

This derivation is general and assumes nothing about the coordinate system's orientation relative to the flow, or any symmetries or special alignment of the wave components.

LST has a long history of use in boundary-layer transition prediction, using both the temporal and spatial forms of the theory. Extensive parametric studies of its predictions for Falkner-Skan-Cooke boundary layers can be found by Mack [6, 39], and reviews of the theory can be found in Arnal [40] and Reed et al. [41].

2.2 Spatial BiGlobal

Spatial BiGlobal is a natural extension of spatial LST. It still considers parallel flows ($\partial\bar{\phi}/\partial\xi = 0$), but allows for spanwise variation of the basic state. In the same vein, instead of the perturbation being represented in ζ by a single wavenumber, β, it is allowed to remain general in ζ. These two sets of assumptions are defined by equations 2.16 and 2.17.

$$
\phi(\xi, \eta, \zeta, t) = \bar{\phi}(\eta, \zeta) + \phi'(\xi, \eta, \zeta, t) \tag{2.16}
$$

$$
\phi'(\xi, \eta, \zeta, t) = A_0 \hat{\phi}(\eta, \zeta) e^{i(\alpha\xi - \omega t)} + c.c. \tag{2.17}
$$

This changes the system of equations from a set of Ordinary Differential Equations (ODEs) to a set of Partial Differential Equations (PDEs), which require extra boundary conditions to be enforced. When equation 2.17 is substituted into the perturbed Navier–Stokes equations, it can be reduced to the following form:

$$\boldsymbol{\mathcal{A}}\frac{\partial^2\hat{\boldsymbol{\phi}}}{\partial\eta^2}+\boldsymbol{\mathcal{B}}\frac{\partial^2\hat{\boldsymbol{\phi}}}{\partial\eta\partial\zeta}+\boldsymbol{\mathcal{C}}\frac{\partial^2\hat{\boldsymbol{\phi}}}{\partial\zeta^2}+(\boldsymbol{\mathcal{D}_0}+\alpha\boldsymbol{\mathcal{D}_1})\frac{\partial\hat{\boldsymbol{\phi}}}{\partial\eta}+(\boldsymbol{\mathcal{E}_0}+\alpha\boldsymbol{\mathcal{E}_1})\frac{\partial\hat{\boldsymbol{\phi}}}{\partial\zeta}+(\boldsymbol{\mathcal{F}_0}+\alpha\boldsymbol{\mathcal{F}_1}+\alpha^2\boldsymbol{\mathcal{F}_2})\hat{\boldsymbol{\phi}}=\mathbf{0} \quad (2.18)$$

with $\hat{\boldsymbol{\phi}}^T = [\hat{u},\hat{v},\hat{w},\hat{T},\hat{\rho}]$ and matrices $\boldsymbol{\mathcal{A}}$–$\boldsymbol{\mathcal{F}} \in \mathbb{C}^{5\times5}$. With the application of homogeneous boundary conditions, this is a quadratic eigenvalue problem in α, with $\hat{\boldsymbol{\phi}}$ as its associated eigenvector. The companion-matrix approach [42] can then be used to reformulate equation 2.18 into a generalized eigenvalue problem in α, shown in equations 2.19. $\boldsymbol{\mathcal{F}_{2R}}$ is the same as $\boldsymbol{\mathcal{F}_2}$, except that the last column of 0s has been removed, making $\boldsymbol{\mathcal{F}_{2R}} \in \mathbb{C}^{5\times4}$.

$$\boldsymbol{\mathcal{M}_1} = \left[\begin{array}{c|c} \boldsymbol{\mathcal{A}}\frac{\partial^2}{\partial\eta^2}+\boldsymbol{\mathcal{B}}\frac{\partial^2}{\partial\eta\partial\zeta}+\boldsymbol{\mathcal{C}}\frac{\partial^2}{\partial\zeta^2}+\boldsymbol{\mathcal{D}_0}\frac{\partial}{\partial\eta}+\boldsymbol{\mathcal{E}_0}\frac{\partial}{\partial\zeta}+\boldsymbol{\mathcal{F}_0} & \boldsymbol{\mathcal{I}}^{5\times4} \\ \hline \boldsymbol{0}^{4\times5} & \boldsymbol{\mathcal{I}}^{4\times4} \end{array}\right] \quad (2.19a)$$

$$\boldsymbol{\mathcal{M}_2} = -\left[\begin{array}{c|c} \boldsymbol{\mathcal{D}_1}\frac{\partial}{\partial\eta}+\boldsymbol{\mathcal{E}_1}\frac{\partial}{\partial\zeta}+\boldsymbol{\mathcal{F}_1} & \boldsymbol{\mathcal{F}_{2R}} \\ \hline \boldsymbol{\mathcal{I}}^{4\times4} & \boldsymbol{0}^{4\times5} \end{array}\right] \quad (2.19b)$$

$$\hat{\boldsymbol{\Phi}}^T = \left[\begin{array}{ccccc|cccc} \hat{u} & \hat{v} & \hat{w} & \hat{T} & \hat{\rho} & \alpha\hat{u} & \alpha\hat{v} & \alpha\hat{w} & \alpha\hat{T} \end{array}\right] \quad (2.19c)$$

$$\boldsymbol{\mathcal{M}_1}\hat{\boldsymbol{\Phi}} = \alpha\boldsymbol{\mathcal{M}_2}\hat{\boldsymbol{\Phi}} \quad (2.19d)$$

SBG is required when spanwise variation is essential to the problem, such as corner flows, horseshoe vortices, crossflow vortices, or other three-dimensional features. It is worth noting that SBG, like LST, still assumes $\partial\bar{\phi}/\partial\xi = 0$ and in general will under-predict growth rates as a result. However, this theory still expands the breadth of applicable flowfields compared to LST. Reviews of this theory and its usage are available by Theofilis in references [19] and [20].

As previously mentioned, one of the main assumptions in spatial BiGlobal is that $\partial\bar{\phi}/\partial\xi = 0$. This is almost never true in any real flowfield. Therefore, in order to keep model error to a minimum, one should attempt to minimize this derivative when choosing the ξ direction. This is

akin to finding a direction such that $\partial^2\bar{\phi}/\partial\xi^2 = 0$. However, this is not an easy condition to satisfy. For instance, it is unclear what basic-state quantity should be used for $\bar{\phi}$. In a three-dimensional boundary layer, there is no guarantee that different choices will produce the same direction for ξ. In addition, since SBG is solved on a surface, the best direction may change across that surface. As a result, assumptions about the direction based on the underlying physics are often needed to choose the best direction for ξ.

2.2.1 Parallel N Factor

When calculating an N factor for spatial BiGlobal, there is an extra consideration with the eigenfunction $\hat{\phi}$. In this type of solution, the growth in ζ is contained in $\hat{\phi}$, so this term cannot be neglected when forming the amplitude. For SBG, the perturbation can be rewritten as equation 2.20.

$$\phi' = 2|A_0|e^{-\alpha_i\xi}|\hat{\phi}|\sin(\alpha_r\xi - \omega t + \theta) \tag{2.20a}$$

$$\theta = \tan^{-1}\left(\frac{A_{0i}\hat{\phi}_i - A_{0r}\hat{\phi}_r}{A_{0r}\hat{\phi}_i + A_{0i}\hat{\phi}_r}\right) \tag{2.20b}$$

The definition of the group-velocity curve in equations 2.12 are still valid, but importantly, θ_g is now a function of ζ. This leads to a change in the partial derivatives of ξ and ζ with respect to s.

$$\frac{\partial\zeta}{\partial s} = \frac{\sin\theta_g}{1 - s\cos\theta_g\frac{d\theta_g}{d\zeta}} \tag{2.21a}$$

$$\begin{aligned}\frac{\partial\xi}{\partial s} &= \cos\theta_g - s\sin\theta_g\frac{d\theta_g}{d\zeta}\frac{\partial\zeta}{\partial s} \\ &= \cos\theta_g - \frac{s\sin^2\theta_g\frac{d\theta_g}{d\zeta}}{1 - s\cos\theta_g\frac{d\theta_g}{d\zeta}} \\ &= \frac{\cos\theta_g - s\frac{d\theta_g}{d\zeta}}{1 - s\cos\theta_g\frac{d\theta_g}{d\zeta}}\end{aligned} \tag{2.21b}$$

After some algebra, the magnitude of the curve's tangent vector can be written as:

$$|\boldsymbol{c}'(s)| = \sqrt{1 + \left(\frac{s \sin\theta_g \frac{d\theta_g}{d\zeta}}{1 - s\cos\theta_g \frac{d\theta_g}{d\zeta}} \right)^2} \tag{2.22}$$

Note that if $d\theta_g/d\zeta = 0$, then equation 2.22 reduces to unity, as in equation 2.14.

Combining all of this leads to the SBG N factor to be defined as

$$\begin{aligned} N &= \int_{s_0}^{s_1} \frac{1}{2|A_0|e^{-\alpha_i \xi}|\hat{\phi}|} 2|A_0| \left(\frac{\partial \xi}{\partial s}(-\alpha_i)e^{-\alpha_i \xi}|\hat{\phi}| + e^{-\alpha_i \xi}\frac{\partial \zeta}{\partial s}\frac{\partial |\hat{\phi}|}{\partial \zeta} \right) |\boldsymbol{c}'(s)| ds \\ &= \int_{s_0}^{s_1} \left(-\alpha_i \frac{\partial \xi}{\partial s} + \frac{1}{|\hat{\phi}|}\frac{\partial |\hat{\phi}|}{\partial \zeta}\frac{\partial \zeta}{\partial s} \right) |\boldsymbol{c}'(s)| ds \\ &= \int_{s_0}^{s_1} \left(-\alpha_i \frac{\cos\theta_g - s\frac{d\theta_g}{d\zeta}}{1 - s\cos\theta_g \frac{d\theta_g}{d\zeta}} + \frac{1}{|\hat{\phi}|}\frac{\partial |\hat{\phi}|}{\partial \zeta}\frac{\sin\theta_g}{1 - s\cos\theta_g \frac{d\theta_g}{d\zeta}} \right) \sqrt{1 + \left(\frac{s \sin\theta_g \frac{d\theta_g}{d\zeta}}{1 - s\cos\theta_g \frac{d\theta_g}{d\zeta}} \right)^2} ds \end{aligned} \tag{2.23}$$

Some simplified versions of this equation are worth noting. If the group-velocity direction is constant with respect to ζ, then $d\theta_g/d\zeta = 0$ and equation 2.23 reduces to

$$\begin{aligned} N &= \int_{s_0}^{s_1} \left(-\alpha_i \cos\theta_g + \frac{1}{|\hat{\phi}|}\frac{\partial |\hat{\phi}|}{\partial \zeta}\sin\theta_g \right) ds \\ &= -\alpha_i \cos\theta_g \left(s_1 - s_0 \right) + \int_{s_0}^{s_1} \frac{1}{|\hat{\phi}|}\frac{\partial |\hat{\phi}|}{\partial \zeta}\sin\theta_g ds \end{aligned} \tag{2.24}$$

If the group-velocity direction is constant in ζ and is in the direction of ξ, then the N factor reduces to

$$N = -\alpha_i \left(s_1 - s_0 \right) \tag{2.25}$$

Equation 2.25 is the most commonly used definition of the SBG N factor. If the distribution of the group-velocity direction can be determined based on physical reasoning or from a previous

stability result, then equations 2.23 or 2.24 can be used as appropriate. In the rest of this work, equation 2.25 will be used, but future work on extracting the group-velocity direction from spatial BiGlobal solutions could lead to more-accurate predictions of integrated growth.

2.2.2 Nonparallel N Factor

For nonparallel boundary layers, the prediction by SBG at one point does not hold for all space like it does for parallel flows. As a result, SBG is typically done at a series of planes along the ξ direction, and multiple, independent solutions are stitched together. When equation 2.25 is used for each section, the effect is to numerically integrate $-\alpha_i$ as if it *did* vary with ξ.

3. METHODOLOGY*

In order to apply the SBG theory to the finned cone and other complex geometries, an SBG solver was developed from scratch, named Boundary Layer Analysis using Surface Techniques (BLAST). This section will detail some of the theory and numerics the code employs.

Equations 2.4 are the vector form of the linearized Navier–Stokes equations, without the SBG assumptions applied. In order to reduce these equations to their spatial BiGlobal form, a coordinate system must be specified. BLAST can be divided into two sections based on the type of coordinate system that is used to solve the equations: orthogonal and nonorthogonal. For clarity, the following notation will be used. (X, Y, Z) will refer to an inertial Cartesian coordinate system, with basis vectors $C : \left\{\hat{\boldsymbol{\imath}}, \hat{\boldsymbol{\jmath}}, \hat{\boldsymbol{k}}\right\}$. (x, y, z) will denote an orthogonal curvilinear coordinate system, with basis vectors $O : \{\boldsymbol{e}_x, \boldsymbol{e}_y, \boldsymbol{e}_z\}$. (a, b, c) refers to a computational coordinate system with equal spacing, denoted as the T frame. Next, (ξ, η, ζ) refers to a general (potentially nonorthogonal) curvilinear coordinate system, with its frame given by $N : \{\boldsymbol{a}_\xi, \boldsymbol{a}_\eta, \boldsymbol{a}_\zeta\}$. A final coordinate system that will not appear in this chapter but is needed in Chapters 5 and 6 is a cylindrical system. This will be denoted by coordinates (χ, r, Θ) and frame R, spanned by basis vectors $\{\boldsymbol{b}_\chi, \boldsymbol{b}_r, \boldsymbol{b}_\Theta\}$.

3.1 Orthogonal Code

The orthogonal section of the code was developed first, in line with EPIC [43–45], another stability code used by the Computational Stability and Transition Lab. The coordinate system is generated by defining a curve on the surface of the relevant geometry. Then, wall-normal lines are extruded from the wall to some height. By using strictly wall-normal lines, an orthogonal coordinate system can be ensured.

To define frame O, $\boldsymbol{e}_y$ points away from the wall, and $\boldsymbol{e}_x$ is oriented such that it is normal to the stability surface with the maximum value of $\boldsymbol{v}_\infty \cdot \boldsymbol{e}_x$. $\boldsymbol{e}_z$ is oriented tangent to the wall and tangent

*Portions of this chapter are reprinted with permission from "Linear Stability of a Boundary-Layer Vortex on a Hypersonic Finned Cone" by Andrew Riha, Madeline McMillan, and Helen L. Reed, 2021. *AIAA Aviation 2021 Forum, AIAA Paper 2021-2890*, Copyright 2021 by Andrew Riha, Madeline McMillan, and Helen L. Reed.

to the stability surface, such that the right-hand rule is in effect. (In other words, $\boldsymbol{e}_x \times \boldsymbol{e}_y = c\boldsymbol{e}_z$, where c is a positive constant.)

An important feature of the basis vectors $\{\boldsymbol{e}_x, \boldsymbol{e}_y, \boldsymbol{e}_z\}$ is that they are, in general, not of unit length. This means that for some vector, if $\boldsymbol{v} = u_C\hat{\boldsymbol{\imath}} + v_C\hat{\boldsymbol{\jmath}} + w_C\hat{\boldsymbol{k}} = u_O\boldsymbol{e}_x + v_O\boldsymbol{e}_y + w_O\boldsymbol{e}_z$, vector components u_C and u_O cannot be directly compared. When $\boldsymbol{v}$ represents a physical quantity, such as velocity, u_O is not even guaranteed to have the same units as $|\boldsymbol{v}|$. To aid with showing the differences between the orthogonal and nonorthogonal coordinate systems, some transformation laws will be defined. A more complete treatment can be found in Aris [46].

3.1.1 Tensor Calculus

Summation notation will be used, where a sum is implied over the same index when it is repeated diagonally. For instance, ${u_C}^j\hat{\boldsymbol{\imath}}_j$ is understood to mean $\sum_{j=1}^{3} {u_C}^j\hat{\boldsymbol{\imath}}_j$. (The subscripts C, O, and N are referring to the frames mentioned above and should *not* be considered indices used in summation notation.) The number of indices that are not repeated is the order of the tensor under consideration. The location of the index has meaning: a raised index indicates contravariance and a lowered one means covariance. Contravariance and covariance refers to how the components of a vector transform. For example, a velocity vector's components (contravariant) will transform according to 3.1, while those of a gradient of temperature (covariant) follow the inverse transformation law in equation 3.2.

$$ {u_O}^i = \frac{\partial x^i}{\partial X^j} {u_C}^j \tag{3.1} $$

$$ \frac{\partial T}{\partial x^i} = \frac{\partial X^j}{\partial x^i} \frac{\partial T}{\partial X^j} \tag{3.2} $$

In Euclidean space, there is always a second-order metric tensor $\boldsymbol{g}$ that contains information about the transformation from a Cartesian coordinate system to an arbitrary coordinate system. Its covariant components for the transformation from the C coordinates to the O coordinates are defined by:

$$g_{ij} = \sum_{k=1}^{3} \frac{\partial X^k}{\partial x^i} \frac{\partial X^k}{\partial x^j} \tag{3.3}$$

An equivalent definition showing the metric tensor's relation to length is:

$$ds^2 = g_{ij} dx^i dx^j \tag{3.4}$$

If the components g_{ij} are organized in a matrix as shown in equation 3.5,

$$[g_{ij}] = \begin{bmatrix} g_{11} & \cdots & g_{13} \\ \vdots & \ddots & \vdots \\ g_{31} & \cdots & g_{33} \end{bmatrix} \tag{3.5}$$

then some characteristics can be noted in linear algebra terms. For a Cartesian coordinate system, $[g_{ij}]$ is simply the identity matrix. This intuitively makes sense because g_{ij} would then represent a transformation from one Cartesian frame to another, which must preserve length and angles. $[\partial X^i / \partial Y^j]$, where Y^i are the coordinates of the second Cartesian frame, must be an orthogonal rotation matrix, which by definition leads to $g_{ij} = \delta_{ij}$. (δ_{ij} is the covariant Kronecker-Delta.)

For an orthogonal coordinate system like O, angles must be preserved, but not necessarily lengths. This leads to $[g_{ij}]$ having 0s on its off-diagonals, and non-unity values on the diagonal. Another general property of the metric tensor is shown in equation 3.6, and explains these conditions on orthogonal systems as well. For an orthogonal coordinate system, $\boldsymbol{e}_i \cdot \boldsymbol{e}_j = 0$ when $i \neq j$. Since g_{ij} is reduced to three non-zero values, it is often rewritten in terms of scale factors h_i, where $g_{ii} = h_i h_i$ with no sum on i. (This is usually written as $g_{ii} = h_i^2$, but this is an even worse abuse of notation within an already confusing system and will be avoided.)

$$g_{ij} = \boldsymbol{e}_i \cdot \boldsymbol{e}_j \tag{3.6}$$

Another important use for the matrix tensor is to raise and lower indices. For instance, the components of a velocity vector can be written in their covariant form by using $u_{Oi} = g_{ij} u_O{}^j$. The

reverse is true: ${u_O}^i = g^{ij} u_{Oj}$. And since $g_{ij} g^{jk} = \delta_i^k$, the components of g^{ij} can easily be found through $[g^{ij}] = [g_{ij}]^{-1}$.

Spatial derivatives take on a different form in non-Cartesian systems. For instance, one of the terms in the perturbed continuity equation (2.4a), must be written as follows when specialized to the O coordinate system. Note that the spatial derivatives of h_i, of the coordinate system itself, are also a factor in the gradient.

$$\nabla \cdot \rho \boldsymbol{v}' = \frac{1}{h_1 h_2 h_3} \frac{\partial}{\partial x^i} (h_1 h_2 h_3 \rho {u'_O}^i) \tag{3.7}$$

Besides allowing for scaling arguments about the directions of strong and weak variation in a boundary layer to be used, another important benefit from using the wall-normal lines for the orthogonal coordinate system comes from the calculation of h_i. Let the wall be defined by $S(x, z)$, where $y = 0$. Everywhere on S in space, let $h_i = 1_i$. This also requires that $|\boldsymbol{e}_x| = |\boldsymbol{e}_y| = |\boldsymbol{e}_z| = 1$ on S. Then, $\boldsymbol{e}_y$ is defined by $\boldsymbol{e}_y(x, 0, z) = \nabla S / |\nabla S|$ and $\partial \boldsymbol{e}_y / \partial y = 0$. A direction must be chosen for either $\boldsymbol{e}_x(x, 0, z)$ or $\boldsymbol{e}_z(x, 0, z)$, then the other is formed through the appropriate cross product. This allows $g_{ij}(x, y, z)$ to be fixed based on information from the surface S only, as shown in equations 3.8 and 3.9. R_x and R_z are the radii of curvature in the x and z directions, respectively. (The equations for the radii originate from the definition of the curvature of a line embedded in a surface, where the curve in this case is a specific coordinate.) The equations for h_x and h_z are related to how the arc length of a circular segment increases as the radius increases. The radii of curvature are typically calculated for the entire surface S ahead of time and then used where needed for a particular calculation.

$$[g_{ij}] = \begin{bmatrix} \left(1 + \frac{y}{R_x}\right)^2 & 0 & 0 \\ 0 & 1 & 0 \\ 0 & 0 & \left(1 + \frac{y}{R_z}\right)^2 \end{bmatrix} \tag{3.8}$$

$$R_x(x, z) = \left| \frac{\partial \boldsymbol{e}_x(x, z)}{\partial x} \right|^{-1} \tag{3.9a}$$

$$R_z(x,z) = \left| \frac{\partial \boldsymbol{e}_z(x,z)}{\partial z} \right|^{-1} \tag{3.9b}$$

3.1.2 Clustering

Once the metrics for the orthogonal coordinate system have been calculated, one further step involving coordinate systems must be taken. Problems that require discretization of the boundary layer typically employ clustering near the wall, then taper off spacing as distance away from the wall increases. BLAST is no different. Many options have been implemented in the code, but any clustering is based on the function first used by Malik [47] in equation 3.10. This is a one-dimensional clustering based on two parameters: y_c, which is the y-location where the middle point will be placed, and y_e, the end of the domain. y is assumed to begin at 0. y_c is typically chosen to be the boundary-layer height and y_e is chosen to be some distance far enough away that all perturbations have died off. b is a coordinate from the computational coordinate system mentioned earlier in the section. For the stability domain, a is constant and $b, c \in [0, 1]$ with equal spacing between points. The equal spacing is necessary for the finite differences used to approximate the derivatives in the SBG equations.

$$y = \frac{y_c b}{m_1 - m_2 b} \tag{3.10a}$$

$$m_1 = 1 - \frac{y_c}{y_e} \tag{3.10b}$$

$$m_2 = 1 - 2\frac{y_c}{y_e} \tag{3.10c}$$

If y_e and y_c are provided as functions of z and are smooth, then transformations between coordinate system O and the computational frame can be formulated based on $(x(a), y(b,c), z(c))$. An important note is that for the orthogonal section of BLAST, the equations are cast in the O frame, but all spatial derivatives must be transformed into derivatives of the computational coordinates

for the finite differences. Therefore, when transforming vector components of the solution $\hat{\phi}$, they are only transformed from O to C coordinates or to their physical components in O. (Physical components of a vector are components that are still in their current frame, but are adjusted by a function of the metric tensor such that they are directly comparable with components of the same vector in a Cartesian frame. This also ensures that the physical components all have the correct units. Details on this idea can be found in Truesdell [48].)

3.1.3 Surface Generation and Interpolation

So far, it has been taken for granted that a SBG grid point can be placed anywhere on the surface S. However, this usually requires interpolation of the coordinates of the surface itself, and can prove problematic. BLAST reads in data in structured form, meaning that the dataset consists of many irregular hexahedra, with data provided at each vertex. (The hexahedra are irregular because each side is not planar.)

There are multiple methods to find a point in three-dimensional space that intersects S in between points when S is not defined analytically, each requiring different assumptions. In BLAST, the solution is found through orthogonal regression [49]. Four points are used to find a plane whose orthogonal distance to each point is minimized, passing through the average of all four points. When the points are already coplanar, that plane is used. The algorithm implemented in BLAST was adapted from reference [50]. The query is found on S by using some guess defined in the C frame. It is then projected onto the local plane definition of S either along some direction, usually based on a Cartesian coordinate direction or distance from an axis of the body of interest.

This is not a perfect solution. One of the detriments of this method is that in general the plane does not intersect any of the four points used to generate it. To deal with edge cases, query points are automatically assigned the value of one of the four points if the distance is below some tolerance. Higher-order methods were explored that took into account multiple sets of four surface points, but that introduced problems of their own that led those methods to be abandoned. Regions on the surface that were not C^2 continuous, like where a cylindrical leading edge transitions to a plane, behaved poorly. Spurious wiggles also appeared on occasion. In the end, errors associated

with the discretization error of the surface decrease as the number of surface-grid points increase. Therefore, using this method should not introduce any error of a larger order of magnitude than that of the Computational Fluid Dynamics (CFD) code's handling of the surface.

Distance along S in the $\boldsymbol{e}_z$ direction is curved. To ensure that this distance can be accurately computed, a bisection method along the curve is used to determine when new points are needed. A segment of a curve is bisected until the sum of the Cartesian distances of two segments is within some tolerance to the Cartesian distance calculated from the first to the last point. This ensures that z can be accurately calculated to within the discretization error. Then, the z points of the grid are placed either equally spaced in z, or according to the 1-D clustering in equation 3.10a.

3.2 Nonorthogonal Code

There are times when a surface-based, orthogonal coordinate system is not amenable to the geometry of the body of interest. For instance, consider a geometry like that of figure 3.1. A positive R represents a concave-down surface with respect to the wall-normal direction, while a negative R indicates a concave-up surface. In the limit of $R \to \pm\infty$, the surface becomes flat and the metric tensor reduces to that of the Cartesian coordinate system, $g_{ij} = \delta_{ij}$. However, when $R < 0$, y must be limited to $0 \leq y < |R|$, or else the coordinate lines from different z locations will cross. When it is necessary for the solution domain to extend beyond $y = |R|$, due to the physical extent of the computed instability or features in the unperturbed solution, more complicated coordinate systems must be used.

For the fully nonorthogonal coordinate system, all components of g_{ij} become nonzero. In order to apply equations 2.4 to a general coordinate system, the following definitions are needed.

The components of a gradient of a vector can be written as

$$u_N{}^i_{,j} = \frac{\partial u_N{}^i}{\partial \xi^j} + \Gamma^i_{jk} u_N{}^k \tag{3.11}$$

where Γ^i_{jk} is a Christoffel symbol of the second kind, defined by

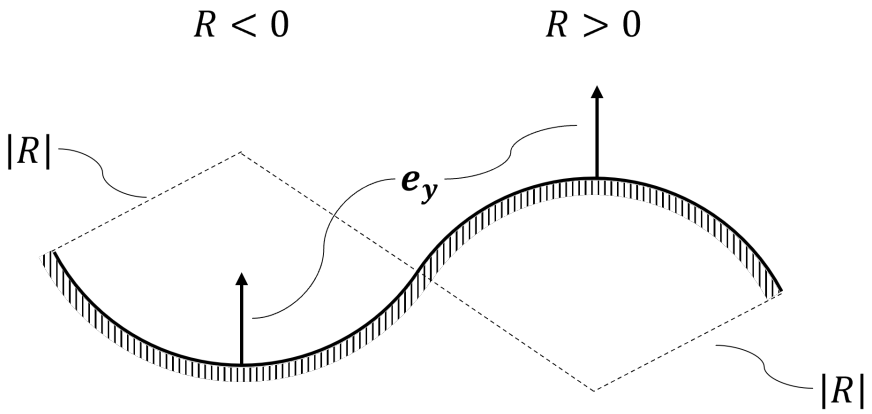

Figure 3.1: Example of positive and negative surface curvature as used by the orthogonal coordinate system in BLAST. Adapted from Riha et al. [51].

$$\Gamma^i_{jk} = \frac{1}{2} g^{il} \left(\frac{\partial g_{lj}}{\partial \xi^k} + \frac{\partial g_{lk}}{\partial \xi^j} - \frac{\partial g_{jk}}{\partial \xi^l} \right) \tag{3.12}$$

The gradient of a scalar remains the same as in equation 3.2. Defining $J \equiv \sqrt{\det[g_{ij}]}$, the divergence of a vector is

$$\nabla \cdot \boldsymbol{v} = u_{N^i,i} = \frac{1}{J} \frac{\partial}{\partial \xi^i} \left(J u_N{}^i \right) \tag{3.13}$$

3.2.1 Wave Components

The wave component for LST was originally introduced as $\exp(i(\alpha\xi + \beta\zeta - \omega t))$. However, it is not immediately clear how this form transforms. Instead, the wave component can be written in vector form, as the gradient of a scalar function.

$$\phi'(\xi^j, t) = A_0 \hat{\phi}(\eta) e^{i\theta} + c.c. \tag{3.14a}$$

$$\frac{\partial \theta}{\partial t} = -\omega \tag{3.14b}$$

$$\frac{\partial \theta}{\partial \xi^j} = k_{Nj} - i\sigma_{Nj} \tag{3.14c}$$

k_{Nj} and σ_{Nj} are the components of the wavenumber and growth vectors: $\boldsymbol{k} = k_{Nj} g^{jl} \boldsymbol{a}_l$ and

$\boldsymbol{\sigma} = \sigma_{Nj} g^{jl} \boldsymbol{a}_l$. (Recall that in Chapter 2 was defined using $\sigma_{N1} = -\Im(\alpha_N)$). From here, it is clear that the wavenumber is covariant and transforms according to equation 3.15.

$$k_{Cj} = \frac{\partial \xi^l}{\partial X^j} k_{Nl} \tag{3.15}$$

However, there are not three components of k_{Nj} in SBG, but only one. In order to use k_N, it needs to have units of k_C, but in the same direction as $\boldsymbol{a}_\xi$. Since there is only one component, the magnitude of $\boldsymbol{k}$ can be used to convert k_N into appropriate units.

$$\begin{aligned} |\boldsymbol{k}| &= \sqrt{k_{Nj} k_{Nl} g^{jl}} \\ &= k_{N1} \sqrt{g^{11}} \end{aligned} \tag{3.16}$$

Therefore, all reported values of α from nonorthogonal equations correspond to $\alpha_N \sqrt{g^{11}}$.

For phase velocity, another important quantity, the vector definition is given by Whitham [52] in equation 3.17a. The magnitude of $\boldsymbol{c}_{ph}$ shows how fast a monochromatic instability propagates in the boundary layer, and often helps identify different types of disturbances.

$$\boldsymbol{c}_{ph} = \frac{\omega \boldsymbol{k}}{|\boldsymbol{k}|^2} \tag{3.17a}$$

$$|\boldsymbol{c}_{ph}| = \frac{\omega}{k_{N1} \sqrt{g^{11}}} \tag{3.17b}$$

3.2.2 Interpretation of Nonorthogonal Results

An important point to note is that in the nonorthogonal frame, α_N is constant everywhere along the solution, while in any other frame, it varies from point to point with through $\sqrt{g^{11}}$. This begs the question, how should α be reported so that it is useful to other researchers?

Some inspiration can be drawn from LST and PSE results. When using a orthogonal curvilinear system like that described in 3.1, equation 3.16 becomes $|\boldsymbol{k}| = k_{O1} h^1$ (see the equations reported in Zanus, for instance [53]). However, whenever α is reported, the scaling factors are often dropped.

This can be interpreted as reporting the value of α at the wall, where $h_1 = h_3 = 1$. Here, the same will be done: $\sqrt{g^{11}}$ will be extracted from the wall at the location corresponding with the maximum of the absolute value of the pressure perturbation.

3.2.3 Physical Components

On occasion, it will be helpful to display a vector or tensor quantity in the nonorthogonal frame, but in a way that can be compared with its components in an orthonormal frame. For this purpose, physical components will be used [48]. Physical components for vectors can be understood intuitively by taking the length of the basis vector and shifting it to be contained in the vector component. For instance, the following equation shows how to derive the physical component of a velocity component.

$$\begin{aligned} u_N \boldsymbol{a}_\xi &= u_N \left|\boldsymbol{a}_\xi\right| \hat{\boldsymbol{a}}_\xi \\ &= u_N \sqrt{\boldsymbol{a}_\xi \cdot \boldsymbol{a}_\xi} \hat{\boldsymbol{a}}_\xi \\ &= u_N \sqrt{g_{11}} \hat{\boldsymbol{a}}_\xi \\ &= \check{u}_N \hat{\boldsymbol{a}}_\xi \end{aligned} \tag{3.18}$$

In equation 3.18, $|\boldsymbol{a}_\xi|$ is folded into $\check{u}_N$, leading to the physical component of a contravariant vector to be defined as

$$\check{u}_N{}^j = u_N{}^j \sqrt{g_{jj}} \qquad \text{(no sum on } j\text{)} \tag{3.19}$$

Physical components of covariant vectors are similarly defined:

$$\check{k}_{Nj} = k_{Nl} g^{lj} \sqrt{g_{jj}} \qquad \text{(no sum on } j\text{)} \tag{3.20}$$

Physical components will be designated with $\check{}$. It is important to note that physical components of vectors that were originally covariant or contravariant are no longer so. Truesdell [48] and Aris [46] use a different index notation to signify the difference ($\check{u}_N{}^j = u_N(j)$). This notation will not be used in this work.

3.3 Boundary Conditions

3.3.1 Dirichlet

Boundary conditions at the domain edges are required to complete the problem definition. Eigenvalue problems require homogeneous boundary conditions, so only a few are available. Dirichlet conditions are when components of $\hat{\phi}$ are set to 0 (equation 3.21). For $\hat{u}$, $\hat{v}$, and $\hat{w}$ (in any frame), this boundary condition is used to enforce no-slip conditions at solid boundaries. $\hat{T} = 0$ is used when a boundary is assumed to be isothermal. $\hat{\rho} = 0$ is rarely used as a physical boundary condition. Dirichlet conditions may also be used at domain edges that are far enough away from the region where the eigenfunction is active to ensure that the solution fully dies off, but this is difficult to predict a priori; these use cases fall more into the category of "numerical" boundary conditions than mathematically rigorous ones.

$$\hat{\boldsymbol{\phi}} = \mathbf{0} \tag{3.21}$$

3.3.2 Neumann

The next common type of boundary condition is Neumann conditions. These take different forms for the scalar and vector parts of $\hat{\phi}$. Note that equation 3.22a is the gradient of a vector, while equations 3.22b and 3.22b are the gradients of a scalar.

$$\nabla \hat{\boldsymbol{u}} \cdot \hat{\boldsymbol{n}} = \mathbf{0} \tag{3.22a}$$

$$\nabla \hat{T} \cdot \hat{\boldsymbol{n}} = 0 \tag{3.22b}$$

$$\nabla \hat{\rho} \cdot \hat{\boldsymbol{n}} = 0 \tag{3.22c}$$

$\hat{\boldsymbol{n}}$ is a unit normal vector to the boundary where the conditions are being imposed. For example, if the boundary was $\zeta = 1$, the definition would be

$$\hat{\boldsymbol{n}} = \frac{\boldsymbol{a}_1 \times \boldsymbol{a}_2}{|\boldsymbol{a}_1 \times \boldsymbol{a}_2|} \tag{3.23}$$

This cross product can then be written as

$$\begin{aligned} \boldsymbol{a}_1 \times \boldsymbol{a}_2 &= \epsilon_{ljk} J \delta^{j1} \delta^{k2} g^{il} \boldsymbol{e}_i \\ &= \epsilon_{l12} J g^{il} \boldsymbol{e}_i \\ \boldsymbol{a}_1 \times \boldsymbol{a}_2 &= J g^{i3} \boldsymbol{a}_i \end{aligned} \tag{3.24}$$

ϵ_{ljk} is the absolute covariant Levi-Civita tensor. The magnitude of $\boldsymbol{a}_1 \times \boldsymbol{a}_2$ is shown in equation 3.25

$$\begin{aligned} |\boldsymbol{a}_1 \times \boldsymbol{a}_2| &= \sqrt{J g^{i3} J g^{j3} g_{ij}} \\ &= J \sqrt{g^{i3} \delta_i^3} \\ |\boldsymbol{a}_1 \times \boldsymbol{a}_2| &= J \sqrt{g^{33}} \end{aligned} \tag{3.25}$$

Combining equations 3.24 and 3.25, the final definition for the unit normal vector at the $\zeta = 1$ is

$$\hat{\boldsymbol{n}} = \frac{g^{i3}}{\sqrt{g^{33}}} \boldsymbol{a}_i \tag{3.26}$$

To avoid any confusion as to which indices are contracted in equation 3.22a, it is shown in indicial notation in equation 3.27 (using the same boundary vector).

$$\left(\frac{\partial \hat{u}_N^i}{\partial \xi^j} + \Gamma_{jk}^i \hat{u}_N^k \right) \frac{g^{j3}}{\sqrt{g^{33}}} = 0^i \tag{3.27}$$

Neumann conditions are commonly used as symmetry or asymptotic conditions. Equation 3.22b is also used when a solid boundary is assumed to be adiabatic, and that the perturbation is not significant enough to alter the heat flux through the boundary.

3.3.2.1 Symmetry

Symmetry conditions do not consist of Neumann conditions on their own. True symmetry conditions involve forcing there to be no component of velocity penetrating the boundary. This can be achieved by equations 3.28. Initially, this appears to be four equations for three velocity components, but it is not. When the second-order tensor $\nabla\left(\hat{\boldsymbol{u}} - \left(\hat{\boldsymbol{u}} \cdot \hat{\boldsymbol{n}}\right)\hat{\boldsymbol{n}}\right)$ is expressed in a coordinate system, the resulting matrix will be rank-deficient. Therefore, this matrix should be reduced to row echelon form, and then the null row removed. Now, equation 3.28a represents two equations, and the third is supplied by equation 3.28b.

$$\nabla\left(\hat{\boldsymbol{u}} - \left(\hat{\boldsymbol{u}} \cdot \hat{\boldsymbol{n}}\right)\hat{\boldsymbol{n}}\right) \cdot \hat{\boldsymbol{n}} = \mathbf{0} \tag{3.28a}$$

$$\hat{\boldsymbol{u}} \cdot \hat{\boldsymbol{n}} = 0 \tag{3.28b}$$

3.3.3 Periodic

Periodic conditions can be stated a number of ways. In BLAST, periodic conditions are imposed by matching the derivative and value of two opposing boundaries, emulating a Taylor series. If periodic boundary conditions are imposed on the $\zeta = 0$ and $\zeta = 1$ boundaries, then the $\zeta = 0$ boundary will have

$$\left(\nabla\hat{\boldsymbol{u}} \cdot \hat{\boldsymbol{n}}\right)\big|_{\zeta=0} = \left(\nabla\hat{\boldsymbol{u}} \cdot \hat{\boldsymbol{n}}\right)\big|_{\zeta=1} \tag{3.29a}$$

$$\left(\nabla\hat{T} \cdot \hat{\boldsymbol{n}}\right)\Big|_{\zeta=0} = \left(\nabla\hat{T} \cdot \hat{\boldsymbol{n}}\right)\Big|_{\zeta=1} \tag{3.29b}$$

$$\left(\nabla\hat{\rho} \cdot \hat{\boldsymbol{n}}\right)\big|_{\zeta=0} = \left(\nabla\hat{\rho} \cdot \hat{\boldsymbol{n}}\right)\big|_{\zeta=1} \tag{3.29c}$$

On the $\zeta = 1$ boundary, the following equations will be enforced:

$$\hat{\boldsymbol{u}}\big|_{\zeta=0} = \hat{\boldsymbol{u}}\big|_{\zeta=1} \tag{3.30a}$$

$$\hat{T}\Big|_{\zeta=0} = \hat{T}\Big|_{\zeta=1} \tag{3.30b}$$

$$\hat{\rho}|_{\zeta=0} = \hat{\rho}|_{\zeta=1} \tag{3.30c}$$

3.4 Solution Procedures

Next, the methods used to solve the equations will be discussed. For convenience, two of the relevant equation sets from Chapter 2 will be repeated here. α can be regarded as either α_O or α_N depending which set of equations are used.

$$\boldsymbol{\mathcal{A}}\frac{\partial^2\hat{\boldsymbol{\phi}}}{\partial\eta^2}+\boldsymbol{\mathcal{B}}\frac{\partial^2\hat{\boldsymbol{\phi}}}{\partial\eta\partial\zeta}+\boldsymbol{\mathcal{C}}\frac{\partial^2\hat{\boldsymbol{\phi}}}{\partial\zeta^2}+(\boldsymbol{\mathcal{D}_0}+\alpha\boldsymbol{\mathcal{D}_1})\frac{\partial\hat{\boldsymbol{\phi}}}{\partial\eta}+(\boldsymbol{\mathcal{E}_0}+\alpha\boldsymbol{\mathcal{E}_1})\frac{\partial\hat{\boldsymbol{\phi}}}{\partial\zeta}+(\boldsymbol{\mathcal{F}_0}+\alpha\boldsymbol{\mathcal{F}_1}+\alpha^2\boldsymbol{\mathcal{F}_2})\hat{\boldsymbol{\phi}}=\mathbf{0} \tag{2.18}$$

$$\boldsymbol{\mathcal{M}_1} = \left[\begin{array}{c|c} \boldsymbol{\mathcal{A}}\frac{\partial^2}{\partial\eta^2}+\boldsymbol{\mathcal{B}}\frac{\partial^2}{\partial\eta\partial\zeta}+\boldsymbol{\mathcal{C}}\frac{\partial^2}{\partial\zeta^2}+\boldsymbol{\mathcal{D}_0}\frac{\partial}{\partial\eta}+\boldsymbol{\mathcal{E}_0}\frac{\partial}{\partial\zeta}+\boldsymbol{\mathcal{F}_0} & \boldsymbol{0}^{5\times4} \\ \hline \boldsymbol{0}^{4\times5} & \boldsymbol{\mathcal{I}}^{4\times4} \end{array}\right] \tag{2.19a}$$

$$\boldsymbol{\mathcal{M}_2} = -\left[\begin{array}{c|c} \boldsymbol{\mathcal{D}_1}\frac{\partial}{\partial\eta}+\boldsymbol{\mathcal{E}_1}\frac{\partial}{\partial\zeta}+\boldsymbol{\mathcal{F}_1} & \boldsymbol{\mathcal{F}_{2R}} \\ \hline \boldsymbol{\mathcal{I}}^{4\times4} & \boldsymbol{0}^{4\times5} \end{array}\right] \tag{2.19b}$$

$$\hat{\boldsymbol{\Phi}}^T = \left[\begin{array}{ccccc|cccc} \hat{u} & \hat{v} & \hat{w} & \hat{T} & \hat{\rho} & \alpha\hat{u} & \alpha\hat{v} & \alpha\hat{w} & \alpha\hat{T} \end{array}\right] \tag{2.19c}$$

$$\boldsymbol{\mathcal{M}_1}\hat{\boldsymbol{\Phi}} = \alpha\boldsymbol{\mathcal{M}_2}\hat{\boldsymbol{\Phi}} \tag{2.19d}$$

3.4.1 Arnoldi Method

Equation 2.19d is still a continuous eigenvalue problem. No useful analytical solutions are known, so the domain must be discretized, and the derivatives must be numerically approximated. n_y will refer to the amount of points in the y or η dimension, and n_z is the number of points in the z or ζ dimension. In addition, derivatives are approximated through finite differences, which will be discussed in section 3.5. Once the problem is discretized, the core 9×9 blocks are organized

into one large matrix, starting with the y dimension as the inner loop and the z dimension as the outer loop.

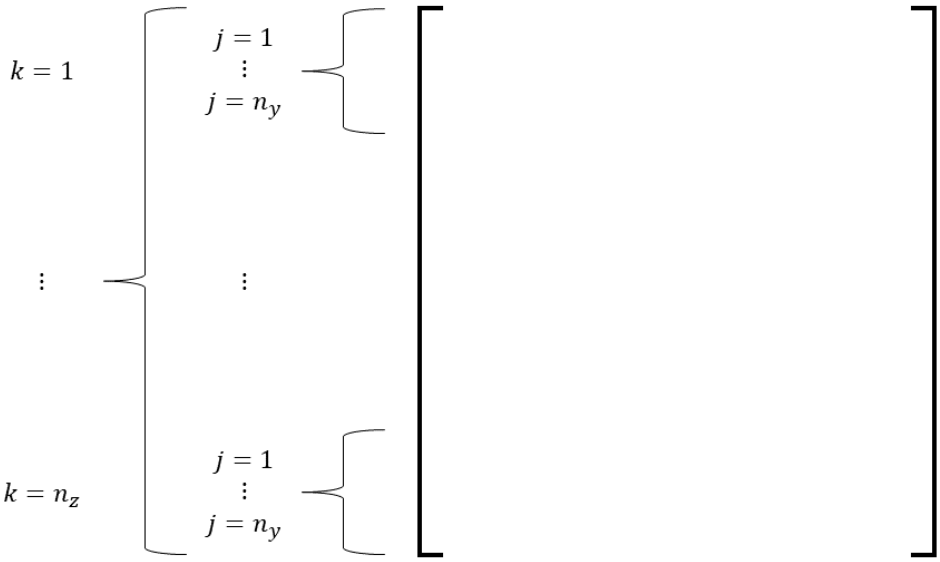

Figure 3.2: Diagram of the way the matrices are organized in BLAST.

Let $\tilde{\boldsymbol{\mathcal{M}}}_{\mathbf{1}}$ and $\tilde{\boldsymbol{\mathcal{M}}}_{\mathbf{2}}$ be the discretized forms of the matrices. These are sparse, square matrices with $9n_yn_z$ rows. The sizes involved require the use of sparse storage methods and sparse arithmetic. For instance, to store a double-precision complex $\tilde{\boldsymbol{\mathcal{M}}}_{\mathbf{1}}$ when $n_y = n_z = 400$ in a dense format would require roughly 30 terabytes of memory. This is a common grid size for realistic problems. Alternatively, the use of a sparse matrix form such as Coordinate (COO) format likely requires less than 3 gigabytes of memory, depending on the construction method. BLAST uses the open-source SPARSKIT library [54] to convert between various sparse formats, and for sparse versions of some linear-algebra operations.

Finding all of the eigenvalues and eigenvectors for a particular problem is currently intractable for all but the smallest problems. Luckily, modal instability theory is based on the premise that the long-time (or long-space) behavior of a single mode, or eigenvalue, dominates the system. So in

practice, only a few eigenvalues are usually needed for a particular frequency.

In BLAST, Arnoldi's method (or Arnoldi's algorithm) is used to find a subset of the eigenvalues of the discretized form of equation 2.19d. This algorithm is originally introduced by Arnoldi [55] and described in detail by Saad as Algorithm 3.1 [56]. The core idea is to find a Krylov subspace that has a much smaller dimension than the original matrix, but contains approximations to the same eigenvalues as the original system. Then a standard QZ algorithm can be employed to find all of the eigenvalues and eigenvectors of the subspace, which become Ritz values and vectors of the original space. Saad [56] mentions a danger that the vectors used to span the subspace can become not properly orthogonal due to the accumulation of errors with floating-point arithmetic, and mentions a reorthogonalization scheme to correct this. However, this has not proven to be an issue in the solution of various SBG problems, so the basic algorithm is the one used in BLAST.

The Arnoldi method finds the largest eigenvalues of a given matrix, resolving more eigenvalues as the dimension of the Krylov subspace increases. This dimension will be denoted as $n_{Arnoldi}$. In order to use the Arnoldi method efficiently, a shift-and-invert method is used to remap a guess for the eigenvalue of the original system to be among the largest of a new matrix. Therefore, an initial guess for α must be provided. This is usually calculated through the phase speed, along with a "reasonably" negative value for the imaginary part. Experience has shown the real part of α to be by far the most important part of the guess to get right, with very little dependence on $\Im(\alpha)$.

This new matrix equation is constructed through the following equations.

$$\boldsymbol{\mathcal{A}}_{Shift} = (\tilde{\boldsymbol{\mathcal{M}}}_{\mathbf{1}} - \alpha_{Guess}\tilde{\boldsymbol{\mathcal{M}}}_{\mathbf{2}})^{-1}\tilde{\boldsymbol{\mathcal{M}}}_{\mathbf{2}} \tag{3.32a}$$

$$\alpha_{Shift} = \frac{1}{\alpha - \alpha_{Guess}} \tag{3.32b}$$

$$\boldsymbol{\mathcal{A}}_{Shift}\hat{\boldsymbol{\Phi}}_{Shift} = \alpha_{Shift}\hat{\boldsymbol{\Phi}}_{Shift} \tag{3.32c}$$

The goal is to create $\boldsymbol{\mathcal{H}}$, the Hessenberg matrix whose $n_{Arnoldi}$ column vectors span the Krylov subspace of $\boldsymbol{\mathcal{A}}_{Shift}$. The Arnoldi method requires, among other things, the repeated calculation of $\boldsymbol{b}$ through $\boldsymbol{\mathcal{A}}_{Shift}\boldsymbol{x} = \boldsymbol{b}$, where $\boldsymbol{x}$ is another known vector created in the algorithm. Solving for

$\boldsymbol{\mathcal{A}}_{Shift}$ directly through inversion of $(\tilde{\boldsymbol{\mathcal{M}}}_{\mathbf{1}} - \alpha_{Guess}\tilde{\boldsymbol{\mathcal{M}}}_{\mathbf{2}})$ would be computationally expensive in terms of both run time and memory. Instead, this matrix vector product is performed in two steps. $\boldsymbol{\mathcal{A}}_{Shift}\boldsymbol{x} = \boldsymbol{b}$ can be rearranged as shown below.

$$\begin{aligned} \boldsymbol{\mathcal{A}}_{Shift}\boldsymbol{x} &= \boldsymbol{b} \\ (\tilde{\boldsymbol{\mathcal{M}}}_{\mathbf{1}} - \alpha_{Guess}\tilde{\boldsymbol{\mathcal{M}}}_{\mathbf{2}})^{-1}\tilde{\boldsymbol{\mathcal{M}}}_{\mathbf{2}}\boldsymbol{x} &= \boldsymbol{b} \\ (\tilde{\boldsymbol{\mathcal{M}}}_{\mathbf{1}} - \alpha_{Guess}\tilde{\boldsymbol{\mathcal{M}}}_{\mathbf{2}})\boldsymbol{b} &= \tilde{\boldsymbol{\mathcal{M}}}_{\mathbf{2}}\boldsymbol{x} \end{aligned} \tag{3.33}$$

First, the LU decomposition of $(\tilde{\boldsymbol{\mathcal{M}}}_{\mathbf{1}} - \alpha_{Guess}\tilde{\boldsymbol{\mathcal{M}}}_{\mathbf{2}})$ is taken and stored. This is an expensive step, but it must be done only once per Arnoldi algorithm. Then, to solve for $\boldsymbol{b}$, $\boldsymbol{x}$ is premultiplied by $\tilde{\boldsymbol{\mathcal{M}}}_{\mathbf{2}}$, then the LU factors are applied to that product. This step is much cheaper, but must be done $n_{Arnoldi}$ times. Once $\boldsymbol{\mathcal{H}}$ has been built, all of its eigenvalues and eigenvectors are calculated using a QZ algorithm. The resulting eigenvalues approximate α_{Shift} which then have the shift operation of equation 3.32b undone. The eigenvectors are converted from eigenvectors of $\boldsymbol{\mathcal{H}}$ to approximate eigenvectors of equation 2.19d through an auxiliary matrix that is built during the Arnoldi algorithm. The accuracy of the resulting α and $\hat{\boldsymbol{\Phi}}$ solutions directly depends on $|\alpha - \alpha_{Guess}|$ and $n_{Arnoldi}$ [19]. Accuracy is increased through either a better guess or a larger Krylov subspace.

To perform the LU decomposition, a parallel library for sparse systems is used called MUMPS [57]. It uses a multifrontal method to calculate the decomposition in parallel while maintaining reasonable levels of sparsity, and memory usage as a result. For the QZ algorithm and the solution of smaller, dense linear systems throughout BLAST, LAPACK is used [58]. OpenMP shared-memory parallelization is also employed wherever possible to reduce overall run time.

3.4.2 Newton–Raphson Convergence

The α and $\hat{\phi}$ solution that comes out of the Arnoldi technique, as previously mentioned, is approximate. Another method is needed to converge this solution to whatever the required level of precision might be. For this purpose, a Newton–Raphson technique was chosen, adapted from one described by Moyes et al. [45]. The equations that are converged are shown below:

$$\boldsymbol{F_{NR}} = \begin{bmatrix} \boldsymbol{f_{NR_1}} \\ f_{NR_2} \end{bmatrix} = \boldsymbol{0} \tag{3.34a}$$

$$\begin{aligned} \boldsymbol{f_{NR_1}} = \Bigg(& \boldsymbol{\mathcal{A}} \frac{\partial^2}{\partial \eta^2} + \boldsymbol{\mathcal{B}} \frac{\partial^2}{\partial \eta \partial \zeta} + \boldsymbol{\mathcal{C}} \frac{\partial^2}{\partial \zeta^2} + (\boldsymbol{\mathcal{D}_0} + \alpha \boldsymbol{\mathcal{D}_1}) \frac{\partial}{\partial \eta} \\ & + (\boldsymbol{\mathcal{E}_0} + \alpha \boldsymbol{\mathcal{E}_1}) \frac{\partial}{\partial \zeta} + (\boldsymbol{\mathcal{F}_0} + \alpha \boldsymbol{\mathcal{F}_1} + \alpha^2 \boldsymbol{\mathcal{F}_2}) \Bigg) \hat{\boldsymbol{\phi}} \end{aligned} \tag{3.34b}$$

$$f_{NR_2} = \hat{\boldsymbol{\phi}}^T \hat{\boldsymbol{\phi}} - 1 \tag{3.34c}$$

$\boldsymbol{F_{NR}}$ is a vector of length $5n_y n_z + 1$. (The indices are to be regarded as linear algebra indices and do not imply any tensorial character.) Since an eigenvector is only unique to within a multiplicative constant, f_{NR_2} is added as a normalization equation to make the final α and $\hat{\boldsymbol{\phi}}$ solution unique. The Jacobian of this with system respect to α and $\hat{\boldsymbol{\phi}}$ is given by equation 3.35.

$$\boldsymbol{\mathcal{J}_{NR}} = \begin{bmatrix} \boldsymbol{\mathcal{J}_{NR11}} & \boldsymbol{J_{NR12}} \\ \boldsymbol{J_{NR21}}^T & J_{NR22} \end{bmatrix} = \begin{bmatrix} \dfrac{\partial \boldsymbol{f_{NR_1}}}{\partial \hat{\boldsymbol{\phi}}} & \dfrac{\partial \boldsymbol{f_{NR_1}}}{\partial \alpha} \\ \dfrac{\partial f_{NR_2}}{\partial \hat{\boldsymbol{\phi}}} & \dfrac{\partial f_{NR_2}}{\partial \alpha} \end{bmatrix} \tag{3.35a}$$

$$\begin{aligned} \boldsymbol{\mathcal{J}_{NR11}} = & \boldsymbol{\mathcal{A}} \frac{\partial^2}{\partial \eta^2} + \boldsymbol{\mathcal{B}} \frac{\partial^2}{\partial \eta \partial \zeta} + \boldsymbol{\mathcal{C}} \frac{\partial^2}{\partial \zeta^2} + (\boldsymbol{\mathcal{D}_0} + \alpha \boldsymbol{\mathcal{D}_1}) \frac{\partial}{\partial \eta} \\ & + (\boldsymbol{\mathcal{E}_0} + \alpha \boldsymbol{\mathcal{E}_1}) \frac{\partial}{\partial \zeta} + (\boldsymbol{\mathcal{F}_0} + \alpha \boldsymbol{\mathcal{F}_1} + \alpha^2 \boldsymbol{\mathcal{F}_2}) \end{aligned} \tag{3.35b}$$

$$\boldsymbol{J_{NR12}} = \left(\boldsymbol{\mathcal{D}_1} \frac{\partial}{\partial \eta} + \boldsymbol{\mathcal{E}_1} \frac{\partial}{\partial \zeta} + (\boldsymbol{\mathcal{F}_1} + 2\alpha \boldsymbol{\mathcal{F}_2}) \right) \hat{\boldsymbol{\phi}} \tag{3.35c}$$

$$\boldsymbol{J_{NR21}} = 2\hat{\boldsymbol{\phi}} \tag{3.35d}$$

$$J_{NR22} = 0 \tag{3.35e}$$

The solution is then updated through the following equation, where i refers to the iteration count.

$$\begin{bmatrix} \hat{\phi} \\ \alpha \end{bmatrix}^{i+1} = \begin{bmatrix} \hat{\phi} \\ \alpha \end{bmatrix}^{i} - \omega_{relax} \left(\boldsymbol{\mathcal{J}_{NR}}^{-1} \boldsymbol{F_{NR}} \right)^{i} \tag{3.36}$$

ω_{relax} is a relaxation factor that can be used to help the algorithm converge if the first few iterations are too aggressive and overshoot the solution. Otherwise, ω_{relax} is set to unity. This technique can reliably push the magnitude of the residual, $|\boldsymbol{F_{NR}}|$, down to around 10^{-14} or lower. Depending on the accuracy of the initial solution, the method typically takes around 4–10 steps to converge. In terms of computational cost, the method described here is somewhat of a middle ground. The rank of the matrix that must be LU decomposed is lower compared to the Arnoldi technique ($5n_y n_z + 1$ vs $9n_y n_z$), but the LU decomposition must occur every iteration.

3.4.2.1 Solution Marching

When trying to track an instability in either frequency or space, a common use of this technique is to take the previous solution (in space or frequency) and it use it as the initial solution to be converged at the current conditions. Since this uses α and $\hat{\phi}$ to form the update in a coupled fashion, it is a much more reliable technique to follow an instability than solving multiple eigenvalue problems and manually sifting through the results to find the same disturbance.

This would be known as a 0$^{\text{th}}$-order approximation to the next solution. Unfortunately, sometimes this technique diverges. In order to improve reliability, 1$^{\text{st}}$- and 2$^{\text{nd}}$-order guesses at the next solution were implemented, shown in equations 3.37 and 3.38, respectively. (Equation 3.38, is formally mixed order, combining a 2$^{\text{nd}}$-order 1$^{\text{st}}$ derivative with a 1$^{\text{st}}$-order 2$^{\text{nd}}$ derivative. A fully 2$^{\text{nd}}$-order method would require 4 previous solutions.) Both of these equations were derived from a Taylor series expansion, and assume constant spacing in frequency or space between solutions. The extrapolations are applied to $\hat{\phi}$ as is, without any attempt to account for the movement of grid points relevative to a basic-state feature. In general, the 1$^{\text{st}}$-order extrapolation was found to be the most robust. The 2$^{\text{nd}}$-order sometimes gave a more accurate guess, but often failed in regions of significant enough change in the solution.

$$\alpha^i = 2\alpha^{i-1} - \alpha^{i-2} \tag{3.37}$$

$$\alpha^i = \frac{7}{2}\alpha^{i-1} - 4\alpha^{i-2} + \frac{7}{2}\alpha^{i-3} \tag{3.38}$$

3.5 Numerics

3.5.1 Finite Differences

BLAST was designed to use finite differences on account of their ease of implementation and expansion to higher orders. Another design choice was to use coefficients of the same order of approximation throughout the entire domain, including at the boundaries. There are pros and cons to this methodology. One benefit of this approach is that entire solution keeps the same order of accuracy. Mixed-order schemes have been observed to have the error of the solution be dominated by the lowest-order approximation within the method [59]. However, the dissipation and dispersion properties of the finite difference changes as the location within the stencil changes. A central difference scheme will in general be dissipative but nondispersive, but any one-sided schemes will add extra dispersion. In addition, one-sided stencils will have truncation error of the same order, but it will also in general be higher than that of a symmetric scheme.

For the spatial BiGlobal problem specifically, the equations are elliptic and typically used with a smooth basic state. This type of problem should be attacked by central stencils wherever possible. In addition, solutions typically have compact support in the basic state and die off toward the freestream, left, and right boundaries (for external flows). The only location where introducing one-sided differences has a significant effect is at the wall, where the basic-state boundary layer lives. This effect can be mitigated in large part by the use of significant clustering at the wall, which is already done to help ensure accuracy. Overall, there have been very few instances where the one-sided differences have shown to cause any adverse effects in BLAST.

Instead of manually inputting the relevant coefficients, BLAST sets the following system of linear equations to solve for the coefficients based on a few inputs.

$$A(i,j) = (j - i_{Stencil})^{i-1} \tag{3.39a}$$

$$b(i) = \begin{cases} n_{Order}!, & i = n_{Order} + 1 \\ 0, & \text{otherwise} \end{cases} \tag{3.39b}$$

$$\boldsymbol{\mathcal{A}}_{FD}\boldsymbol{x}_{FD} = \boldsymbol{b}_{FD} \tag{3.39c}$$

In equations 3.39, $\boldsymbol{\mathcal{A}}_{FD}$ is of rank $n_{Order} + n_{Approx}$, where n_{Order} is the order of the derivative and n_{Approx} is the order of the approximation. $i_{Stencil}$ is the location within the stencil where the derivative is being approximated. For instance, if the coefficients corresponding to a 4th-order approximation of a 2nd-order derivative at the 2nd point away from the wall were needed, that would correspond to $n_{Approx} = 4$, $n_{Order} = 2$, $i_{Stencil} = 2$. The derivative would then be approximated by

$$\frac{\partial f(i = i_{Stencil})}{\partial \eta} \approx \frac{\boldsymbol{f}(i = 1 : n_{Order} + n_{Approx}) \cdot \boldsymbol{x}_{FD}}{(\Delta\eta)^{n_{Order}}} \tag{3.40}$$

where $\Delta\eta$ is the step size in the η direction. For the orthogonal version of BLAST, this corresponds to the step size in the T frame, while in the nonorthogonal version this corresponds to the N frame directly. Like the T frame, the N frame is also scaled such that $\eta, \zeta \in [0, 1]$ for a particular domain.

In BLAST, terms like $\partial^2/\partial\eta^2$ and $\partial^2/\partial\zeta^2$ are calculated with coefficients arising from equation 3.39 solved with $n_{Order} = 2$, while the mixed derivative $\partial^2/(\partial\eta\partial\zeta)$ is calculated through successive application of the $n_{Order} = 1$ stencils for η and ζ, respectively. Calculating 2nd derivatives in this way reduces, but does not eliminate, the effects of odd-even decoupling.

3.5.1.1 Effects of Floating-Point Precision

One of the nice properties of finite-difference coefficients is that they can always be represented by a rational number. In addition, the sum of these coefficients is always zero. This results in finite differences perfectly recovering the fact that the derivative of a constant dataset is zero.

However, solving a linear system will not result in perfect rational numbers. BLAST is written

primarily in modern Fortran, which requires numbers to be represented by a constant type while math is performed. (Double precision is used almost everywhere throughout the code for real and complex types.) Numerical experiments that will be further detailed in section 4 revealed that small errors were appearing in derivatives of perfectly constant data. This was resolved by multiplying $\boldsymbol{x}_{FD}$ by $(n_{Order}+n_{Approx}-1)!$, rounding the result to the nearest integer, then dividing by $(n_{Order}+n_{Approx}-1)!$ again. This brought a particular relative error measure down from 10^{-12} to 10^{-14}. Granted, this could be improved by using a proper greatest-common-divisor algorithm to find the smallest integer to which each coefficient could be rounded, or splitting the application of the coefficients so that the numerators are applied first with integer math. However, this method was easily implemented and resulted in a noticeable error reduction in this particular case, so no further improvements were sought.

3.5.2 Buffer

While the unaltered finite-difference methodology described above works well for the vast majority of cases, there are some situations that have required special treatment. One of these occurs when shocks are present in the basic state. Eigenvectors concentrated around shocks will dominate any Arnoldi problems, and as a result extremely large values of $n_{Arnoldi}$ are required to get solutions to appear in the boundary layer, if they appear at all. However, sometimes the domain cannot be cutoff below the shocks, either due to a complicated shock structure or a shock that is very near the boundary layer. Both of these situations are hallmarks of hypersonic flow. In these cases, it is desirable to force the solution to go to zero in these regions. This can be accomplished through the use of a buffer region, that smoothly kills the solution in part of the domain.

In BLAST, equation 3.41 is used as when a buffer is needed. λ_{Buffer} is a spatially-varying scalar that is designed to overwhelm the SBG equations when it is large. ($\boldsymbol{\mathcal{I}}^{\dagger}$ is almost an identity matrix, except the rows corresponding to auxiliary equations needed for the companion-matrix approach are zeroed out. In other words, the diagonal of a 9×9 block of $\boldsymbol{\mathcal{I}}^{\dagger}$ would be $[1,1,1,1,1,1,0,0,0,0]^T$.) Note that as $\lambda_{Buffer}\rightarrow 0$, equation 3.41 reduces to equation 2.19d. When $\lambda_{Buffer}\rightarrow\infty$, equation 3.41 approaches 3.42, forcing $\hat{\phi}$ to 0.

$$\left(\boldsymbol{\mathcal{M}_1} + \lambda_{Buffer}\boldsymbol{\mathcal{I}}^{\dagger}\right)\hat{\boldsymbol{\Phi}} = \frac{\alpha}{1+\lambda_{Buffer}}\boldsymbol{\mathcal{M}_2}\hat{\boldsymbol{\Phi}} \tag{3.41}$$

$$\boldsymbol{\mathcal{I}}\hat{\boldsymbol{\phi}} = \boldsymbol{0}\hat{\boldsymbol{\phi}} \tag{3.42}$$

In order for the buffer to be effective, the function describing λ_{Buffer} must be smooth. Sharp changes in λ_{Buffer} can act the same as shocks in the basic-state and degrade the quality of the eigenvalue spectrum around a guess. BLAST uses a specifically designed $\tanh$ function for this purpose.

$$\lambda_{Buffer}(\eta,\zeta) = \lambda_{Max}\lambda_1(\eta)\lambda_2(\eta)\lambda_3(\zeta)\lambda_4(\zeta) \tag{3.43a}$$

$$\lambda_1 = \frac{1}{2}\left(1+\tanh\left(c_{BL}\left(\frac{2}{\lambda_{Ramp}}(\eta-\eta_{Min})+1\right)\right)\right) \tag{3.43b}$$

$$\lambda_2 = \frac{1}{2}\left(1+\tanh\left(-c_{BL}\left(\frac{2}{\lambda_{Ramp}}(\eta-\eta_{Max})+1\right)\right)\right) \tag{3.43c}$$

$$\lambda_3 = \frac{1}{2}\left(1+\tanh\left(c_{BL}\left(\frac{2}{\lambda_{Ramp}}(\zeta-\zeta_{Min})+1\right)\right)\right) \tag{3.43d}$$

$$\lambda_4 = \frac{1}{2}\left(1+\tanh\left(-c_{BL}\left(\frac{2}{\lambda_{Ramp}}(\zeta-\zeta_{Max})+1\right)\right)\right) \tag{3.43e}$$

In equations 3.43, λ_{Max} defines the large number for overwhelming the SBG equations, while λ_1–λ_4 control the activation of λ_{Buffer} in space. λ_1 and λ_2 set the η extent, while λ_1 and λ_2 define the ζ bounds. $c_{BL} \equiv \tanh^{-1}(0.99)$ and is used as the "boundary-layer height" of the $\tanh$ function. That way, η_{Min}, η_{Max} and the other bounds define the point where λ_{Buffer} equals 99% of λ_{Max}. λ_{Ramp} defines the extent of the "ramp-up region," where a value of $\lambda_{Ramp} = 0.1$ would imply that λ_1 ramps from 1% to 99% of λ_{Max} over a distance of 0.1 units in the local frame. This methodology usually requires trial and error for successful application to a specific problem, but once the parameters are tuned, it greatly reduces the value of $n_{Arnoldi}$ needed to find the important boundary-layer instabilities when there are shocks in a domain.

3.5.3 Filtering

4th-order finite differences are generally considered a "high-order" method, which some have defined as any scheme higher than 3rd order [60]. Unfortunately, it is nearly impossible to ensure that there will not be any noise in a basic-state, especially as the complexity of the solution increases. Use of high-order methods are known to be susceptible to the effects low-amplitude noise and produce extraneous wiggles that can contaminate the solution. One method to deal with these wiggles is the application of a filter designed to suppress high-wavenumber noise.

A 10th-order accurate filter developed and tested by Gaitonde et al. [60] is used in BLAST. To understand its effects, the spectral properties of both the finite differences and the filter will be analyzed.

Using an 11 point stencil centered at index 0, the filter applied to f to give a filtered function $\breve{f}$ can be written as

$$\breve{f}_0 = \sum_{j=0}^{5} \frac{c_{Filter\,j}}{2}(f_j + f_{-j}) \tag{3.44}$$

The amplification properties of this filter are shown in equation 3.45. ω_h is a wavenumber based on the spacing in between points, $\omega_h \equiv 2\pi\lambda/h$. With this definition, the Nyquist limit for discretely resolving a signal without aliasing corresponds to $\omega_h = \pi$. This would be equivalent to $2h$ (either $\Delta\eta$ or $\Delta\zeta$) per λ, where λ is a wavelength present in the solution.

$$A_{Filter}(\omega_h) = \frac{\breve{f}_0(\omega_h)}{f} = \sum_{j=0}^{5} c_{Filter\,j}\,\cos(j\omega_h) \tag{3.45}$$

Let the coefficients for 4th-order 1st and 2nd derivatives be represented according to equations 3.46 and 3.47, respectively.

$$\frac{\partial f_0}{\partial \eta} \approx \frac{1}{\Delta\eta}\sum_{i=1}^{3} c_{FD1\,i}(f_i - f_{-i}) \tag{3.46}$$

$$\frac{\partial^2 f_0}{\partial \eta^2} \approx \frac{1}{(\Delta\eta)^2} \sum_{i=0}^{3} c_{FD2i}(f_i + f_{-i}) \tag{3.47}$$

Similar amplification properties for the finite difference schemes can be found by comparing the ratio of the finite-difference approximation of the derivative a monochromatic wave to its analytical derivative. The spectral functions for the these schemes are then given by

$$A_{FD1}(\omega_h) = \frac{1}{\omega_h} \sum_{j=1}^{3} 2c_{FD1j} \sin(j\omega_h) \tag{3.48}$$

$$A_{FD2}(\omega_h) = \frac{-1}{\omega_h^2} \sum_{j=0}^{3} 2c_{FD2j} \cos(j\omega_h) \tag{3.49}$$

For reference, all of the coefficients for the central schemes mentioned above are given in table 3.1.

	c_0	c_1	c_2	c_3	c_4	c_5
1st Derivative		$\frac{45}{60}$	$\frac{-9}{60}$	$\frac{1}{60}$		
2nd Derivative	$\frac{-490}{360}$	$\frac{270}{180}$	$\frac{-27}{180}$	$\frac{2}{180}$		
Filter	$\frac{193}{256}$	$\frac{105}{256}$	$\frac{-15}{64}$	$\frac{45}{512}$	$\frac{-5}{512}$	$\frac{1}{512}$

Table 3.1: Coefficients for the finite difference and filter stencils in equations 3.44–3.49.

The first thing to notice about equations 3.45, 3.48, and 3.49 is that they are purely real. This implies that all of these schemes, including the filter, add dissipation only and are nondispersive. Next, $A_{FD} \leq 1$ for the ω_h range of interest, meaning no wavenumbers are amplified. The total amplification of the filter applied on top of the finite difference schemes is the product of their amplification functions, for instance $A_{Filter}A_{FD1}$. The individual amplifications, along with their product can be seen in figure 3.3 for first derivatives and figure 3.4 for second derivatives.

In figure 3.3, the blue line is the filter, the red line is the 1st-derivative finite difference, and

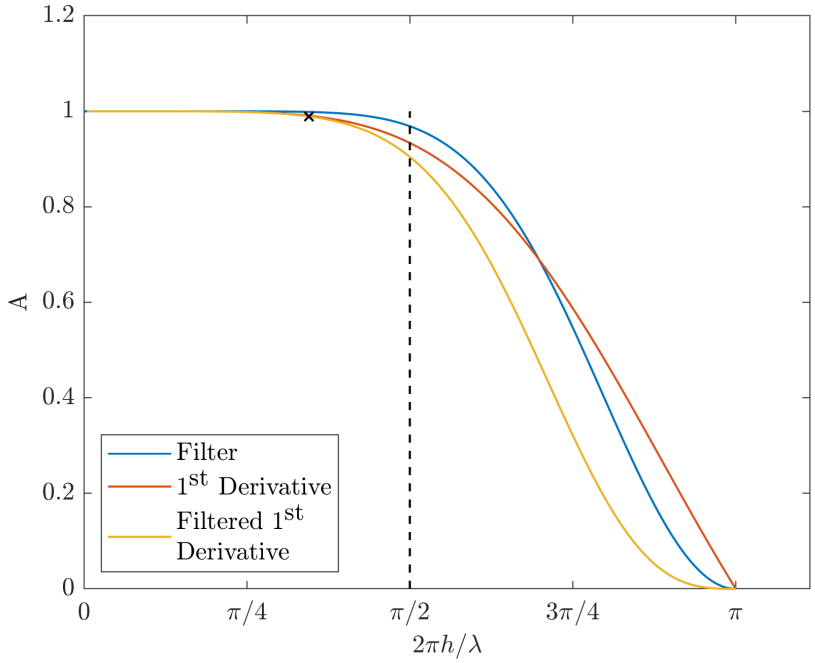

Figure 3.3: Amplification functions of the 1st-derivative finite difference, the filter, and their product. The black x is the location where the filtered derivative function reaches 0.99, which corresponds to $h/\lambda = 5.8$.

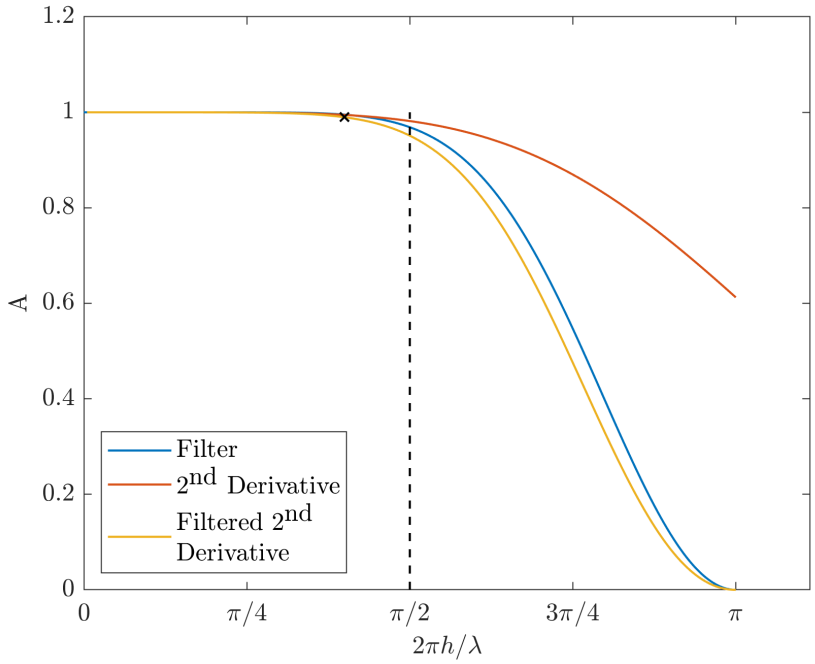

Figure 3.4: Amplification functions of the 2nd-derivative finite difference, the filter, and their product. The black x is the location where the filtered derivative function reaches 0.99, which corresponds to $h/\lambda = 5.0$.

the yellow line is their combined effect. The dashed line corresponds to $\omega_h = \pi/2$, or $h/\lambda = 4$. Qualitatively, the most aggressive damping occurs for wavenumbers beyond this point. The black x marks the wavenumber that is only damped to 99% of its true value, and this occurs at $h/\lambda = 5.8$. This would suggest that to resolve small scale structures well when using this scheme, there should be at least $6h$ per wavelength to avoid any extraneous damping of physical solutions. In figure 3.4, a notable difference is that $A_{FD2}(\pi) \neq 0$. Indeed, the high-wavenumber damping of the 2nd derivative without any filtering is much weaker than the 1st derivative. $\omega_h = \pi$, while technically resolvable theoretically, also corresponds to the odd-even-decoupling mode that can plague single-grid finite-difference schemes. Damping this mode out entirely in the 1st and 2nd derivatives is a major benefit of the filter. Finally, the black x in figure 3.4 corresponds to $h/\lambda = 5.0$, so the suggested value of $h/\lambda = 6$ is unaffected by the 2nd derivative.

This type of filter was investigated and applied by Visbal, Gaitonde and their colleagues in a series of efforts after its initial introduction [60–63]. Initially, the researchers chose to remain with central filters as they approached the boundaries, while systematically lowering the order. However, Gaitonde & Visbal [63] showed that excellent numerical behavior could be retained by keeping a constant-order filter throughout the domain and resorting to asymmetric stencils near the boundaries. The filters near the boundaries are then dispersive, and have the undesirable property of amplifying some small wavenumber bands (see figure 1 of Gaitonde & Visbal [63], for instance.) Because of this, the filters are only used when deemed absolutely necessary to ensure numerical stability or to suppress excessive noise in the solution. The coefficient list for the 10th-order filter for all of the boundary stencils can be found in tables 2.15–2.19 of Gaitonde & Visbal [61].

4. VERIFICATION*

In order to verify the orthogonal and nonorthogonal sets of equations, two previously published cases with easily reproducible basic states were considered. The first was an incompressible plane Poiseuille flow, which has been analyzed by numerous authors with different numerical techniques [64–66]. The second flowfield was a Mach-10 flat plate, analyzed in detail by Groot et al. [67].

4.1 Poiseuille Flow

The plane Poiseuille flow was investigated at conditions of $Re = 10000$. A diagram of the flow is shown in figure 4.1, and more details about this canonical solution can be found in White [35]. Poiseuille flow is one of very few analytical solutions to the incompressible Navier–Stokes equations, so its solution can be generated with arbitrary precision very easily. BLAST is a compressible stability tool, so analytic profiles for both the density and temperature had to be provided in addition to the parabolic velocity profile. The temperature profile was derived based on the incompressible solution, and the density profile was simply chosen to be constant. The reference properties for Re are the velocity at the center-line, one-half the distance between the two walls, and the kinematic viscosity. Dimensionalizing, the center-line velocity was taken to be 1 m/s, the walls were at $y = \pm 1$ m, and were considered isothermal at 300 K. The kinematic viscosity is $1 \cdot 10^{-4}$ m^2/s, required by the Reynolds number. Dynamic viscosity is determined by Sutherland's formula at the center-line temperature, and density is then computed to match the kinematic viscosity. The pressure gradient used to drive the flow was derived from the conditions on $\bar{u}(y = 0)$. This results in a Mach number of about 0.003, so the effects of using a compressible solver on an incompressible basic state should be minimized.

Previous works reported complex phase-speed results and prescribed $\alpha = 1.0$ [64–66], since the Orr–Sommerfeld equation is naturally a temporal problem. In order to replicate this with

*Portions of this chapter are reprinted with permission from "Linear Stability of a Boundary-Layer Vortex on a Hypersonic Finned Cone" by Andrew Riha, Madeline McMillan, and Helen L. Reed, 2021. *AIAA Aviation 2021 Forum, AIAA Paper 2021-2890*, Copyright 2021 by Andrew Riha, Madeline McMillan, and Helen L. Reed.

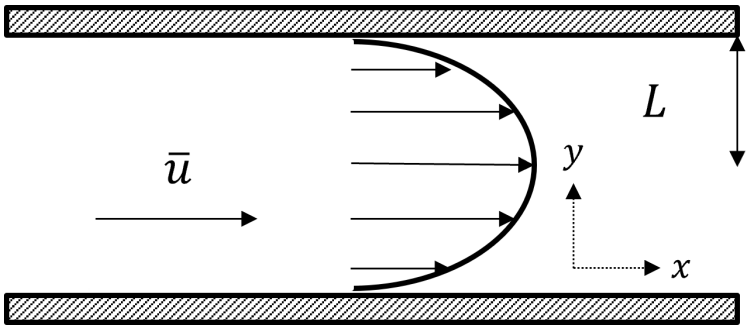

Figure 4.1: Diagram of the plane Poiseuille flow. The flow is fully developed, acting under a constant pressure gradient in the x direction, and infinite in z.

$\bar{u}(y=0)$ [m/s]	$\bar{\nu}$ [m^2/s]	$\bar{T}_{Wall}$ [K]	$\bar{\rho}$ [kg/m^3]	Pr
1	$1 \cdot 10^{-4}$	300.	0.1846	0.72

Table 4.1: Dimensional conditions for the Poiseuille flow.

spatial BiGlobal, the most-accurate phase-speed results were taken from Kirchner [66] ($c_{ph} = 2.375264888204682 \cdot 10^{-1} + 3.739670622979878 \cdot 10^{-3}i$) and were converted to a complex frequency input to BLAST. The correct mode should then have a streamwise wavenumber that approaches $1.0 + 0.0i$. This inversion of the solution procedure does not allow direct comparison of error with the other authors, but this trade-off is accepted since this problem is still one of the most accessible basic-state and stability combinations for verification. The velocity and temperature basic-state profiles was computed at 100001 points, and then a cubic-spline was used to interpolate to the different stability grids. The stability grids were all equally spaced, as there is no boundary layer to capture. Also, odd numbers of points were used so that there would always be a grid point at the center line. 4$^{\text{th}}$-order finite differences are used for the basic-state and stability variables, as well as the metric-tensor components. The boundary conditions for the stability problem consisted of velocity and temperature perturbations being set to zero at the walls, with no boundary condition set on density. In the spanwise dimension of the SBG problem, full Neumann conditions were applied.

The convergence behavior of BLAST can be seen in figure 4.2. The number of points in y range from 201 to 25601, while the number of z points were held constant at 6. The dashed line represents ideal 4^{th}-order convergence, and both the nonorthogonal and orthogonal SBG equations match this rate very well. The error measure used here is shown in equation 4.1, which compares the real and imaginary parts of the eigenvalue against some "true" eigenvalue (indicated with a subscript t). The magnitude of the difference in each component is taken, then normalized by the magnitude of the true eigenvalue. Here, the nonorthogonal and orthogonal solutions with $25601\,y$ points are taken as truth for each method, respectively. Recovering the expected convergence rate puts confidence in the numerics used inside BLAST.

Table 4.2 shows that the α results for each method have a relative error in each method of about $2.1 \cdot 10^{-7}$ when compared to Kirchner's results. This difference is likely due to the fact that BLAST used compressible SBG, whereas Kirchner used the incompressible Orr–Sommerfeld equation. In the SBG results, the density and temperature eigenmodes were around 10 orders of magnitude smaller than the $\hat{u}$ and $\hat{v}$ perturbations, but they were not a perfect zero. Still, this is excellent agreement between three very different numerical methods and verifies BLAST in the incompressible regime.

$$\varepsilon = \frac{|\alpha - \alpha_t|}{|\alpha_t|} \tag{4.1}$$

Codes	α_r	α_i	ε
Kirchner	1	0	0
Orthogonal	0.999999825759	0.0000001238	$2.137 \cdot 10^{-7}$
Nonorthogonal	0.999999825754	0.0000001239	$2.138 \cdot 10^{-7}$

Table 4.2: Eigenvalue comparison with Kirchner [66]. Adapted from Riha et al. [51].

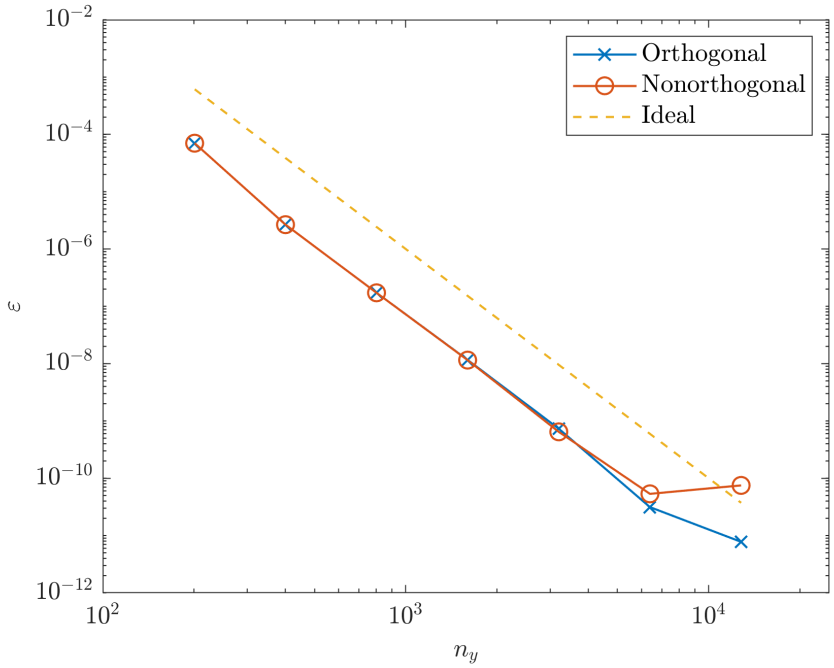

Figure 4.2: Relative error compared to the highest-resolution solution for the Poiseuille flow mode. Adapted from Riha et al. [51].

4.2 Flat-Plate Boundary Layer

4.2.1 Orthogonal Grid

To verify BLAST for high-speed applications, Mach-10 flow over an adiabatic flat plate is considered. These conditions support an unstable second mode, documented in Case 5 of Groot et al. [67]. Here, the base flow was generated in an identical manner and the results from BLAST are compared to LST solutions. DEKAF is used to generate boundary-layer profiles assuming a unit Reynolds number of $Re' = 9.8425 \cdot 10^6$ 1/m and a boundary-layer edge temperature of 278 K. The boundary-layer profiles have a local Reynolds number of 2000. using the Blasius length scale as a reference length, $L = \sqrt{\bar{\mu}x/(\bar{\rho}\bar{u})}$, where x is measured from the leading edge of the flat plate. The flow is modeled assuming a perfect gas with a constant Prandtl number of 0.7, a specific heat $c_p = 1004.5$ J/(kg K), and a ratio of specific heats $\gamma = 1.4$. The basic-state grid uses the algebraic clustering technique described in equations 3.10. The base-flow domain has a

wall-normal height of $y_e = 3.403 \cdot 10^{-2}$ meters and a clustering parameter of $y_c = 7.017 \cdot 10^{-3}$ meters. The 1-D solution is then interpolated on to a dense grid with an extended domain height using the GICM (Groot–Illingworth–Chebyshev–Malik) interpolation method described in Groot et al. [67], and repeated in the spanwise direction to give a 2-D base flow. BLAST may then spline interpolate the basic state onto different stability grids.

M	Re_L	Re' [1/m]	$\bar{T}_\infty$ [K]	Pr	c_p [J/(kg K)]
10.	2000.	$9.8425 \cdot 10^6$	278.	0.7	1004.5

Table 4.3: Conditions for the flat-plate case.

The orthogonal and nonorthogonal formulations of BLAST are compared against LST results published in the literature, which were regenerated using an in-house code developed by Koen Groot [67]. All stability results using this verification cases consider the stability of a second mode with a nondimensional angular frequency of $\omega = 0.075$ ($f = 196.329$ kHz). The orthogonal formulation of BLAST is used to generate an orthogonal grid which is clustered using the same Malik-mapping parameters as in DEKAF. This grid is used with the nonorthogonal method as well. 4$^{\text{th}}$-order finite differences are again used in BLAST. To match the parallel assumption in LST, the BiGlobal codes impose $\bar{v} = 0$ for the basic state. The stability problem is first solved using the Arnoldi algorithm with 100 Arnoldi iterations. Then the 2-D second mode is identified and converged using the Newton–Raphson algorithm until the L_2 norm of the residuals to the equations is less than 10^{-14}. For the stability boundary conditions, no-slip and isothermal conditions are enforced at the wall, and $\hat{\phi} = 0$ is imposed at the freestream boundary on all perturbation variables.

Both the orthogonal and nonorthogonal versions of BLAST are run with increasing points in the wall-normal direction until convergence is demonstrated. 6 points are used in z. Figure 4.3 shows the convergence of both BLAST formulations and LST using both spectral and finite-difference methods, with all errors reported relative to their own methods. The LST code using Chebyshev

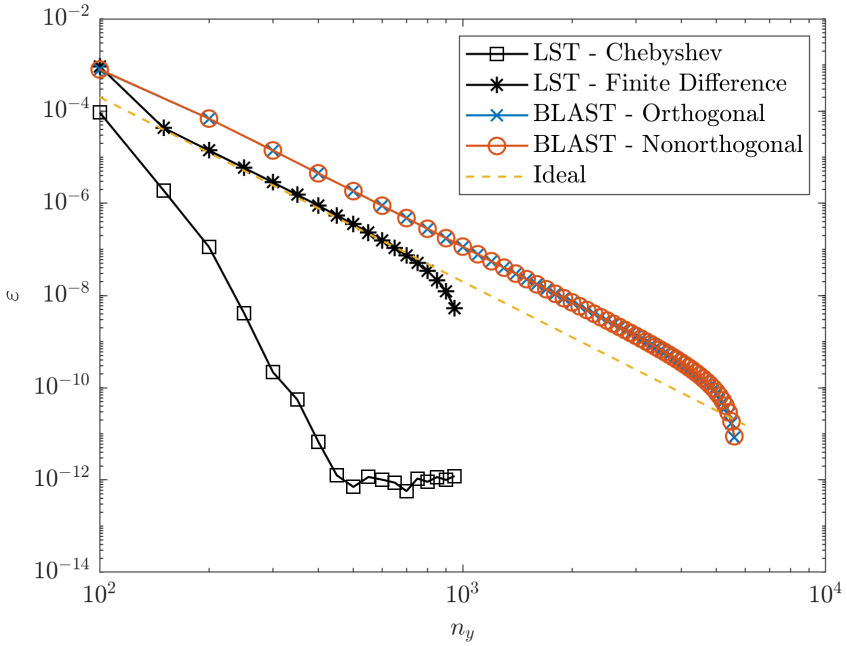

Figure 4.3: Convergence error for Mach-10 2-D second mode. Adapted from Riha et al. [51].

polynomials converges rapidly due to the fast convergence properties of spectral methods. Both BLAST formulations and the LST code using finite differences converge at the expected rate for a 4$^{\text{th}}$-order code and require far more points in the wall-normal direction to reach the same level of convergence as the Chebyshev code. The final eigenvalues are compared against each other in table 4.4. Both formulations of BLAST match the LST results to at least six digits, giving relative errors of approximately $5.9 \cdot 10^{-8}$ when compared against the LST code using Chebyshev polynomials.

Code	α_r [1/m]	α_i [1/m]
LST - Chebyshev	$3.86915377501814 \cdot 10^2$	-7.98862348206074
LST - Finite Differences	$3.86915370085317 \cdot 10^2$	-7.98862874509943
BLAST - Orthogonal	$3.86915354920636 \cdot 10^2$	-7.98862655553127
BLAST - Nonorthogonal	$3.86915354891287 \cdot 10^2$	-7.98862653486782

Table 4.4: Mach-10 most-converged eigenvalue comparison. The full double-precision numbers are reported for verification purposes. Adapted from Riha et al. [51].

Further comparison was sought for the eigenmodes themselves. The eigenfunctions from the LST solver using Chebyshev polynomials with 500 points are compared against the eigenmodes from both formulations of BLAST using 5000 wall-normal points in figure 4.4. The mode shape is excellently replicated between all three solvers.

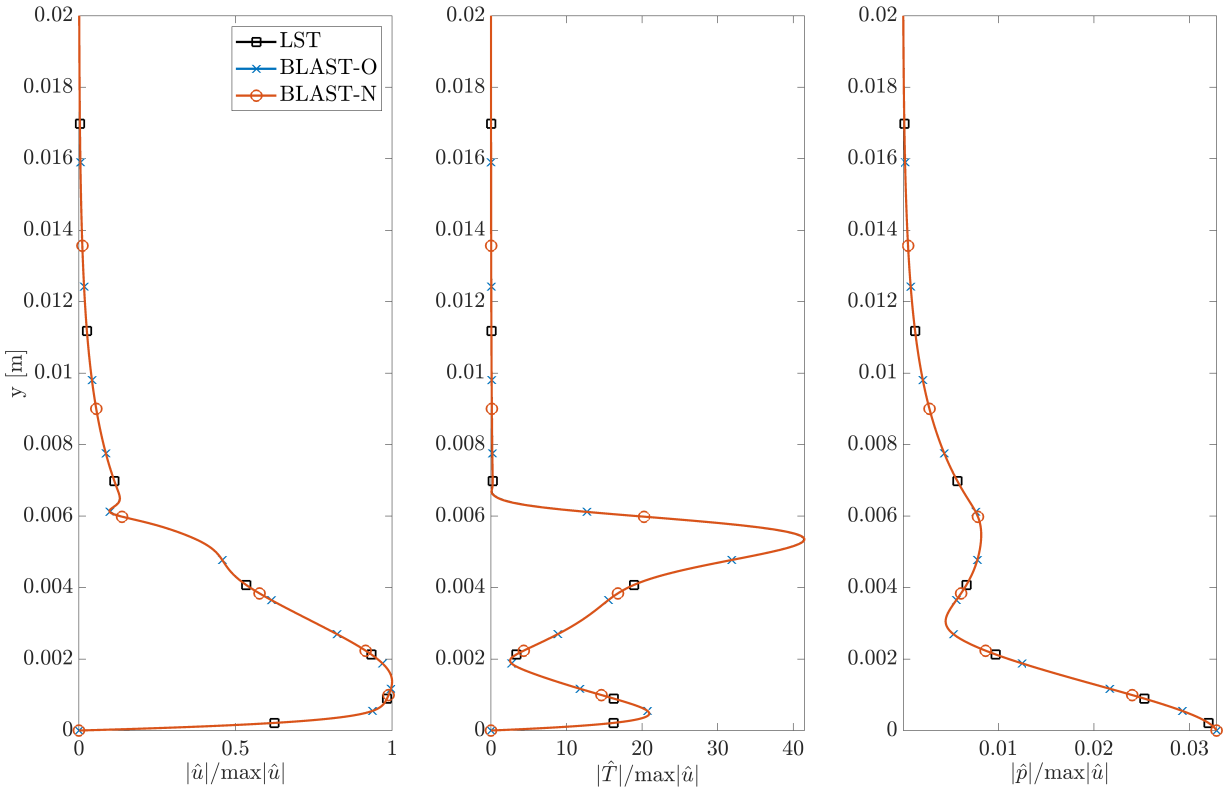

Figure 4.4: Eigenmode comparison between different solvers for Mach-10 2-D second mode. Adapted from Riha et al. [51].

4.2.2 Nonorthogonal Grid

The above results verify the orthogonal equations, as well as the nonorthogonal equations on an orthogonal grid. All that is left is to test the nonorthogonal equations on a nonorthogonal grid.

Nonorthogonality in a grid is known to have detrimental effects to the accuracy of a numerical

solution, even though it is an invaluable tool for analysis of complicated shapes [68, 69]. Skew between grid lines and alignment of the grid lines with gradients in the solution are the primary contributors to additional error. For verification purposes, it is important to be able to distinguish between the two effects. An analytical transformation is used to distort the grids, so that control is retained over the form and level of distortion. The equations used for the nonorthogonal grid are shown below. Y and Z are the Cartesian coordinates, and they range from 0 to Y_{Max} and Z_{Max}, respectively. Y_{Orth} is the clustered distribution used in the orthogonal grid with the same mapping parameters. Y_Δ and Z_Δ are the distortion parameters that affect how skewed the grid is. When $Y_\Delta = Z_\Delta = 0$, the grid is the same as the orthogonal grid. The distortion is in the form of a two-dimensional parabola in the N frame, so that the effect is maximized in the center and decays to zero at the boundaries. Importantly, the boundaries are perfect lines and meet each other at 90 degree angles. The reason for this is simple: when Neumann conditions are applied on the boundaries, the direction of the normal vector of the boundary has to stay parallel with the wall. The normal vector must align with the 2-D direction of the boundary layer due to the symmetry of the problem. However, the interior points can approach the boundary at nonorthogonal angles.

$$Y(\eta,\zeta) = Y_{Orth} + Y_{Max} Y_\Delta \left(1-(2\eta-1)^2\right)\left(1-(2\zeta-1)^2\right) \tag{4.2}$$

$$Z(\eta,\zeta) = Z_{Max}\left[\zeta + Z_\Delta \left(1-(2\eta-1)^2\right)\left(1-(2\zeta-1)^2\right)\right] \tag{4.3}$$

Two examples of what grids equations 4.2 and 4.3 can be found in figures 4.5 and 4.6. Both have only 21 points in each dimension so that the structure of the grid can be seen. Z_{Max} is 0.001 meters, roughly an order of magnitude smaller than the boundary-layer height. Figure 4.5 has distortion parameters of $Y_\Delta = Z_\Delta = 0.1$, distorting the grid in both dimensions. The intersection angles get more skewed towards the wall due to the clustering present in Y_{Orth}. The effect of turning off the distortion in Y is shown by figure 4.6.

Initially, grids with $Y_\Delta = Z_\Delta = 0.1$ were tested. However, curving the constant-η lines resulted

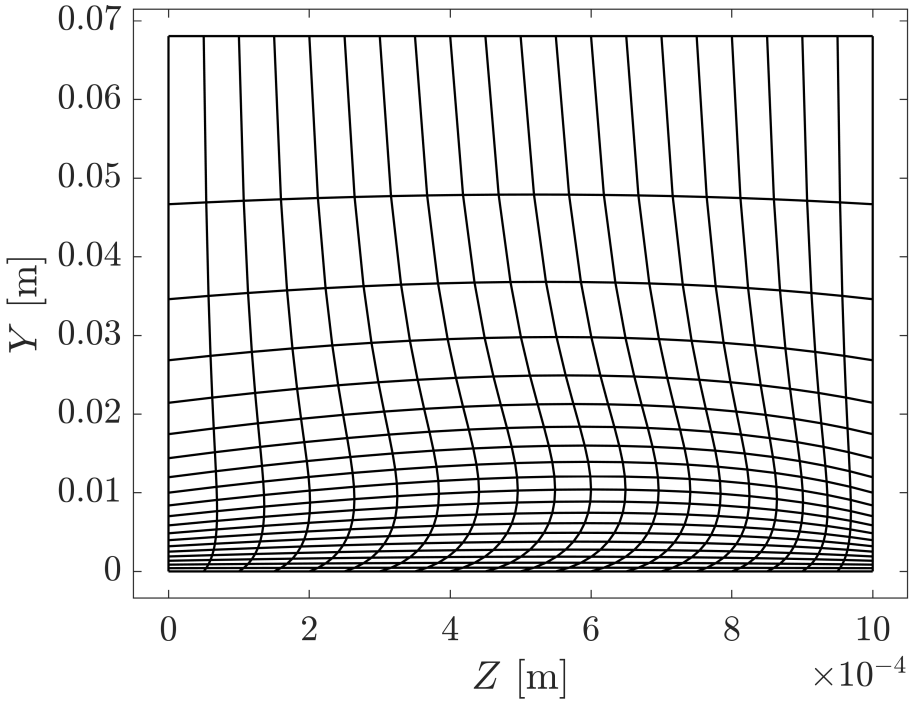

Figure 4.5: Example of the nonorthogonal grid with $n_y = n_z = 21$, $Y_\Delta = Z_\Delta = 0.1$.

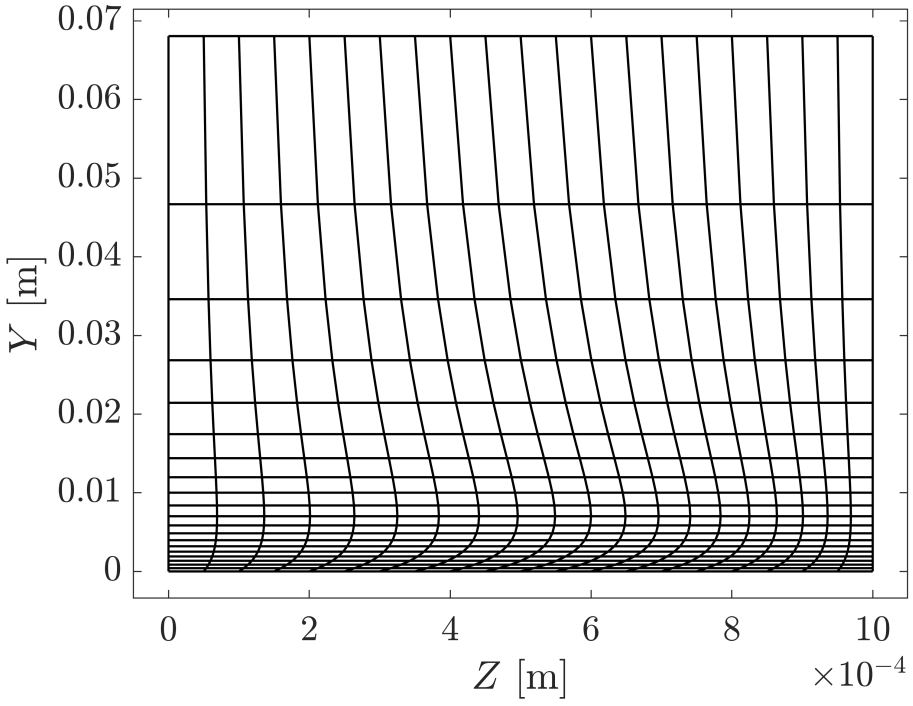

Figure 4.6: Example of the nonorthogonal grid with $n_y = n_z = 21$, $Y_\Delta = 0$, $Z_\Delta = 0.1$.

in the $\partial/\partial\zeta$ derivatives to be orders of magnitude higher. These grids required excessive amounts of points in ζ to resolve the solution, and were less useful as verification tools. As a result, grids with $Y_\Delta = 0$ and $Z_\Delta = 0.1$ were chosen instead for this task.

Figure 4.7 shows the relative error of the nonorthogonal SBG result to the most-accurate Chebyshev LST solution, as a function of n_y and n_z. Symmetry conditions (described in section 3.3.2.1) were used on the constant-ζ boundaries, and the same boundary conditions as in the orthogonal case were used at the wall and freestream. Figure 4.7 shows that $n_z = 6$ is no longer sufficient to reproduce the LST solution. The accuracy of the solution increases with n_z until $n_z = 101$, then the error begins to rise again. Similarly, there is a n_y for each n_z where error is minimized, and it is usually not the largest n_y. This behavior can also be seen in figure 4.8, which shows the magnitude of the $\hat{w}_C$ function in the Cartesian frame. Since $Y \neq Y(\zeta)$, $\hat{w}$ (in both the Cartesian and nonorthogonal frames) is in the 2-D direction and should be zero. However, when weighted against the largest value in the eigenfunction, it is seen to be heavily dependent on the value of n_z. The behavior of ε with respect to n_z in figure 4.7 correlates very well with the size of the error in $\hat{w}$ in figure 4.8. This would suggest that attempting to resolve a function that should be zero with a nonorthogonal grid is a difficult ask of these numerical methods. The solution eventually diverges as n_y and n_z increase. However, at best combination shown here of $n_y = 3201$ and $n_z = 101$, the error is $\varepsilon = 2.7 \cdot 10^{-9}$. This is about the same level of accuracy as the results using the orthogonal grids. With these cases, BLAST has been verified for incompressible and hypersonic results, using both orthogonal and nonorthogonal methods and grids.

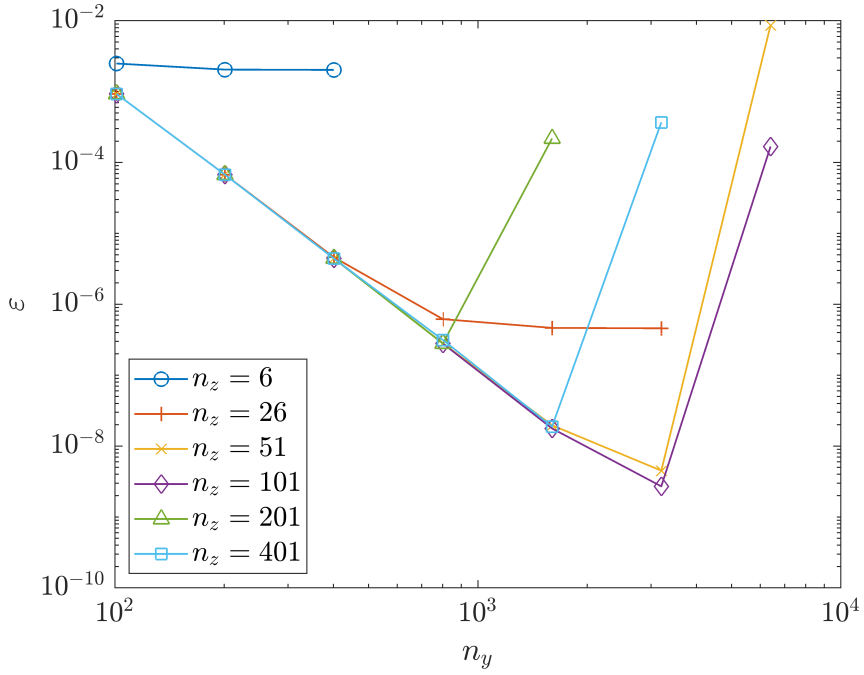

Figure 4.7: Relative error of the nonorthogonal SBG solutions compared to the most-accurate LST result.

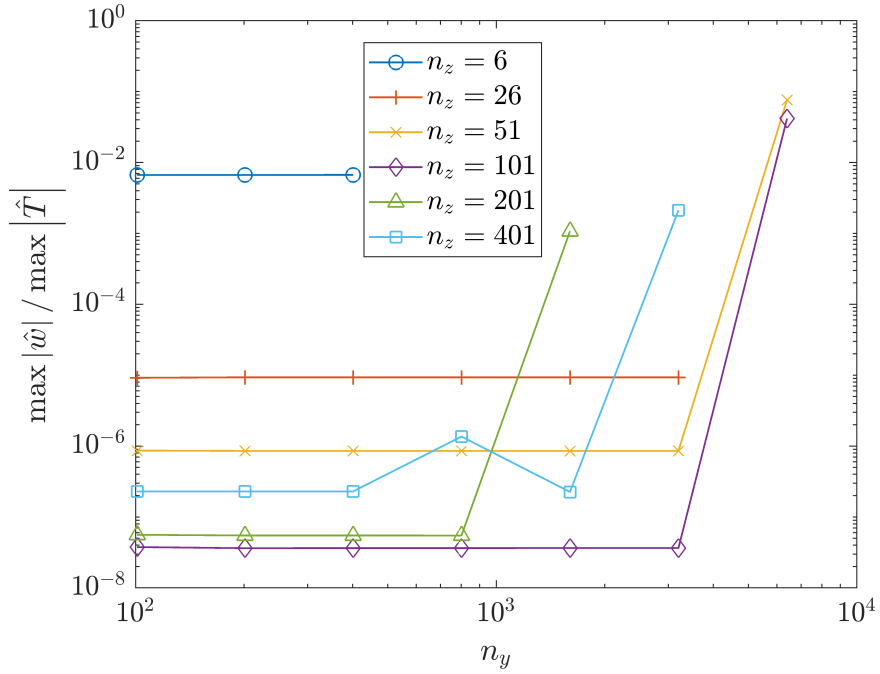

Figure 4.8: Magnitude of the $\hat{w}$ function in the nonorthogonal frame relative to the largest component of the eigenfunction.

5. FINNED CONE: CASE I*

5.1 Introduction

Attention will now to turn to the application of SBG to a cone with a highly swept fin. A series of experiments were performed at Purdue University's Boeing/AFOSR Mach-6 Quiet Tunnel (BAM6QT) [5, 70–73]. The BAM6QT features low freestream-turbulence levels and delayed boundary-layer transition on the tunnel walls, allowing for a testing environment that has noise levels closer to those seen in flight [74].

Parametric studies were performed in the BAM6QT by changing geometric properties of the fin, nose-tip, and the Reynolds number. These experiments were also analyzed by multiple computational groups for its basic-state and stability characteristics [71, 75, 76]. The particular configuration used here is detailed in table 5.1 and visualized in figure 5.1. This cone was chosen because there are good experimental measurements for this case that can support boundary-layer-stability calculations. In particular, a horseshoe vortex that emanates from the fin-cone juncture and wraps around the cone is observed to transition before any other section of the flow [70]. This horseshoe vortex can be visualized by looking at the surface heat flux on the model, as in figure 5.2. This feature provides an excellent test bed for different ways to measure, extract, and analyze instabilities present in SBG solutions. Experiments run at $Re' = 6.0 \times 10^6$ m^{-1} are seen to be mostly laminar with some instabilities detected through pressure fluctuations. At an Re' between 6.7–7.0×10^6 m^{-1}, the flow appears to be transitional at the back of the cone [70]. With this information, two primary conditions were chosen to study the linear stability of this problem, shown in table 5.2. These flowfields should contain well-amplified instabilities, without turbulence or late stages of transition affecting the accuracy of the basic state.

*Portions of this chapter are reprinted with permission from "Linear Stability of a Boundary-Layer Vortex on a Hypersonic Finned Cone" by Andrew Riha, Madeline McMillan, and Helen L. Reed, 2021. *AIAA Aviation 2021 Forum, AIAA Paper 2021-2890*, Copyright 2021 by Andrew Riha, Madeline McMillan, and Helen L. Reed.

Parameter	Measurement
Cone Length [m]	0.4
Cone Half Angle [deg]	7
Nose Radius [μm]	50
Fin Leading-Edge Sweep [deg]	75
Fin Leading-Edge Radius [mm]	3.175

Table 5.1: Geometric description of the finned cone.

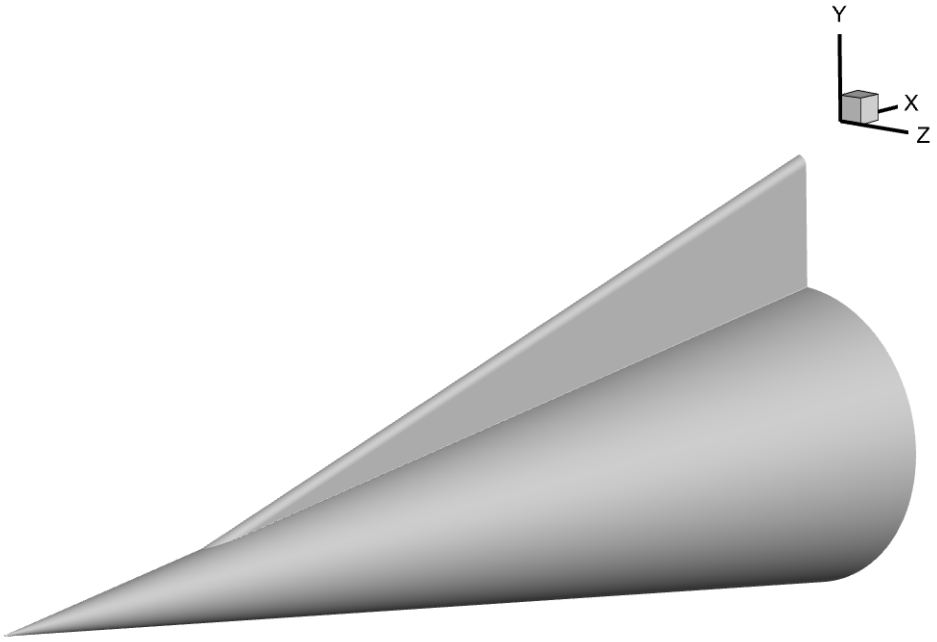

Figure 5.1: Finned cone model, with 75° sweep.

Cases	M	Re' [1/m]	ρ_∞ [kg/m^3]	T_∞ [K]	T_{Wall} [K]
I	6	$6.3 \cdot 10^6$	0.0240	50.61	300.
II	6	$5.9 \cdot 10^6$	0.0229	51.92	300.

Table 5.2: Flow conditions for the finned cone.

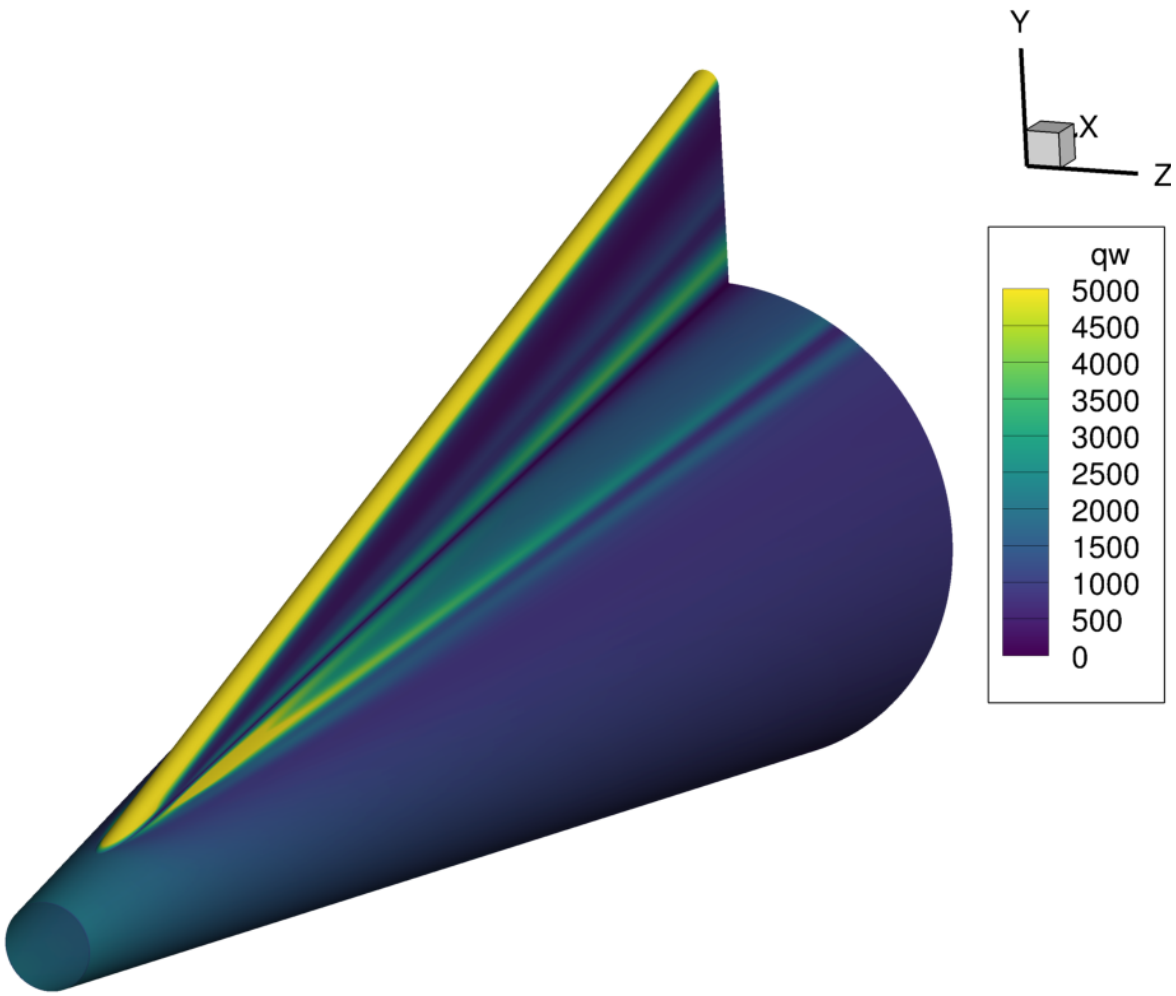

Figure 5.2: Computational heat flux contours on the finned cone. The horseshoe vortex can be seen as the hot-cold-hot streak at the back of the cone.

5.2 Basic State

The flowfield around the fin cone is a challenging one. There is a shock caused by the fin that slowly merges with the oblique shock from the cone as it travels downstream. A vortex forms on the fin that tends to break into additional vortices with enough length or Reynolds number. However, the focus for application of SBG will be on the horseshoe vortex on the surface of the cone.

The horseshoe vortex is initialized by the intersection of the fin and the cone. Most flows of this kind feature a separated boundary layer upstream of the leading edge. This causes a series of vortices to occur in a complicated system of shocks and reattached flow that depends greatly on the sweep, boundary-layer height, leading-edge radius, and Mach number [77]. However, experiments have found that sweep can eliminate separation of the boundary layer altogether [78]. For the geometry described by table 5.1 at Mach 6 and $Re' = 6.3 \times 10^6$ m^{-1}, there is also no boundary-layer separation.

The Data-Parallel Line Relaxation (DPLR) code is used to simulate the flow around the finned cone [79]. This is a finite-volume, structured, viscous, CFD solver that has been verified and validated on hypersonic problems [80]. It uses modified Steger–Warming inviscid fluxes [81] with 3$^{\text{rd}}$-order MUSCL (Monotonic Upstream Schemes for Conservation Laws) extrapolation and the min-mod limiter [82]; a 2$^{\text{nd}}$-order central stencil for the viscous fluxes is used as well.

Prior to running the simulation, a mesh is created over the finned cone using structured hexahedral grids using the Pointwise software. Overall grid topology, along with the symmetry plane and outflow plane, are shown in figure 5.3a. Mullen et al. [71] found that the effects of the fin are felt beyond 90° azimuthally by examining the dominant second-mode frequencies on a half-symmetry solution. As a result, the geometry is simulated using half-symmetry instead of quarter-symmetry. Hexahedral cells are fit to the circular nose using two three-point grid singularities in an H-grid. Other than the nose, the use of singularities is avoided when constructing these grids. The intersection of the fin with the cone is shown in figure 5.3b. The grid was blended as smoothly as possible while still representing the elliptic intersection. Cell clustering was strictly enforced near the sur-

face of the cone, with a first-cell wall-normal spacing of 1 μm or less to capture the boundary layer.

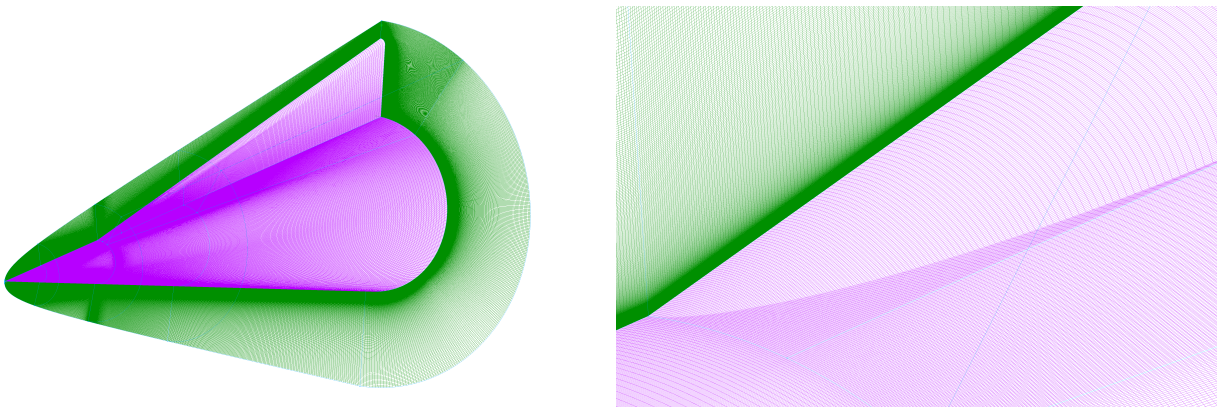

(a) Overview (b) Fin-Cone Intersection

Figure 5.3: Basic-state grid topology. Reprinted with permission from Riha et al. [51].

A converged basic state is needed prior to beginning the stability analysis. It is well known that stability results are highly sensitive to slight changes within the basic state; therefore a grid-convergence study is necessary to ensure convergence of the stability results [83]. Three different basic states were simulated using different grid densities, shown in table 5.3. These counts refer to the combined block downstream of the nose; adjoining boundaries of the H-grid determined the number of cells resolving the nose-tip region. Total cell counts number roughly 100, 150, and 300 million. The vortex on the cone was examined for grid convergence by comparing $\bar{u}_C$ contours at different axial slices. This is shown in figure 5.4. There is close agreement among all three solutions. At the first two axial stations shown, there is almost no visible difference. Slight differences can be seen at the very center of the vortex in the last two axial slices, suggesting that another solution should possibly be pursued with more grid points in this region. However, the difference between the 100- and 150-million-cell solution appears to be more than the difference between the 150- and 300-million-cell boundary layer. This indicates that the solution is likely in the asymptotically-converging domain with respect to the grid size and the numerics used. While

it does not definitively prove that the basic-state is converged, a stability analysis was undertaken using the 300-million-cell grid as useful information can be gleaned from it. The grid convergence of the basic state will be revisited in section 6.1.1.

Resolution	Streamwise	Wall-Normal	Azimuthal	Total (millions)
Low	525	450	450	106
Medium	775	450	450	156
High	977	567	567	314

Table 5.3: Grid sizes for the convergence study for Case I. These node counts refer to the region beyond the nose. Adapted from Riha et al. [51].

The cone vortex originates from where the leading edge of the fin meets the cone. Near this intersection, the flow is undeniably three dimensional and spatial BiGlobal would not be a useful tool. In order to determine the extent of this region of strongly 3-D flow, the vortex was mapped out as can be seen in figure 5.5. The left and right wall-normal dips in streamwise velocity around the vortex were used to mark its bounds, and then a 6^{th}-order polynomial was fit to the locations. Upstream of $X = 0.2$ meters, the bounds show that the vortex is still turning fairly quickly. Based on this data, it was determined that SBG would be bounded between $X = 0.2$ and 0.38 meters. (A buffer region between the last stability surface and the basic-state outflow plane was kept in order to avoid any unphysical influences from the exit boundary condition.)

5.3 Stability Results

The nonorthogonal capabilities of BLAST are employed here. This ensures that stability effects of complicated boundaries like the intersection of the fin and cone are accurately modeled. For the SBG grid, the topology selected is shown in figure 5.6. The grid wraps around the geometry from the fin leading edge to the opposite symmetry plane. The stability surface is wall-normal to the cone, extends up the fin at a constant angle, and is locally warped near the fin leading edge to

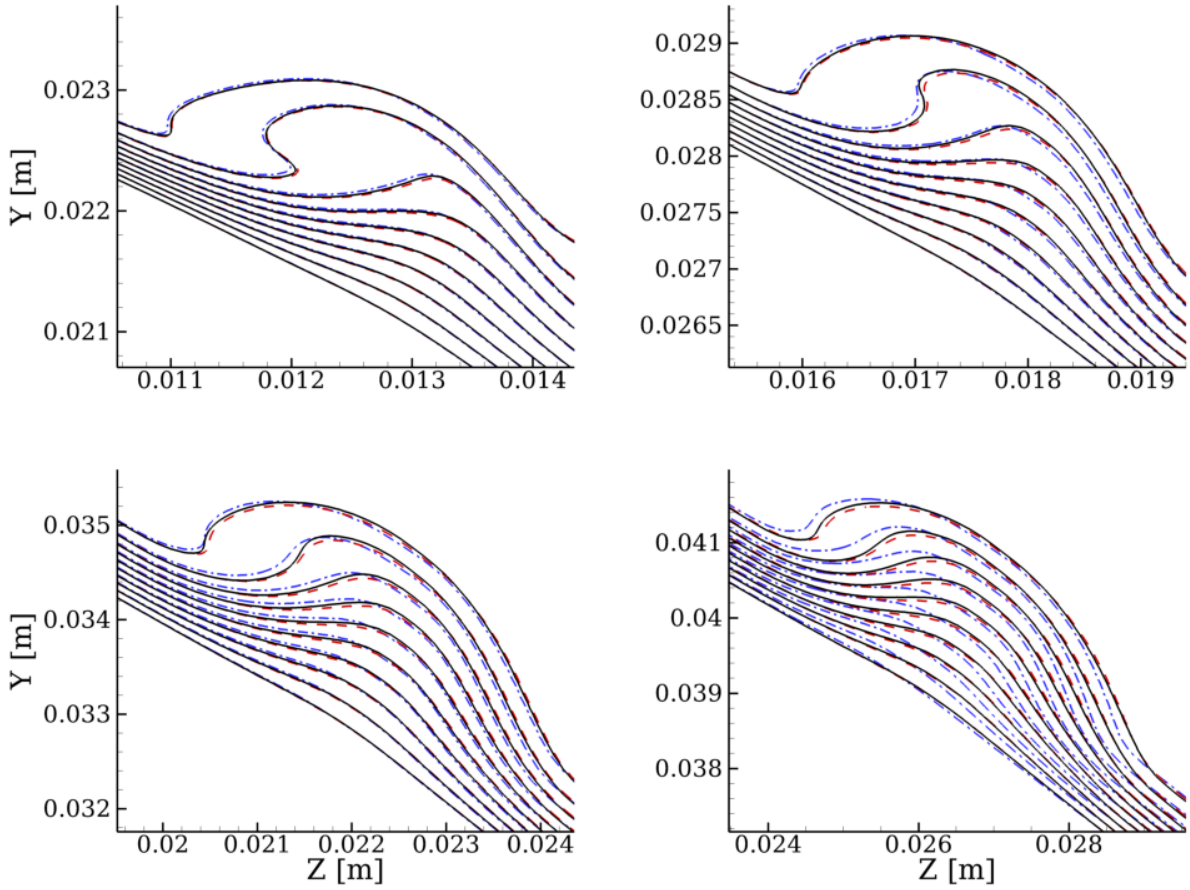

Figure 5.4: Comparison of cone vortex shown with $\bar{u}$ velocity contours between 100-million (blue lines), 150-million (red lines), and 300-million (black lines) solutions. Data is shown at different X locations: top-left) 0.20 m, top-right) 0.26 m, bottom-left) 0.32 m, bottom-right) 0.38 m. Reprinted with permission from Riha et al. [51].

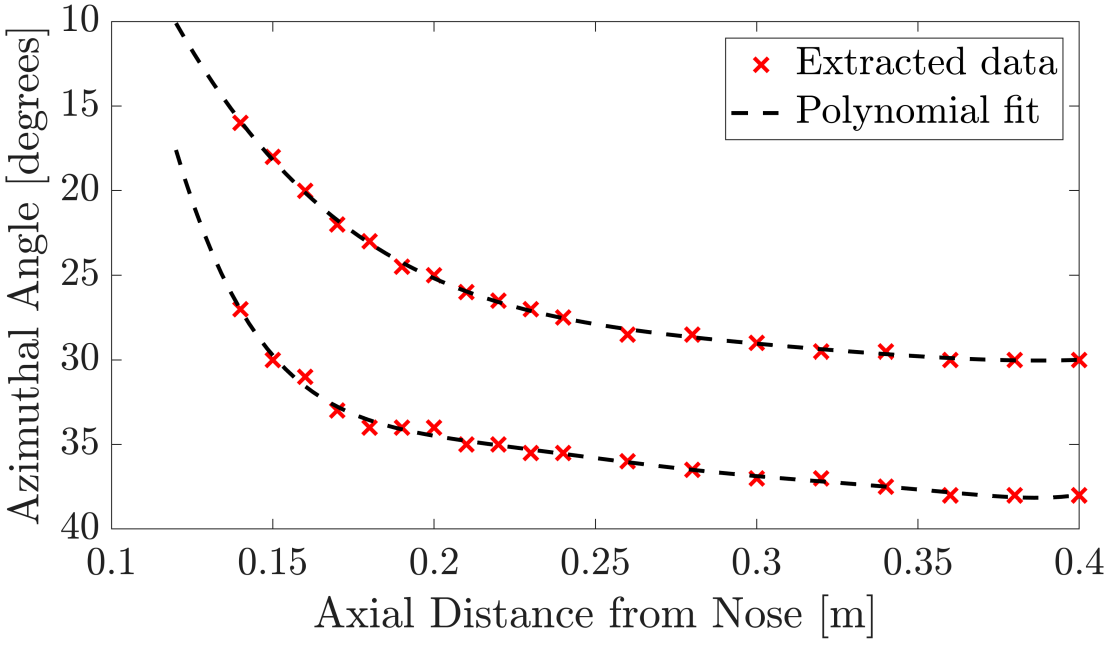

Figure 5.5: Left and right bounds on the cone vortex. Reprinted with permission from Riha et al. [51].

be wall normal there as well. The cone wall and fin wall are treated as one continuous boundary, which leads to some skewed cells near the fin. This idea can be seen in the close up of this region in figure 5.7. The skewed cells were minimized as much as possible with smoothing, but maintaining wall-normal and rectangular grid cells near the cone vortex were the main priority. Grid counts consisted of 400 wall-normal and 500 azimuthal points. Based on a limited grid-convergence study on the 150 kHz mode at 0.380 meters, a stability grid with these dimensions was determined to be within roughly 1% of a higher-resolution solution. Wall-normal points were heavily clustered towards the wall. 291 of the 500 azimuthal points were placed in the vortex region, with the rest ensuring adequate spatial resolution to the boundary conditions. Computational cost was also a factor, with each solution requiring 45 gigabytes of computer memory for its LU decomposition. With SBG solutions desired at multiple frequencies and axial stations (totalling more than 2400 solutions), this 400 by 500 grid was determined to be a good trade-off between accuracy and computational resources. Upstream grids were generated programmatically with Pointwise, with

care taken to ensure adequate smoothness and that the spanwise clustering tracked the vortex.

A useful coordinate system for the finned cone is as follows. The R frame, mention in Chapter 3, has basis vectors $\{\boldsymbol{b}_\chi, \boldsymbol{b}_r, \boldsymbol{b}_\Theta\}$. $\boldsymbol{b}_\chi$ is unit and is parallel with $\hat{\boldsymbol{\imath}}$. $\boldsymbol{b}_r$ is also unit and colinear with $\hat{\boldsymbol{\jmath}}$. Finally, $\boldsymbol{b}_\Theta$ is the final component of the right-handed system, although this vector is not unit. The origin is the virtual sharp edge of the cone, same as the Cartesian frame.

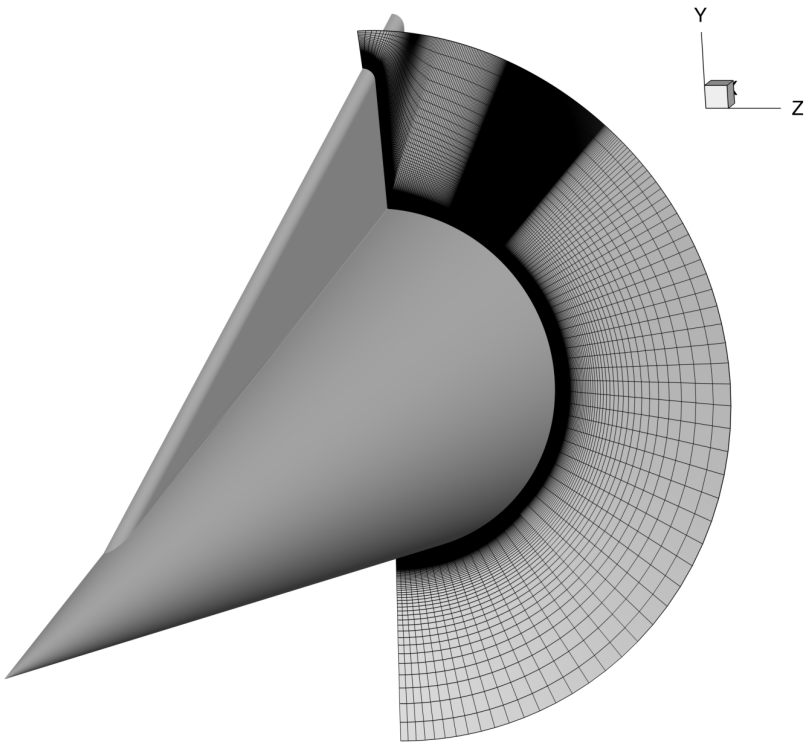

Figure 5.6: The stability grid used at $X = 0.380$ m from the nose. Reprinted with permission from Riha et al. [51].

The boundary conditions used with this grid topology are shown in table 5.4 and defined by equations 3.21, 3.22, and 3.28. The wall conditions are typical no-slip conditions, with density allowed to remain free. (In the linearized Navier–Stokes equations, there are only 1st-order spatial derivatives on density, so only one boundary condition may be applied.) The freestream boundary is outside the shock, so it was found that setting the perturbations to 0 resulted in less extraneous

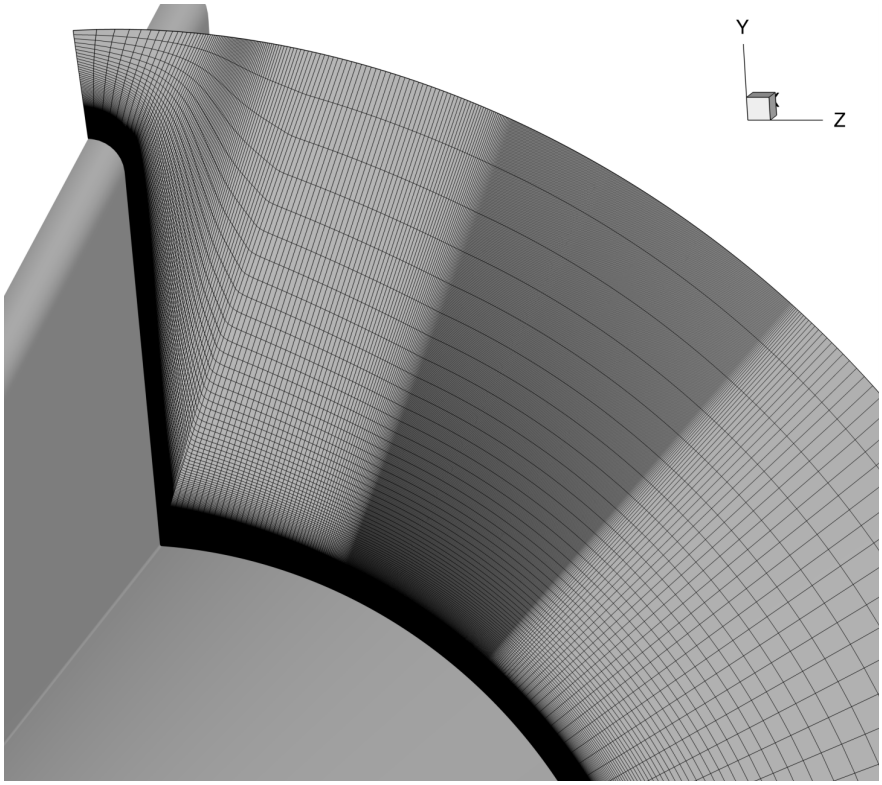

Figure 5.7: A closer view of the fin-cone intersection region on the stability grid used at $X = 0.380$ m from the nose. Reprinted with permission from Riha et al. [51].

modes near the shock in the spectrum than Neumann conditions. Additionally, this minimized the chance of any shock-induced oscillations affecting what would otherwise be physical modes. (No special handling of the shock was implemented with regards to the finite-difference scheme, as it was not seen to affect any eigenmodes in the boundary layer.) The $\Theta = 0$ and $\Theta = 180$ degrees boundaries are given symmetric boundary conditions on the perturbations. Asymmetric boundary conditions [31] are not necessary when the distance of the boundaries from the vortex is considered. Notably, many modes that exist in the cone vortex do not need the full extent of this domain. Indeed, further tests after modes were identified showed that the domain could be reduced in particular cases. However, to avoid testing a solution's dependence on artificially reduced boundary locations for each type of instability at various axial stations, the full domain was used across the entire X range of the cone. 4^{th}-order-accurate finite differences were used to approximate the derivatives, as described in section 3.5.1. $\boldsymbol{a}_\xi$ is chosen to be the normal of the stability surface, and ξ derivatives of the metric tensor are defined to be zero.

Boundary	$\hat{u}_N$	$\hat{v}_N$	$\hat{w}_N$	$\hat{T}$	$\hat{\rho}$
Wall	D	D	D	D	None
Freestream	D	D	D	D	D
$\Theta = 0°$	S	S	S	N	N
$\Theta = 180°$	S	S	S	N	N

Table 5.4: Stability boundary conditions used. D corresponds to a Dirichlet condition as defined by equation 3.21, N corresponds to a Neumann condition as defined by equations 3.22, and S corresponds to the symmetry conditions defined by equations 3.28. Adapted from Riha et al. [51].

SBG was first initiated near the back of the cone, at $X = 0.380$ meters from the nose. (All distances are measured from the nose to the location on the cone surface that intersects the stability grid.) Frequencies from 25 kHz to 400 kHz were searched, with phase speeds ranging from 0.1 to 0.9 when nondimensionalized by the freestream velocity. The most-unstable modes found in this

region are shown in figure 5.8. Nothing was found to be unstable beyond 250 kHz. The phase speeds for these modes all hover very tightly around 0.9, and no physical modes were found at this location with a phase speed of less than 0.7.

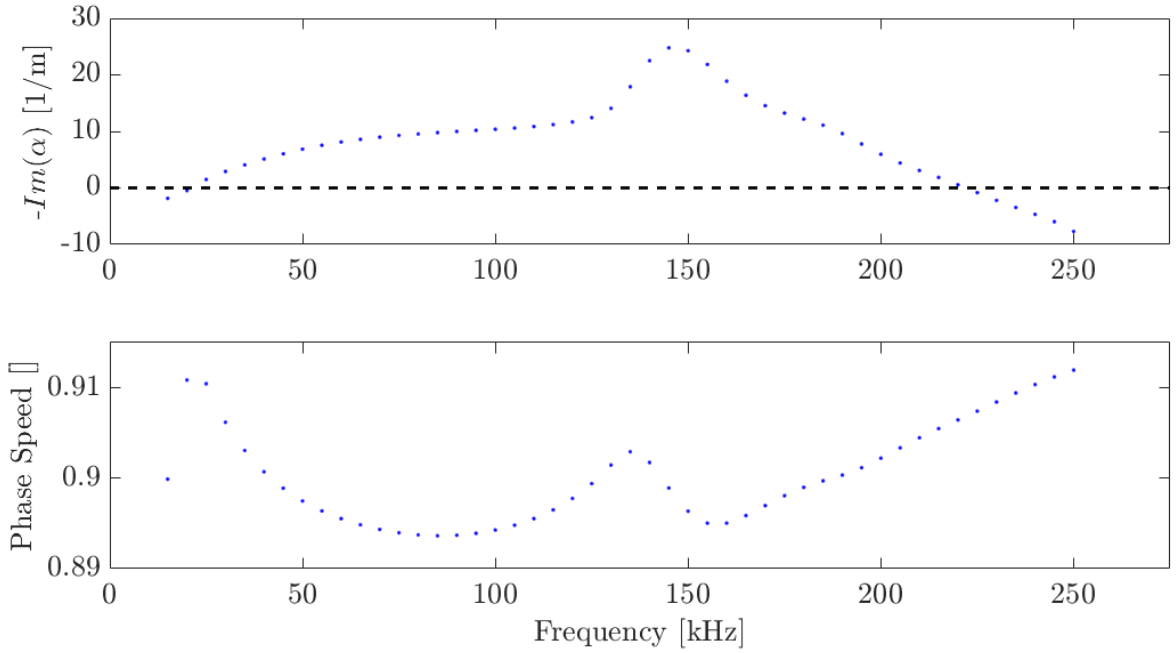

Figure 5.8: Most-unstable modes at $X = 0.380$ meters from the nose. Reprinted with permission from Riha et al. [51].

All of the modes shown in figure 5.8 were marched upstream from 0.380 to 0.200 m. The Newton–Raphson technique mentioned in section 3.4.2 was used to converge the next X location starting from the previous solution as a guess. When the convergence routine worked well, it saved a significant amount of time, as an eigenvalue problem for each frequency and position would have been needed, along with manual selection of the corresponding mode. Since the convergence method uses both the eigenvalue and eigenvector from the previous solution, it is likely to track the same instability without any intervention. However, some frequencies proved to need smaller X steps than others, ranging from 2 to 10 mm, so the task was not completely without manual input.

Figure 5.9 shows the growth rate as a function of X, with each line representing a particular

frequency. Lower frequencies are represented by darker colors, and higher frequencies by lighter colors. The instabilities from 15–155 kHz all reach a neutral point, while the 160–250 kHz modes continue to be unstable further upstream. There are two locations in the position-frequency phase space where the smoothness of the growth-rate trend is broken. The first is at $X = 0.256$ m, with 205 and 210 kHz being the bounding frequencies. The second occurs between 155 and 160 kHz at $X = 0.278$ m. These sudden changes suggest that there are likely multiple unstable modes present at the same frequency, and more work is necessary to map out these instabilities in those regions. Interestingly, in both cases, α_i turns smoothly on either side of the frequency break. These results indicate one of two possibilities. On one hand, it is possible that the behavior of the mode changes rapidly at a critical frequency. This is already seen in the behavior of α at $X = 0.380$. At $f = 125$ kHz, $\partial\alpha_i/\partial f$ changes significantly, and further investigation of the mode shape indicates that the same mode is retained. However, it is also possible that the convergence routine jumped to a new mode with a similar α at the same frequency. A deep dive of this possibility is left for Chapter 6.

When calculating the N factor, the situation is different than what led to the N factor definition of equation 2.23. Here, each solution locally assumes that α is constant, yet it is different at each ξ location. This can be addressed by treating the flowfield as a series of strips with constant alpha, and then numerically integrating them. In other words, define $N = \int_{\xi_0}^{\xi_1} -\alpha_i d\xi$. This allows a formally parallel theory to be more applicable to nonparallel boundary layers. Note that this definition does not include the spanwise growth from 2.23, and effectively assumes that $\boldsymbol{a}_\xi$ is in the group-velocity direction.

The N factors of the aforementioned frequencies are shown in figure 5.10. The three divisions of frequencies noted with regard to figure 5.9 are again visible when considering integrated growth. The most-amplified frequency is 180 kHz, reaching an N of about 4.5. However, it should be noted again that the neutral point was not reached for multiple frequencies, including the one most-amplified over this distance. Based of the trends of $-\alpha_i$ vs X present in figure 5.9, any of the instabilities in the 160–205 kHz frequency band could have the highest N factor when the stability analysis is extended further upstream.

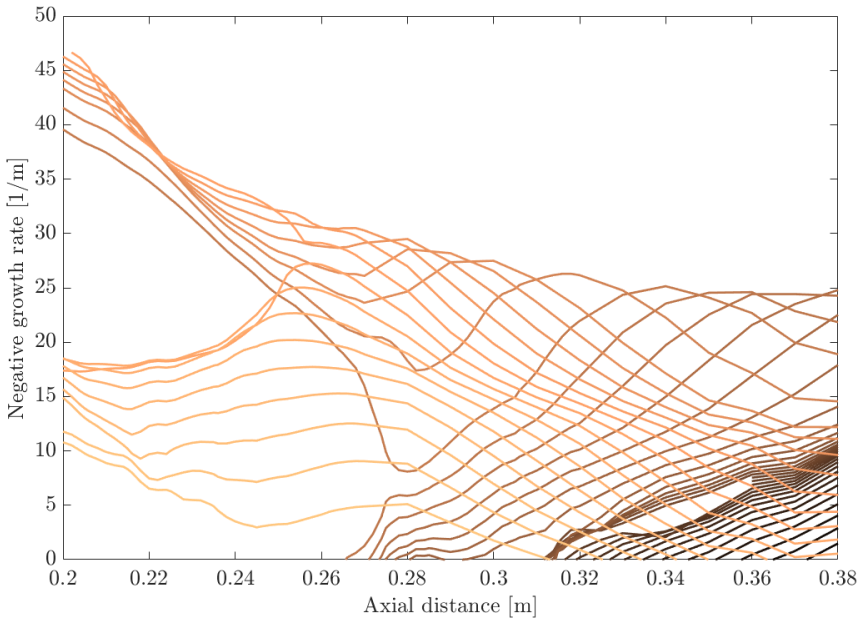

Figure 5.9: Growth rate as a function of position. Each line represents a separate frequency, ranging from 15 kHz (the darkest line) to 250 kHz (the lightest line) in 5 kHz steps. Reprinted with permission from Riha et al. [51].

Figure 5.11 shows the development of $|\check{\hat{u}}_N|$ along the cone for the most-amplified frequency, 180 kHz. (Note that this is referring to the magnitude of the complex, physical component of $\hat{u}_N$, not the magnitude of the total perturbation velocity vector.) At $X = 0.200$ m, the main concentration of the eigenfunction is on the shoulder of the vortex, with an extension reaching over the top. By $X = 0.260$ m, the strength of the region extending over the top has significantly diminished. As the instability convects further downstream, the main lobe of $|\check{\hat{u}}_N|$ slowly rides higher and higher on the shoulder, nearing the top. A weaker concentration exists near the wall at all locations, but is significantly affected by the basic-state distortion and it is difficult to discern a pattern. The wall-normal and azimuthal components of the velocity perturbation have very complicated signatures and are not shown here.

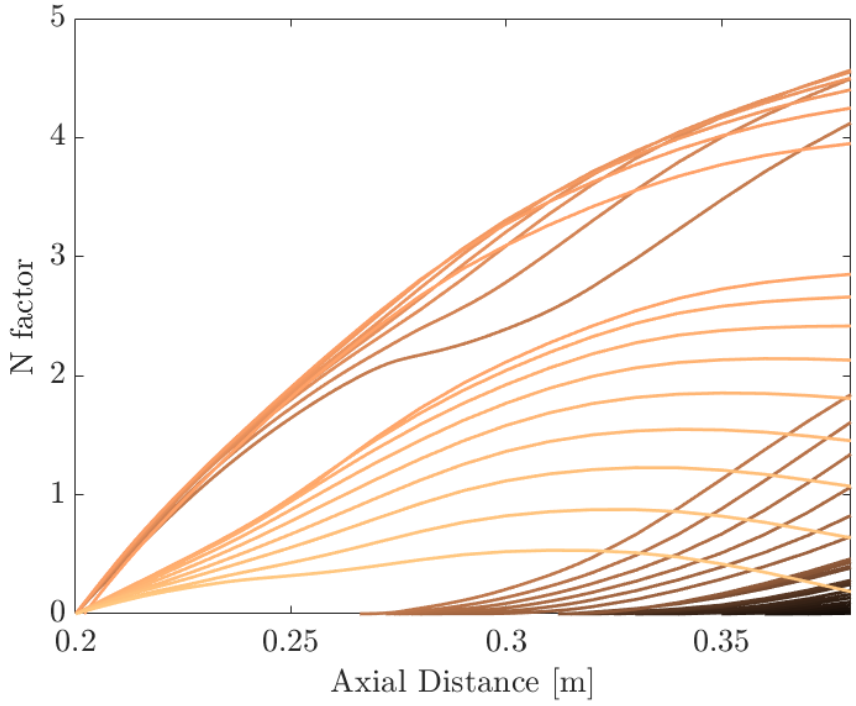

Figure 5.10: N factor as a function of position. Each line represents a separate frequency, ranging from 15 kHz (the darkest line) to 250 kHz (the lightest line) in 5 kHz steps. The most-unstable frequency is 180 kHz with an N factor of about 4.5. Reprinted with permission from Riha et al. [51].

5.3.1 Comparison with Experiments

Turning to the experimental data of Turbeville & Schneider [70], pressure fluctuations are available for a $Re' = 7.0 \cdot 10^6$ 1/m case at 0.33 meters from the nose tip. This case is identified as transitional, and clear peaks can be seen in the frequency data. In figure 14, their spectrum shows significant pressure signatures at $\Theta = 31°$ and 33° concentrated at 180 kHz. Computationally, 190 kHz is found to be the most amplified at this axial location. The bandwidth of the pressure data is very similar to that reported here, with the sensor located at 31 degrees showing frequencies between 160 and 200 kHz within a third of the peak amplitude. The full support of these peaks ranges from about 140 to 210 kHz, beyond which background noise or other instabilities take over.

For the 160–205 kHz band detected with SBG, there is a strong signature of the pressure eigenfunction at the wall. In figure 5.12, the absolute value of the pressure perturbation for 160, 180,

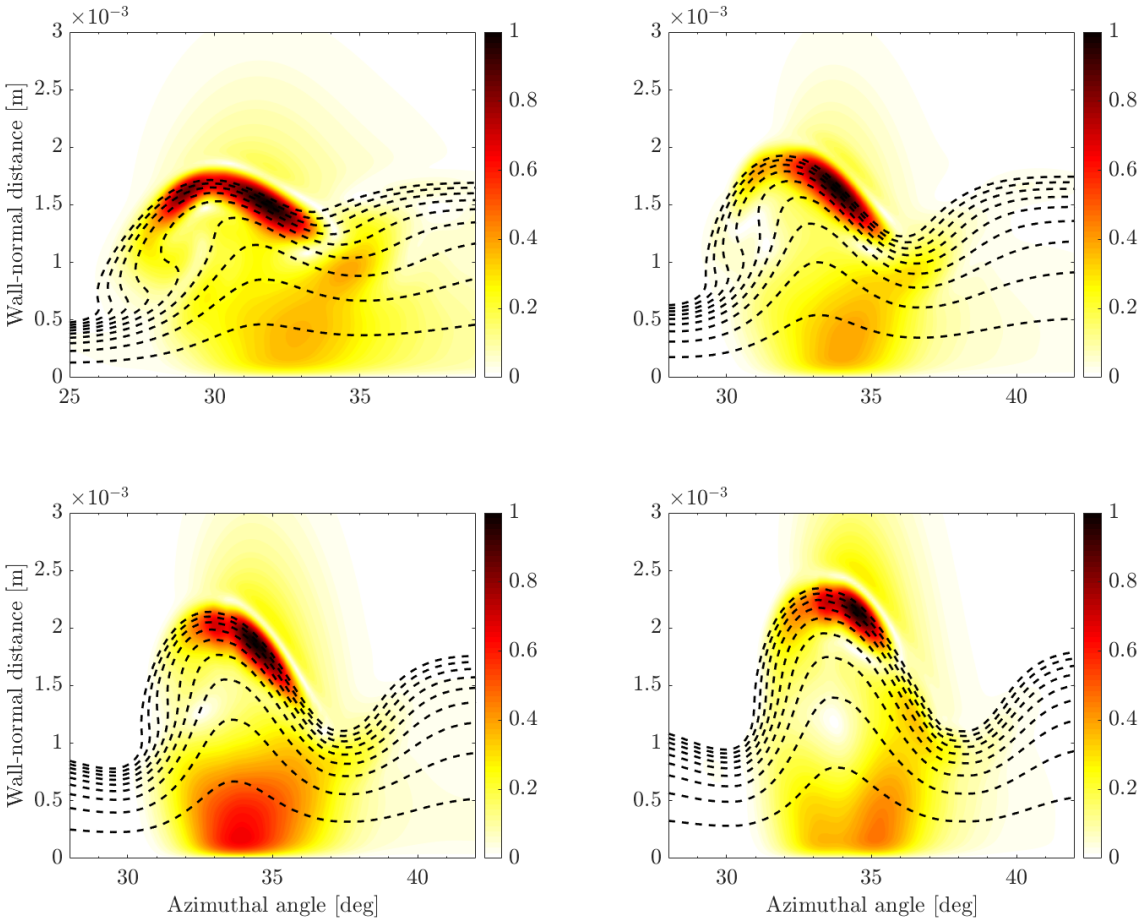

Figure 5.11: The streamwise velocity eigenfunctions for four X locations at 180 kHz. The color contour is $|\check{\hat{u}}_N|$, while the dashed lines represent contours of $\bar{\rho}\bar{u}_C$ mass flux. From the left to right and top to bottom, the X locations are 0.200, 0.260, 0.320, and 0.380 m. Note that the abscissa axis is shifted for the top-left figure, as the vortex core is slightly closer to the fin. Reprinted with permission from Riha et al. [51].

and 200 kHz at $X = 0.330$ m is shown. All eigenfunctions are normalized by their respective maxima in $|\hat{u}|$. Most of the pressure perturbation is concentrated tightly under the vortex, with a small concentration on its shoulder for 180 and 200 kHz. Along the wall, the strongest regions of $|\hat{p}|$ range from about 32–37 degrees away from the fin, with peaks at 34 and 35 degrees. This region is where the instability should be strongly detected by a wall-pressure sensor. Notably, this is shifted slightly from the 31–33° shown experimentally. However, taking into account the repeatability of the streak location and effective sensing diameter of the pressure sensors as reported by Turbeville & Schneider [70], the experimental range of detection could be as large as 29–35 degrees. This overlaps with the SBG eigenfunctions enough that both sensors could have detected the eigenfunctions shown in figure 5.12.

Other peaks in reference [70], such as one at 250 kHz and one at 75 kHz, were not detected in this study. This is due to the downstream location at which the initial instability search occurred. The modes that manifested in the experiments likely were either stable or more-stable than the mode detected at $X = 0.38$ m. The upstream region will be explored more in Chapter 6.

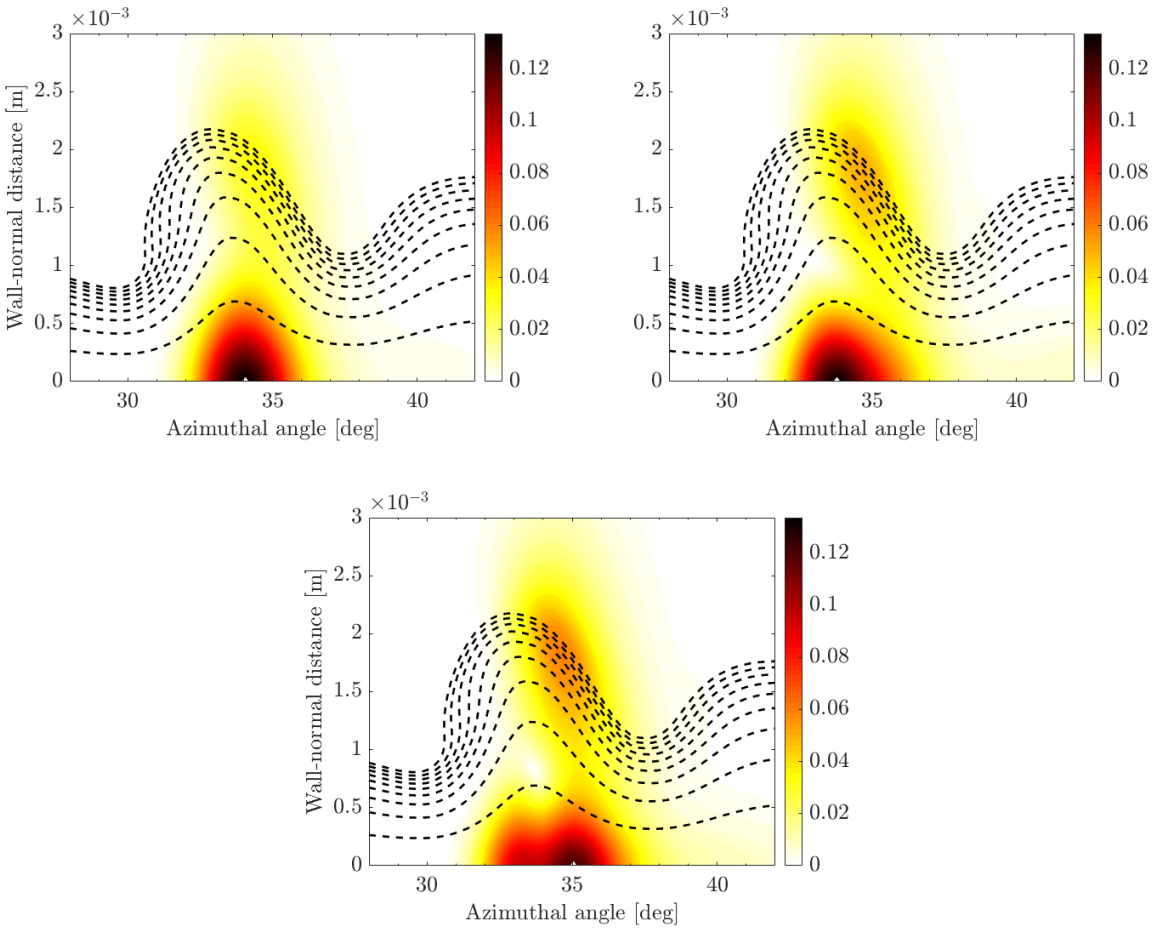

Figure 5.12: The pressure eigenfunctions for three frequencies at $X = 0.330$ m. The color contour is $|\hat{p}|$, while the dashed lines represent contours of $\bar{\rho}\bar{u}_C$ mass flux. From the left to right and top to bottom, the frequencies are 160, 180, and 200 kHz. A white triangle marks the maximum of the pressure signature along the wall in each case. Reprinted with permission from Riha et al. [51].

6. FINNED CONE: CASE II

6.1 Basic State

6.1.1 Grid Convergence

Case II provides a Reynolds number that was confirmed experimentally to be laminar. In addition, there is significantly more pressure fluctuation data [70, 72, 73]. A series of lessons that were learned in studying Case I were applied to Case II. One improvement that could be made was in the CFD surrounding the front of the cone. For much of the region in front of the fin, the flow is axisymmetric. Significant computational savings can be obtained by running the solution in two parts.

The different domains are shown in figure 6.1. The problem was actually split into three domains. Domain 1 was an axisymmetric simulation from the nose to roughly $X = 5 \cdot 10^{-3}$ m, and domain 2 runs from the end of domain 1 to $X = 0.1$ m. Domain 2 overlaps both domain 1 and domain 3, the full 3-D grid. The cell counts for domains 1 and 2 were 500×224 and 450×224, respectively. A grid-convergence study looking at basic-state quantities confirmed that these grid resolutions fully resolved the axisymmetric flow features [84]. This same convergence study also confirmed that the start of domain 3 was far enough upstream of the fin to avoid missing any 3-D effects.

Once the inflow had proved satisfactory, a convergence study was done with the fully 3-D domain 3. The number of nodes used in each solution are shown in table 6.1. Compared to table 5.3, this technique allows for less points to be used in the streamwise direction, and more points resolving the wall-normal and azimuthal features. The same four slices as in figure 5.4 are reproduced under the Case II conditions in figure 6.2. Visually, the different solutions are much closer to each other. There are only slight differences between the coarse and medium solutions visible at the back two slices. The axisymmetric inflow results in significantly better resolution of the 3-D solutions on the cone vortex.

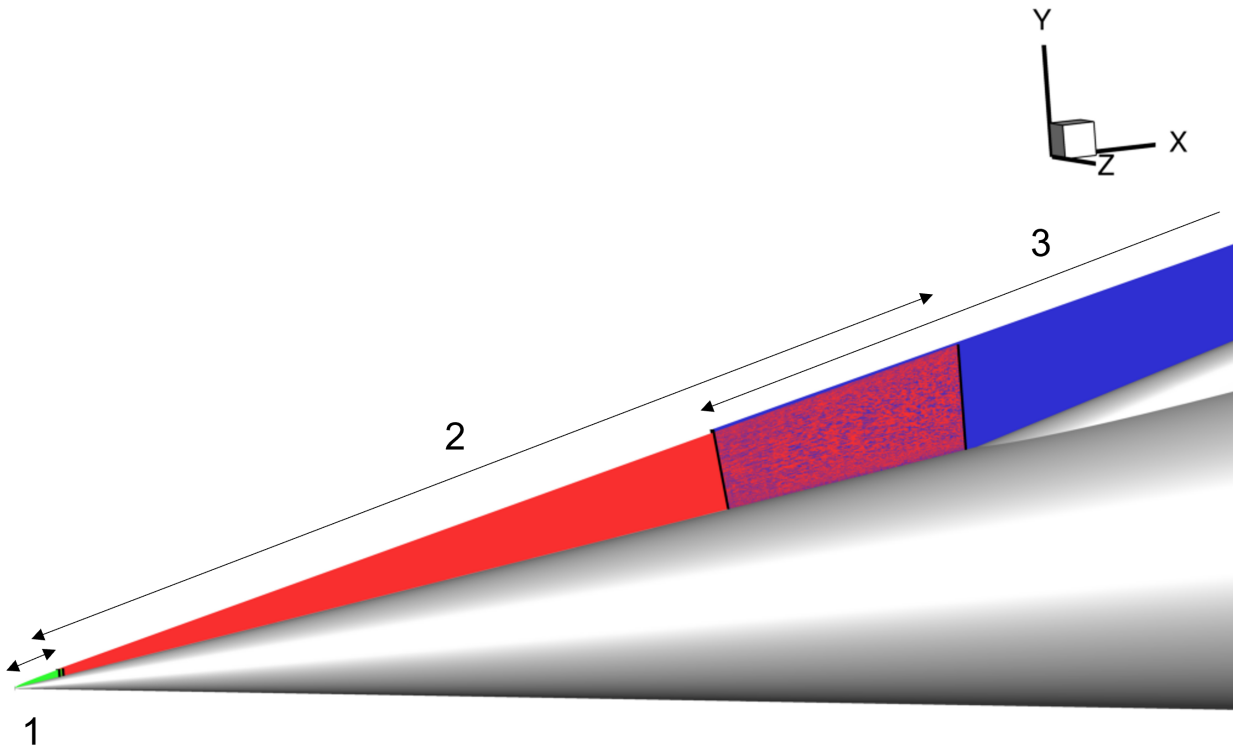

Figure 6.1: The overlapping domains used to simulate the finned cone. Domain 1 extends from the nose to $X = 5 \cdot 10^{-3}$ m, domain 2 from $X = 5 \cdot 10^{-3}$ to $X = 0.1$ m, and domain 3 from $X = 0.075$ m to the end of the cone.

Resolution	Streamwise	Wall-Normal	Azimuthal	Total (millions)
Low	501	380	480	91
Medium	629	480	601	181
High	800	605	755	365

Table 6.1: Node counts for the convergence study for Case II.

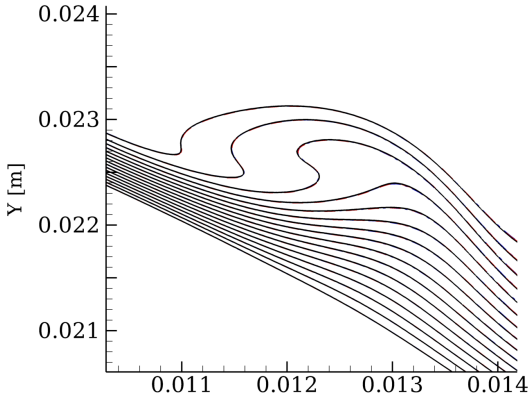

(a) $X = 0.20$ m

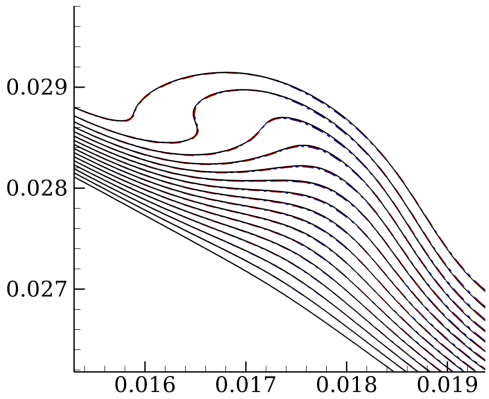

(b) $X = 0.26$ m

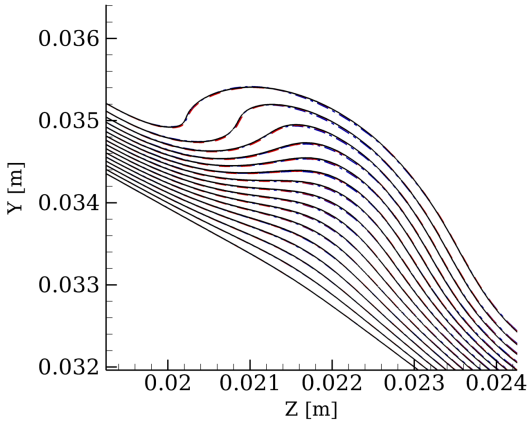

(c) $X = 0.32$ m

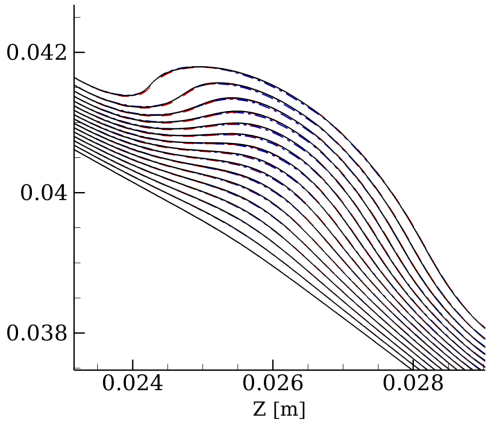

(d) $X = 0.38$ m

Figure 6.2: Evolution of the cone vortex on coarse (blue), medium (red), and fine (black) grids. Contours are of $\bar{u}$.

6.1.2 Vortex Path

The vortex was extracted using tools in Tecplot and fit to a ratio of two 3rd-order polynomials in a least-squares manner in the χ-Θ space. (The equation and coefficients used can be found in equation 6.1 and table 6.2, respectively.) It was then projected to the cone's surface to act as the anchor for the stability grids. The vortex path is seen in red in figure 6.3. The contours of density on the two Y-Z planes show the position of the vortex relative to the extracted path, and it can be seen that the path follows the inboard part of the vortex, near the thinnest region of the boundary layer.

The same path is also shown in figure 6.4a. The vortex moves steadily away from the wall from the fin-cone intersection until about $\chi = 0.3$ m. (Recall that X and χ are equivalent coordinates.) From there, the vortex almost follows a ray of the cone, but inspection of figure 6.4b shows that the vortex actually turns back toward the fin beyond $\chi = 0.34$ m.

$$f(x) = \frac{p_1 x^3 + p_2 x^2 + p_3 x + p_4}{x^3 + q_1 x^2 + q_2 x + q_3} \tag{6.1}$$

p_1	p_2	p_3	p_4	q_1	q_2	q_3
28.79	-11.33	1.675	-0.08500	-0.4159	0.06514	-0.003372

Table 6.2: Coefficients used in the rational polynomial representing the path of the vortex in χ-Θ space.

6.2 Stability Domains

For the following discussion on stability domains, a representative instability at 180 kHz will be used as a baseline case. The details of this perturbation will be discussed more in section 6.3.

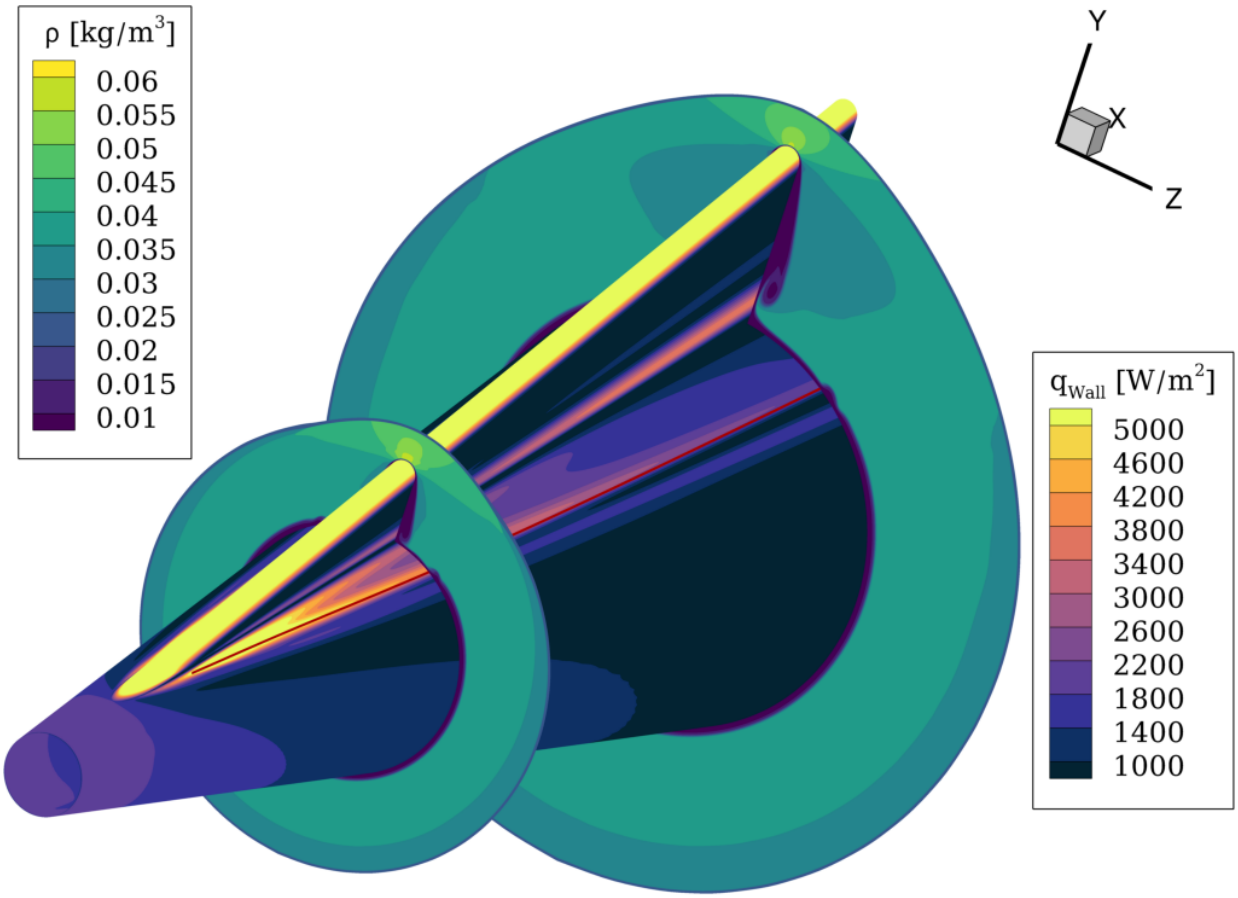

Figure 6.3: The flowfield for Case II. The surface contour is of heat flux, and the two slices show density contours. The red line on the cone surface is the vortex path fit.

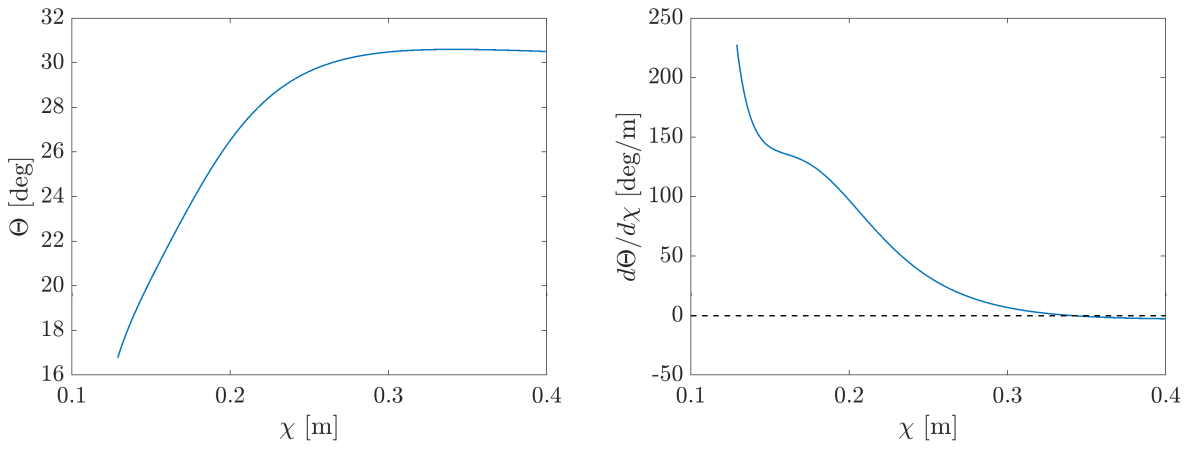

(a) (b)

Figure 6.4: Vortex path shown as Θ vs χ, along with its derivative.

6.2.1 Orientation of the Instability

As mentioned in Chapter 2, the choice of the ξ direction is integral to satisfying the assumptions of spatial BiGlobal. In Case I, the stability domain is based on the intersection of a Y-Z plane and the cone. This curve is extruded orthogonally from the wall in the regions away from the fin. At a certain distance from the fin, the domain warps until the $\Theta = 0^\circ$ boundary is parallel to the symmetry plane as well as orthogonal to the fin leading edge. These choices assert that in the region where the instability is active, the direction that minimizes $\partial/\partial\xi$ of the basic state is along a ray of the cone.

In Case II, a different approach is taken. Here, $\boldsymbol{a}_\xi$ is chosen to follow the vortex core. This is consistent with previous SBG applications to NPSE vortices, where the SBG plane is taken to be orthogonal to the vortex path [26]. Figure 6.4a shows that the vortex does not point along a ray of the cone for any significant length; even when it is close, there is usually a deviation. Choosing ξ to track the vortex path should minimize the model error associated with SBG, given the nonparallel nature of the boundary layer.

The next choice is how to handle the definition of the stability surface. As previously mentioned, with the nonorthogonal form of the SBG equations, $\boldsymbol{a}_\xi$ is decoupled from normal to the stability surface $\hat{\boldsymbol{n}}_S$. At the cone wall, the vortex direction is used to define $\boldsymbol{a}_\xi$ at the intersection of the vortex core and the stability surface. At that location, $\hat{\boldsymbol{n}}_S \parallel \boldsymbol{a}_\xi$. Instead of devising a complicated method of tracking the best direction for ξ throughout the rest of the domain, $\hat{\boldsymbol{n}}_S$ is held constant along the entire surface. This defines a plane.

Figure 6.5 shows the differences between the two stability-surface methodologies. The black line is the vortex path, the green grid is one from Case I, and the blue grid is one used in Case II. The green grid can be seen to be orthogonal to the top and bottom of the cone, as well as the leading edge of the fin. Its geometry is only slightly distorted from a cone frustum. The blue grid is a plane that is only orthogonal to the cone at its intersection with the vortex path.

Next, a series of these surfaces are created along the length of the cone, each based off the local intersection of the vortex with the stability plane. $\boldsymbol{a}_\xi$ is then defined by pointing pointwise from the

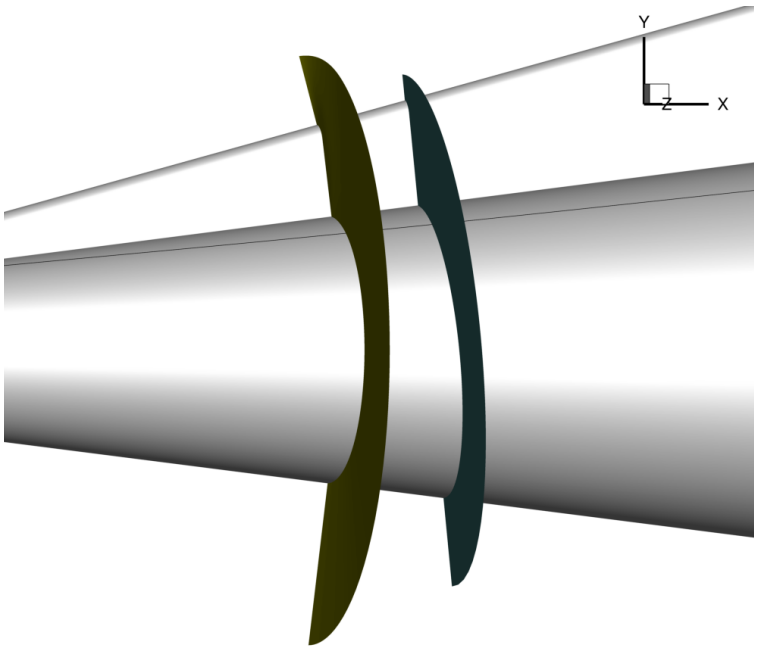

Figure 6.5: Comparison of stability grids for the two cases. The grid for Case I at $X = 0.25$ is in green, and the grid for Case II is in blue at $X = 0.27$. The vortex path is shown in black for reference.

(η, ζ) combination at one surface to the same (η, ζ) at the next surface. Approaching the $\Theta = 180°$ boundary, $\boldsymbol{a}_\xi$ smoothly changes from parallel to the vortex core in its viscinity, to parallel with a ray of the cone. This behavior is demonstrated in figure 6.6. For most modes investigated here, the vast majority of the mode falls within the region where $\theta_N \leq 1°$.

$$\theta_N = \left| \cos^{-1} \left(\frac{\boldsymbol{a}_\xi \cdot \hat{\boldsymbol{n}}_S}{|\boldsymbol{a}_\xi|} \right) \right| \tag{6.2}$$

6.2.2 Effect of Domain Truncation

During investigations into the Case-I basic state, the instabilities that were found seemed focused in the vortex, and visually appeared to rapidly die off away from the vortex. Those grids also used 500 points in the ζ dimension, with only 291 in the vortex region. In the interest of faster stability calculations, smaller domain sizes were investigated to see if the modes could still be properly resolved.

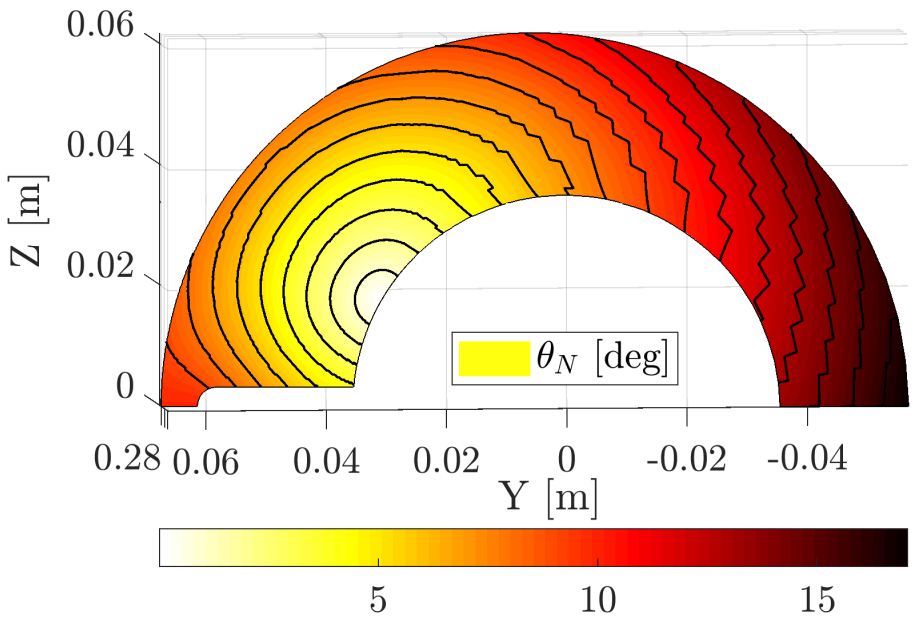

Figure 6.6: Contour of θ_N at $X = 0.28$, where θ_N is defined by equation 6.2. Each contour line is a one-degree increment.

The first domain attempted is shown in figure 6.7. The vortex path intersects this grid at $X = 0.282$ meters. The color map is showing $\left|\check{\hat{u}}_N\right| / \max\left|\check{\hat{u}}_N\right|$, the magnitude of the physical component of the first velocity perturbation component scaled by its maximum. (See section 3.2.3 for details on physical components.) The blue lines are contours of $\bar{\rho}\bar{u}_C$ to show the shape of the local boundary layer. Dotted black lines show contour levels of the pressure perturbation scaled by $\max\left|\check{\hat{u}}_N\right|$. The most outer level corresponds to $|\hat{p}| / \max\left|\check{\hat{u}}_N\right| = 10^{-13}$, with each step towards the perturbation representing an order of magnitude increase (10^{-12}, 10^{-11}, etc.). The contours of mass flux show that the left boundary is very close to the fin, and has dipped inside the edge of the vortex on the fin. While the colored portion of the eigenfunction appears quite small, the pressure perturbation has a very large area of influence, extending far outside of the boundary layer. In the inviscid region of the flow, the distance between the isocontours of $|\hat{p}|$ is roughly equal. This indicates exponential decay of the perturbation as a function of distance from the vortex. The flick-

ering at the outermost contour lines suggests that the magnitude of the eigenfunction has decayed to near machine precision for this problem. However, this level is not reached on the left and right boundaries. The artificial Dirichlet conditions on these boundaries are still influencing the solution.

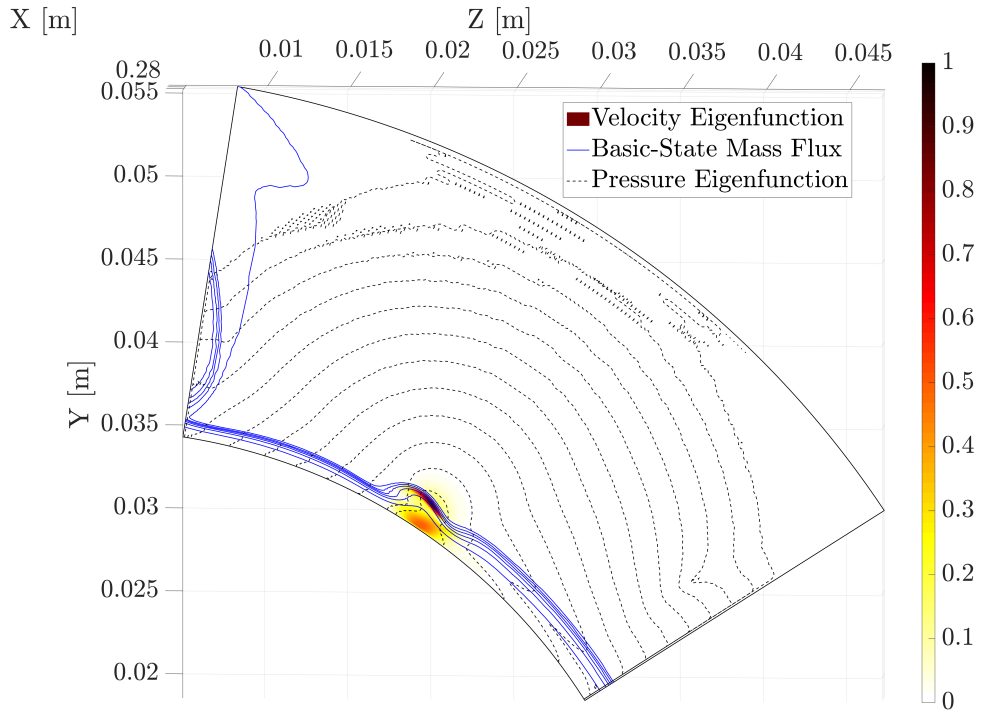

Figure 6.7: Truncated domain with $\Theta_L = 8.4°$ and $\Theta_R = 57.6°$. Blue lines are contours of $\bar{\rho}\bar{u}_C$, dashed black lines are $|\hat{p}| \,/\, \max\left|\check{\hat{u}}_N\right|$, and the color map is $\left|\check{\hat{u}}_N\right| \,/\, \max\left|\check{\hat{u}}_N\right|$.

In figure 6.8, the left boundary is extended up the fin all the way to the basic-state symmetry plane. The effects of the pressure perturbation extend half-way up the fin before decaying below 10^{-13}. This demonstrates the importance of including the fin in the stability calculation. As in the previous domain, the pressure contours change how they propagate moving from outside the boundary layer to inside. The rate of decay along the wall is slower moving away from the fin than toward it, and the contours are significantly distorted as they pass through the strong mass-flux gradients of the boundary layer.

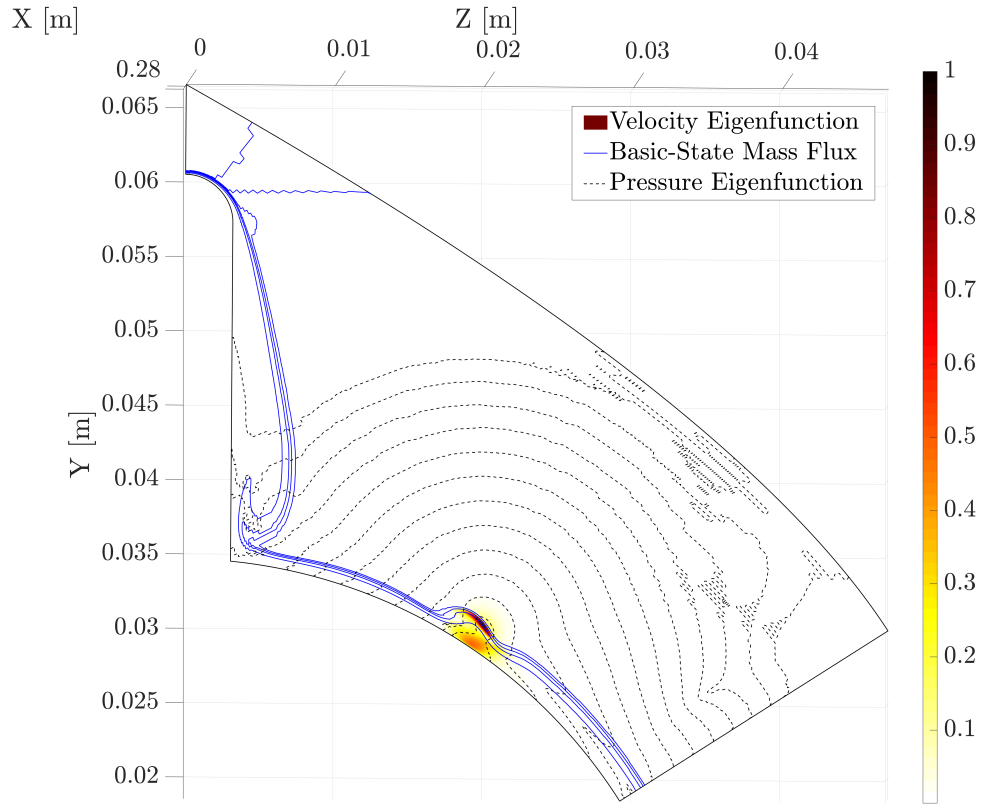

Figure 6.8: Truncated domain with $\Theta_L = 0°$ and $\Theta_R = 57.6°$. Blue lines are contours of $\bar{\rho}\bar{u}_C$, dashed black lines are $|\hat{p}| \,/\, \max|\check{\hat{u}}_N|$, and the color map is $|\check{\hat{u}}_N| \,/\, \max|\check{\hat{u}}_N|$.

The next three grids show the true extent of the instability. In figure 6.9, the right boundary is extended to $90°$. At about $\Theta = 60°$, the decay of the perturbation changes. From $\Theta = 0°$ to $60°$, the contour lines of $|\hat{p}|$ are similar in shape to concentric circles with the vortex as the center. Beyond $\Theta = 60°$, the contours are no longer perpendicular with a position vector originating from the vortex. The decay is still exponential, but at a much slower constant. Figure 6.10 extends the right boundary to $\Theta = 120°$. Here, the 10^{-13} contour has finally reached the wall. To finish the study, 6.11 shows the full domain, wrapping from symmetry plane to symmetry plane. The story is similar to figure 6.10 in terms of the azimuthal extent of the perturbation, with the last contour line extending a similar distance.

Table 6.3 summarizes the characteristics of the various domains, along with dimensional α

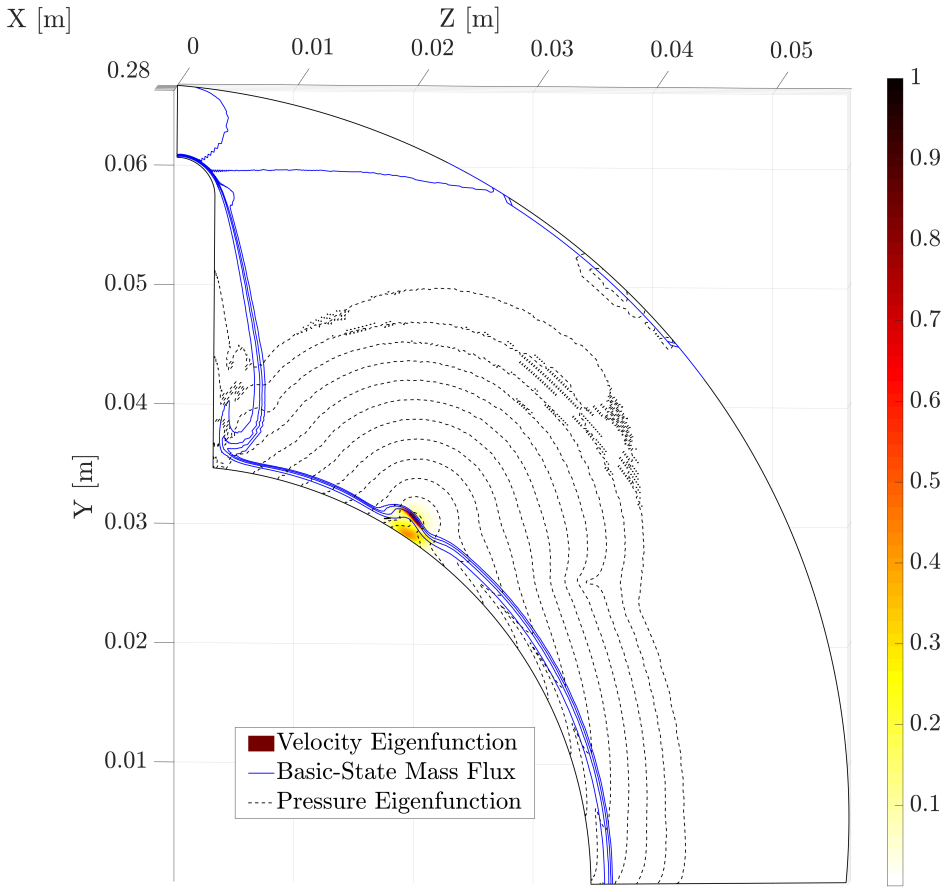

Figure 6.9: Truncated domain with $\Theta_L = 0°$ and $\Theta_R = 90°$. Blue lines are contours of $\bar{\rho}\bar{u}_C$, dashed black lines are $|\hat{p}| \,/\, \max\left|\check{\hat{u}}_N\right|$, and the color map is $\left|\check{\hat{u}}_N\right| \,/\, \max\left|\check{\hat{u}}_N\right|$.

Θ_L [deg]	Θ_R [deg]	n_z	n_{Order}	α_r [m^{-1}]	α_i [m^{-1}]
8.4	57.6	301	4	$1.456 \cdot 10^3$	$-3.457 \cdot 10^1$
0	57.6	411	6	$1.458 \cdot 10^3$	$-3.214 \cdot 10^1$
0	90.	501	6	$1.466 \cdot 10^3$	$-3.451 \cdot 10^1$
0	120.	649	6	$1.468 \cdot 10^3$	$-3.522 \cdot 10^1$
0	180.	651	4	$1.473 \cdot 10^3$	$-3.700 \cdot 10^1$

Table 6.3: Effect of the stability grid's right boundary on α. Θ_L and Θ_R refer to the Θ values of the left and right boundaries of the grid, respectively. n_{Order} refers to the accuracy of the finite differences used on the basic state. All grids have $n_y = 401$, and the stability derivatives are 4$^{\text{th}}$-order accurate.

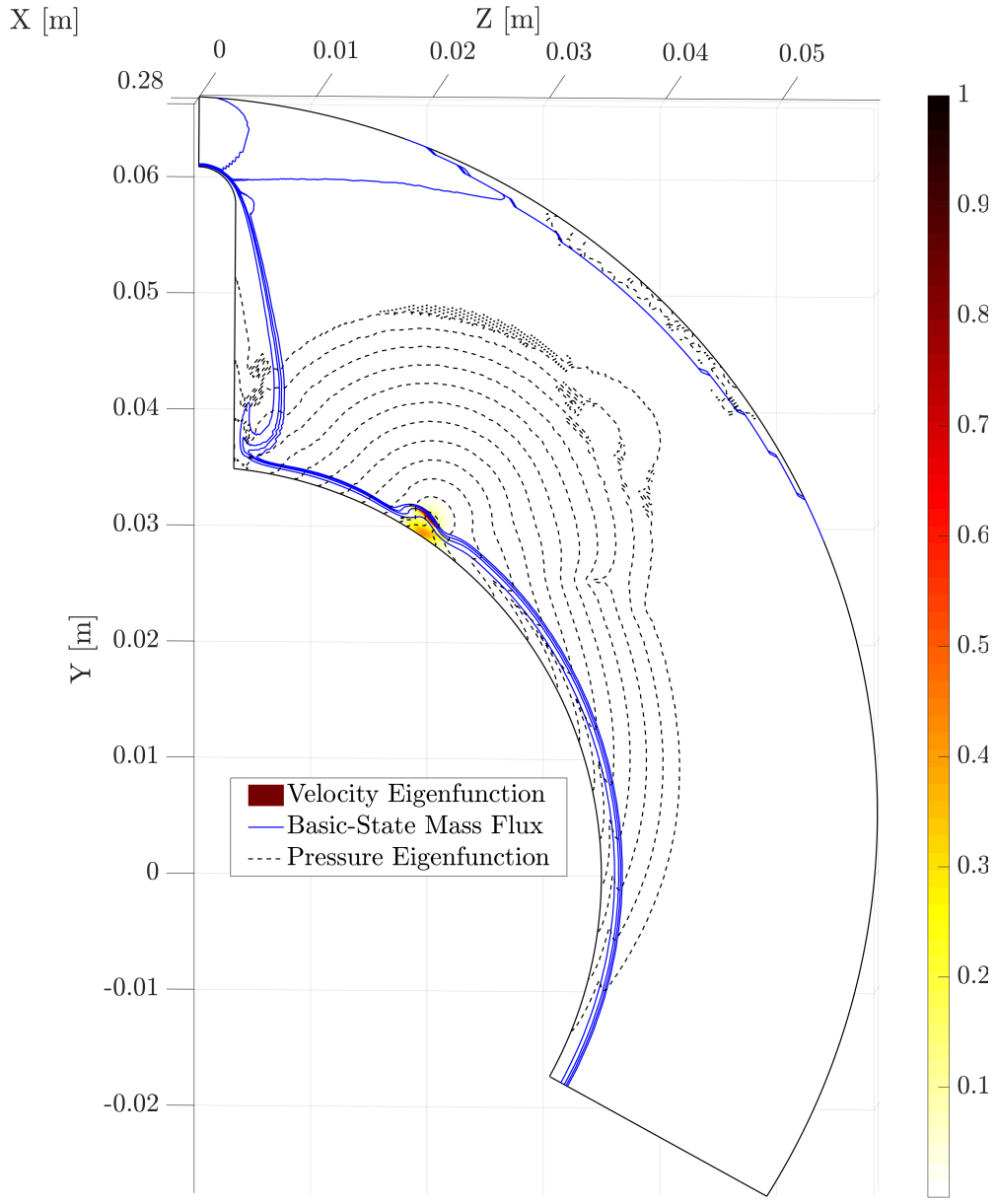

Figure 6.10: Truncated domain with $\Theta_L = 0°$ and $\Theta_R = 120°$. Blue lines are contours of $\bar{\rho}\bar{u}_C$, dashed black lines are $|\hat{p}| \,/\, \max\left|\check{\hat{u}}_N\right|$, and the color map is $\left|\check{\hat{u}}_N\right| \,/\, \max\left|\check{\hat{u}}_N\right|$.

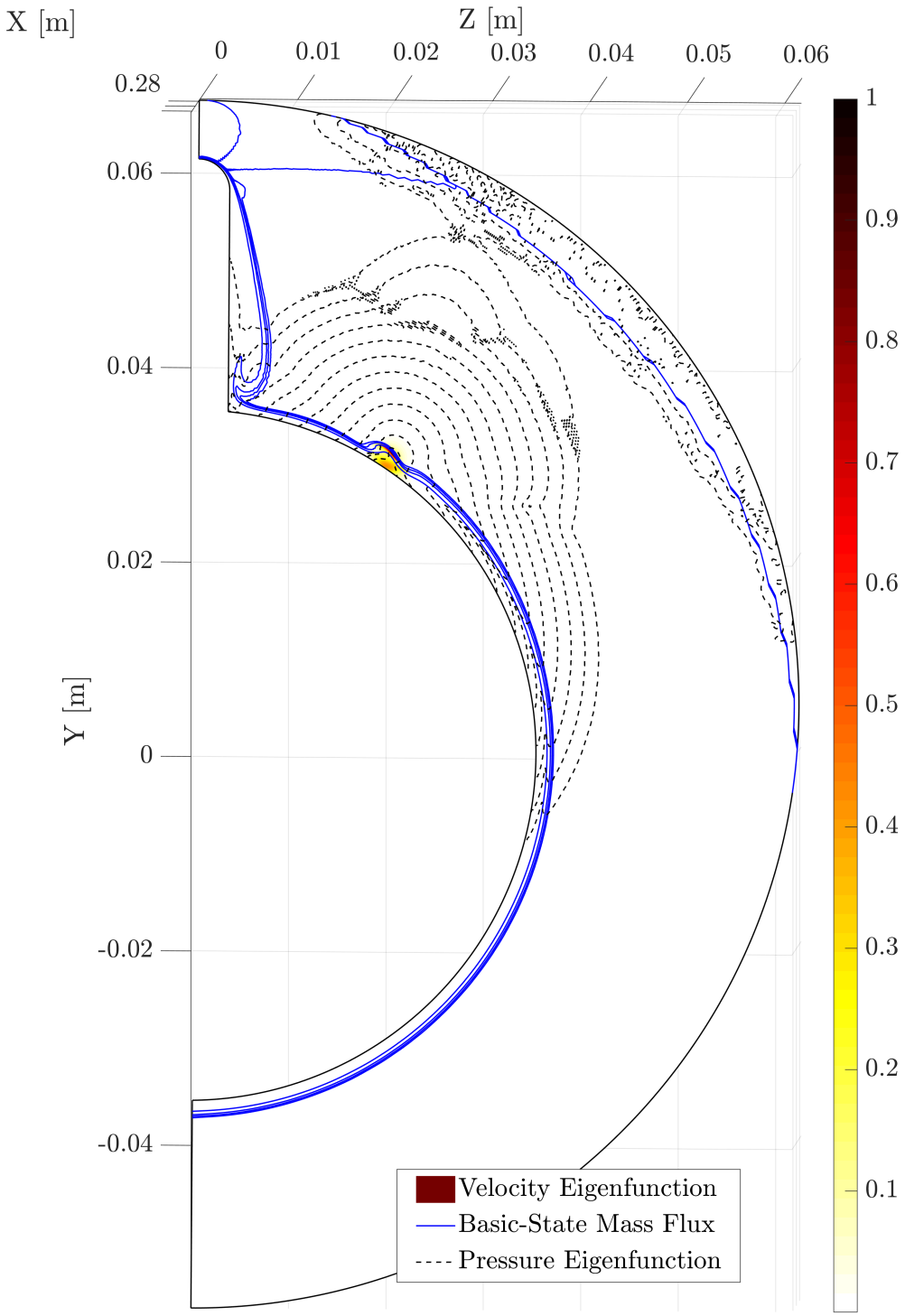

Figure 6.11: Full domain with $\Theta_L = 0°$ and $\Theta_R = 180°$. Blue lines are contours of $\overline{\rho}\overline{u}_C$, dashed black lines are $|\hat{p}| \,/\, \max\left|\check{\hat{u}}_N\right|$, and the color map is $\left|\check{\hat{u}}_N\right| \,/\, \max\left|\check{\hat{u}}_N\right|$.

(as described by section 3.2.1). Some important caveats should be mentioned about this study. The finite-difference order used to calculate derivatives of the basic state were different in the smallest and largest grids relative to the others. (The finite-difference order for derivatives of the perturbation were 4^{th} order for all of the domains.) The freestream boundary of the stability domain is defined slightly differently between the different grids. However, this likely has a small effect, as the perturbation is of order 10^{-12} or less before it interacts any with this boundary. The larger influence with this boundary is how much of the outer oblique shock is included in the domain. The grid in figure 6.11 catches more of the shock than the other grids, and results in the perturbation being active at low levels in its vicinity. This is likely due to the well-known issue high-order methods have with shocks: sharp changes in the solution cause wiggles in the derivatives. Luckily, the cone shock is far enough away from the solution that the effect on the perturbation is at very low magnitudes. Also, these solutions are not grid-converged. An effort was made to keep the grid density roughly the same in the regions that overlapped with previous grids, which is why the value of n_z increased with each subsequent domain.

Even with these limitations, these grids show that the perturbation has a very large footprint. For this instability, the right boundary needs to extend to at least 120 degrees, and the left boundary needs to extend most of the way up the fin. If the SBG solution is active on the boundary, the solution can be affected in unpredictable ways. If a perturbation is not given sufficient room to decay, the boundary condition can keep the solution from converging. A grid-independent solution as $\Delta\eta, \Delta\zeta \to 0$ is no longer guaranteed. Table 6.3 shows that even α was affected by the location of the boundaries, significantly for the growth rate. It is possible to circumvent this issue by implementing a buffer region between the solution and the boundary condition. The function described in section 3.5.2 could be adapted for this purpose. However, this buffer would likely need to be adjusted as the vortex moved along the cone, or as the perturbation changes character across different frequencies. The simpler solution when looking at multiple frequencies, X locations, and instabilities, is to ensure that the left and right boundary conditions are applied at the symmetry planes of the finned cone. This is the approach that was adopted here.

6.2.3 Stability Grid Convergence

After the determination was made that the full 180° domains were needed, grid-convergence tests were begun. In addition to the $n_z = 651$ grid mentioned in the last section, a new set of grids were made where the azimuthal distribution of points was rearranged to cluster near the vortex as much as possible. The test instability was converged at $X = 0.282$ m, then marched upstream and downstream with the Newton–Raphson technique in 1 mm steps. Three new grids were constructed, with 401, 601, and 1201 points in ζ. The number of azimuthal points near the vortex for each grid is shown in table 6.4. n_y is held constant based on convergence tests with Case I, with an off-wall spacing of 10^{-6} m. The basic-state derivatives were 4$^{\text{th}}$-order accurate with the 10$^{\text{th}}$-order filter applied afterwards, and the stability derivatives were also 4$^{\text{th}}$-order accurate.

The resulting α_r and α_i are shown in figures 6.12. The solutions from the $n_z = 651$ grid gets worse upstream, but the three other grids are visually indistinguishable except for a small region near $X = 0.22$ m. The error measure defined by equation 4.1 with the $n_z = 1201$ solution as the true value can be found in figure 6.13 for the three other grids. For this instability, the $n_z = 401$ had a relative error of less than 0.1% throughout the X region shown. Based on this information, a grid size of 401×401 was chosen for the rest of the solutions.

Total n_z	Vortex n_z
651	176
401	201
601	351
1201	751

Table 6.4: n_z counts compared to the number of points near the vortex.

It was mentioned in the previous section that those results were not necessarily grid converged. As a comparison, figure 6.14 shows the decay of the eigenfunction within the 401×1201 domain.

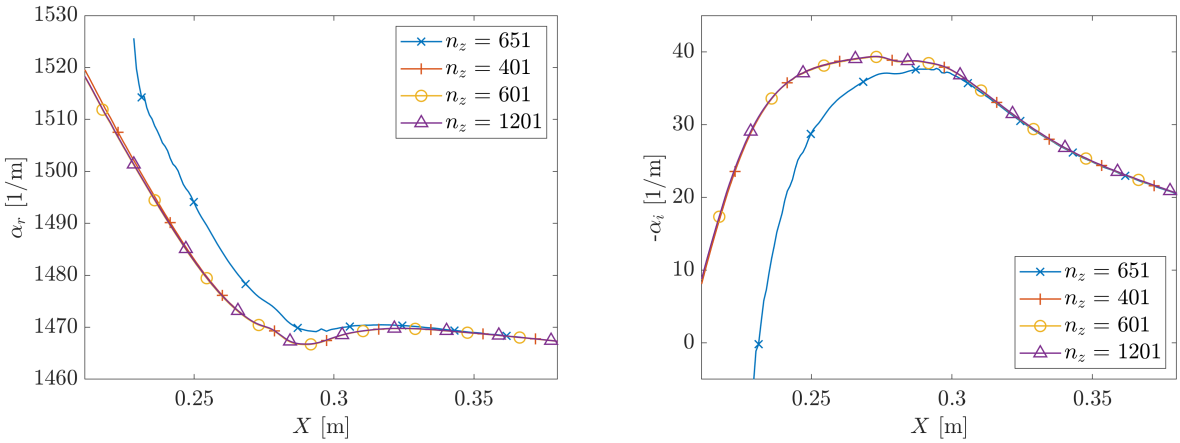

(a) (b)

Figure 6.12: α for the test solution for three spanwise grid densities.

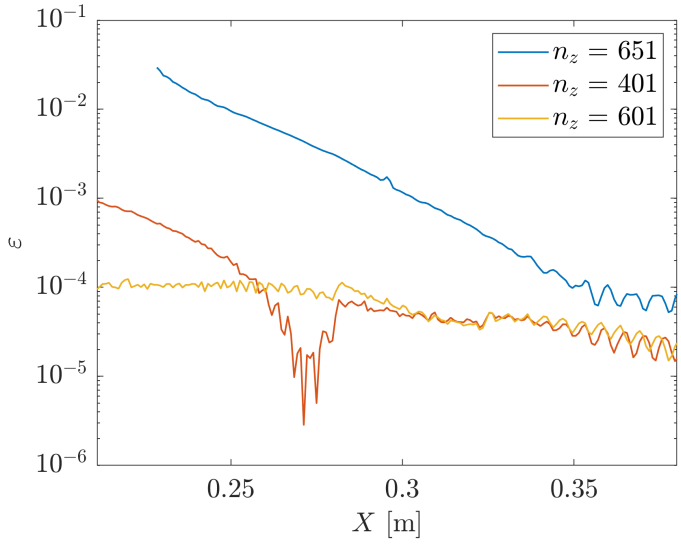

Figure 6.13: Relative error of the 651, 401, and 601 n_z solutions compared to the $n_z = 1201$ grid.

The $|\hat{p}| \,/\, \max\left|\check{\tilde{u}}_N\right| = 10^{-13}$ contour extends even further than the 401×651 grid, reaching $\Theta = 130^\circ$ on the more-resolved solution. This further reinforces the idea that allowing the stability domain to extend from the $+Y$ symmetry plane to the $-Y$ symmetry plane is the safest approach to ensure the eigenfunction can fully decay before reaching the boundaries.

6.2.4 Effect of Streamwise Metrics

There has been discussion of how to handle geometrical curvature terms since at least 1955. Gregory et al. [85], in the first theoretical look at the crossflow instability, made a case both for and against including streamwise and transverse surface-curvature terms. Since then, it has been learned that surface curvature has notable effects on different instabilities, even though the terms are sometimes quite small [7, 10]. However, whether or not inclusion of these effects is consistent with the $\partial\bar{\phi}/\partial\xi = 0$ assumption in LST and SBG is still a matter of debate. With the nonorthogonal methodology employed in BLAST, the problem changes from inclusion of surface curvature to the 3-D distortion of the local coordinate system. This is a multilayered problem, and will be described in terms of curvature of coordinate lines.

The first point to make is that curvature terms cannot be eliminated entirely from the nonorthogonal SBG equations. In order for vectors to properly be represented, the metric tensor must be used. Any gradient operators on a vector or tensor require Christoffel symbols, which have partial derivatives of the metric tensor in all three coordinates. SBG does not make any assumptions about the η and ζ characteristics of the basic state or perturbation. This means terms like $\partial g_{ij}/\partial\eta$ and $\partial g_{ij}/\partial\zeta$, and any higher-order derivatives in η and ζ, must be included fully. So in this sense, transverse curvature is inherently built into the SBG assumptions.

The metric tensor is formed by first calculating the Jacobian of the transformation, $J^i_j = \partial X^i/\partial\xi^j$. The Jacobian also encodes the components of the basis vectors of the N frame represented in the C frame. So, if $\boldsymbol{a}_\xi = a^j\hat{\boldsymbol{\imath}}_j$, then $a^i = J^i_1$. This results in two ways to define $\boldsymbol{a}_\xi$. It can be set by prescribing the vector and using its components to define $\partial X^i/\partial\xi^1$. This is what was done for the calculations for Case I. The other option is to define the ξ coordinates in 3-D, and then calculate $\partial X^i/\partial\xi^1$ through partial derivatives in the same manner as the other two nonorthogonal

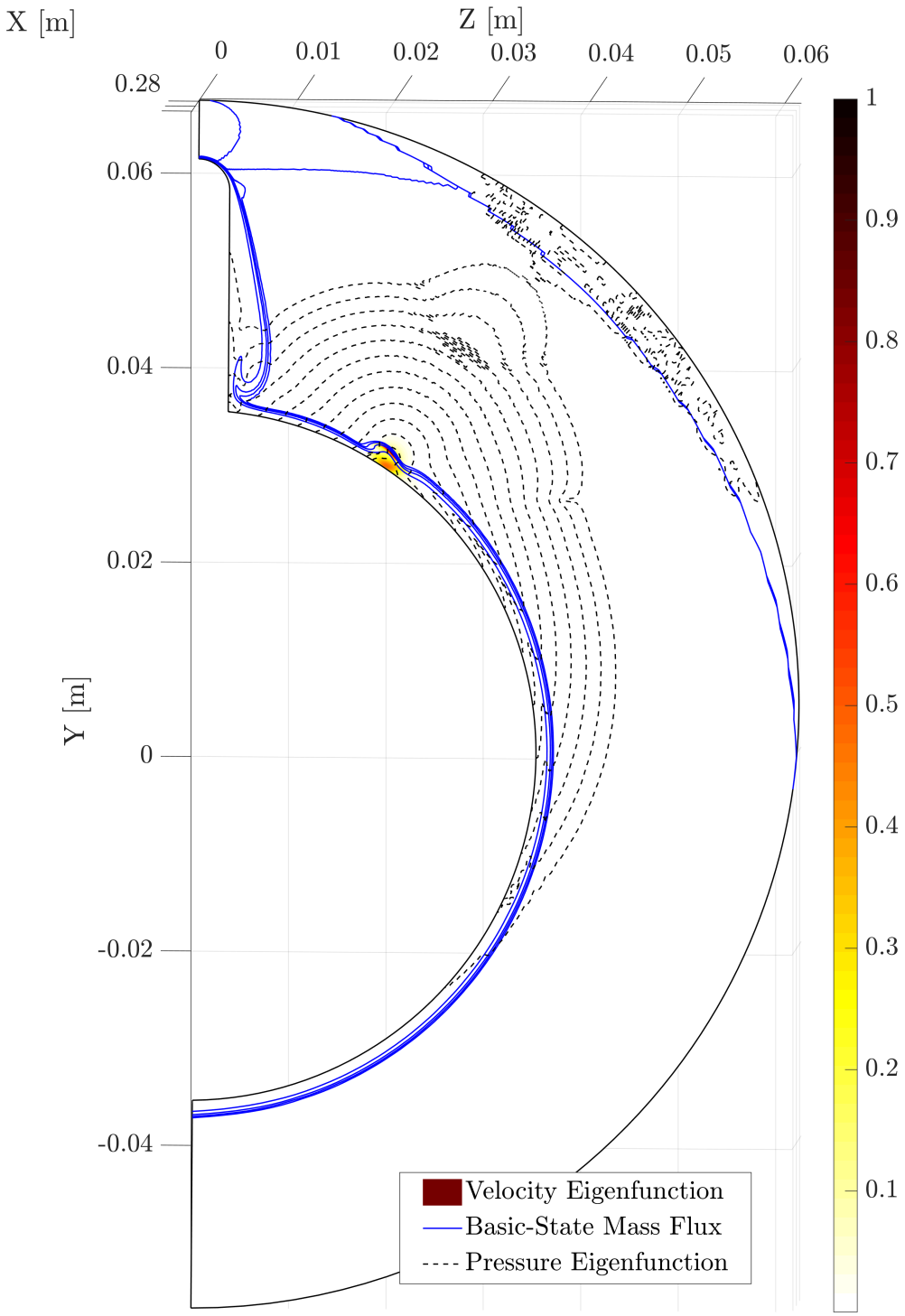

Figure 6.14: Full domain with $\Theta_L = 0°$ and $\Theta_R = 180°$. Blue lines are contours of $\overline{\rho}\overline{u}_C$, dashed black lines are $|\hat{p}| \,/\, \max\left|\check{\hat{u}}_N\right|$, and the color map is $\left|\check{\hat{u}}_N\right| \,/\, \max\left|\check{\hat{u}}_N\right|$.

coordinates. This does require generation of a full 3-D grid, as opposed to decoupled 2-D grids as before.

If $\xi(X, Y, Z)$ is defined, then partial derivatives of the metric tensor can also be taken with respect to ξ. The ξ derivative that defines $\boldsymbol{a}_\xi$ determines the direction of ξ, while $\partial g_{ij}/\partial\xi$ accounts for how the ξ coordinate is curving. This term (and higher-order ξ derivatives of it) can be set to zero independently of the choice for $\boldsymbol{a}_\xi$; this was done in the Case I results. For the calculations in Case II, full inclusion of $\partial g_{ij}/\partial\xi^k$ terms is the approach taken. However, the effect of this choice can also be examined.

Three options are compared, as shown in table 6.5. All three sets of calculations are run on the exact same grids; the only differences are the direction of $\boldsymbol{a}_\xi$ and the handling of ξ derivatives of the metrics. The differences in α can be seen in figures 6.15. The Metrics-Option-2 solution is very different in terms of growth rate compared to the Metrics-Option-1 solution. Up until $X = 0.243$ m, the solution is more unstable. Afterward, the effect is reversed. The wavenumber for Metrics Option 2 has similar behavior as that of Metrics Option 1, but only qualitatively. Metrics Option 3 is very similar to Metrics Option 1. This particular instability was destabilized by neglecting $\partial g_{ij}/\partial\xi$, but this is more mechanism dependent than a general truth. Similar examples of this behavior has been found using LST and PSE [7, 10].

The effect of these assumptions over a length of geometry are shown in figure 6.16, with the max N factors reported in table 6.5. The ΔN between Metrics Options 1 and 2 is 1.1, while it is only 0.6 between Metrics Options 1 and 3. This indicates that $\partial g_{ij}/\partial\xi$ is a lower-order effect than choosing the direction of $\boldsymbol{a}_\xi$. However, neither of the effects are negligible.

It is important to mention that smoothness of the 3-D grid is critical when it is used for ξ derivatives. Initial grids were constructed independent of each other and only smoothed in the η-ζ plane using Pointwise. This led to α_i vs X curves that were jagged at certain locations instead of the smooth ones seen in figures 6.15. The corrected methodology started by constructing a 2-D stability grid at each ξ location and solving them individually first. Then, the grids were all combined into a 3-D grid, which was then smoothed together as a whole. This helped smooth out

	Definition of $\boldsymbol{a}_\xi$	$\partial g_{ij}/\partial\xi$	Max N
Metrics Option 1	Defined by 3-D grid	Included	5.3
Metrics Option 2	Defined by stability-surface normal	0	4.2
Metrics Option 3	Defined by 3-D grid	0	5.9

Table 6.5: Differences between the three cases used to compare the effect of streamwise metrics.

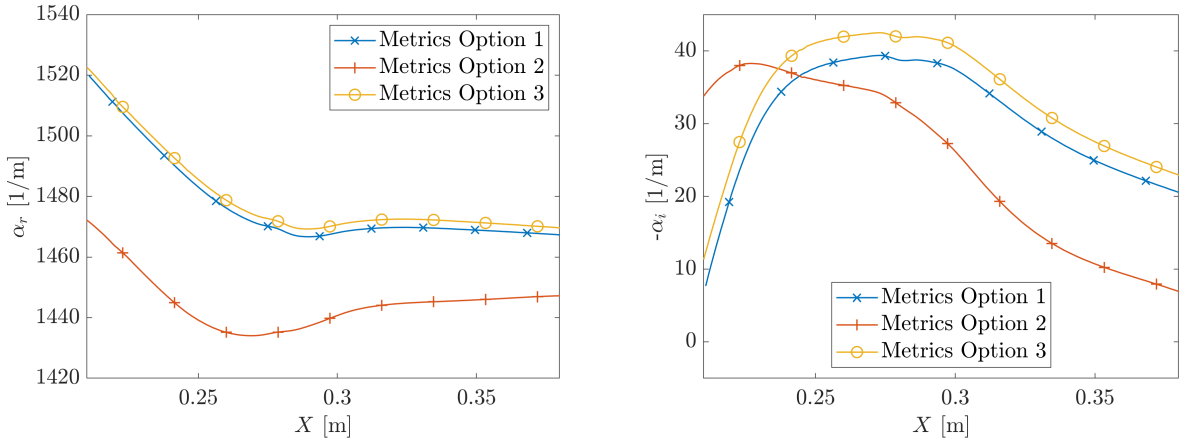

(a) (b)

Figure 6.15: α vs X for the three cases defined in table 6.5.

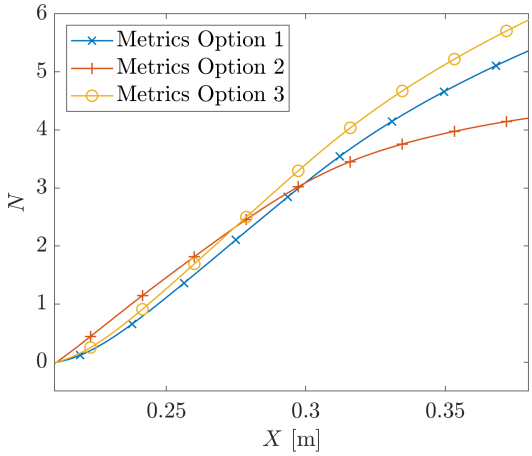

Figure 6.16: N factors for the three cases defined in table 6.5.

ξ coordinate lines, and successfully eliminated the spurious oscillations.

6.2.5 Effect of Contained Shocks

While a shock in the domain was only seen to affect a particular instability at low levels, it did make instabilities harder to find. In typical cases without shocks, an $n_{Arnoldi}$ of 200 is usually enough to find all of the physical instabilities in the vortex. When a shock is in the domain, it results in many spurious modes around the shock that dominate the Krylov subspace. $n_{Arnoldi}$ must be increased five times or more to recover the same modes as before. However, adding a buffer region over the shock during the Arnoldi algorithm alleviated the issue. Using the equations in section 3.5.2, a λ_{Max} of 10^5 successfully damped most of the spurious modes generated by the shock. The buffer region was then removed when the mode was converged with the Newton–Raphson method.

6.3 Stability Results

The next sections evaluate spatial BiGlobal results surrounding the vortex. First, a particular X station is analyzed in detail to show the different modes present at different frequencies. Then, a few specific modes are marched downstream to show trends in space. The following modes are calculated with 4^{th}-order finite differences on the 401×401 grid tested in section 6.2.3. Dirichlet boundary conditions were used at the $\eta = 0$ and $\eta = 1$ boundaries, except for $\hat{\rho}$ at the wall which was left unspecified. On the $\zeta = 0$ and $\zeta = 1$ boundaries, symmetry boundary conditions were compared with Dirichlet conditions. It was found that since the boundaries were far enough away from the solution that there was no difference between the two conditions. As a result, Dirichlet conditions were used because they are less likely to produce spurious modes attached to the boundaries during the eigenvalue-problem phase. All other numerical or physical options are specified as described in section 6.2.

6.3.1 Analysis of Local Modes

The X station chosen is at $X = 0.150$ m. As can be seen in figure 6.17, at this point the cone and fin vortices have just separated, with less than one cone-vortex width between the two. The fin vortex is still strongly affecting the cone vortex, and the thin boundary layer in the middle is about

six times smaller than the equivalent undistorted cone boundary layer.

A series of eigenvalue problems were initiated in 40 kHz increments between 20 and 400 kHz. The spectrum at each frequency was filtered for spurious solutions, and physical modes were marched in frequency space. 2 kHz steps allowed most modes to be tracked well, but this became more difficult in regions with multiple instabilities, especially when they were weakly unstable. The resulting modes that were found are plotted in figure 6.18. The top graph shows the dimensional growth rate and the bottom graph shows the phase speed nondimensionalized by the pre-shock freestream velocity. Five modes are shown. (The labels used are labels only and do not imply that these are first modes, second modes, or higher modes.) Mode 1 (M1) is the most unstable over most of the frequency domain, with a peak at 252 kHz. Mode 2 is the most unstable in a small vicinity around its peak at 198 kHz, and at frequencies below 86 kHz. Modes 3 and 4 (and possibly 5) are interesting because they appear to be shifted versions of Mode 2. Modes 2 and 3 even have the nearly the exact same phase speed in the 66–170 range. There is also a large number of modes not shown with $-\alpha_i \leq 20$ m^{-1} in the 200 to 300 kHz range. However, these modes were quite difficult to distinguish as frequency varies and are less unstable than the five other modes already shown, so they are omitted.

One of the common features of SBG solutions is demonstrated by the α_i vs f plot for Mode 1. There are particular frequencies where the behavior of the growth rate with frequency changes. Figures 6.19 show mode shapes at some of these points. Figures 6.19e and 6.19e show $-\alpha_i$ and c_{ph} versus frequency, with the markers denoting the frequencies chosen: 120, 194, 252, and 360 kHz. In figures 6.19a–6.19d, the perturbation quantity $\left|\check{\hat{u}}_N\right| / \max\left|\check{\hat{u}}_N\right|$ is plotted against dashed-black contours of basic-state mass flux. Figures 6.20 show $|\hat{p}| / \max\left|\check{\hat{u}}_N\right|$ at the same frequencies. All of the eigenfunctions are scaled against that specific frequency only, even though the same color scale is used for the velocity and pressure perturbations individually.

At 120 kHz, $\left|\check{\hat{u}}_N\right|$ sits primarily just to the right of the peak of the vortex, in a region of high shear. There is also a second, weaker band opposite the center of rotation of the vortex. The pressure eigenfunction is concentrated on the left side of the vortex, with a similar magnitude

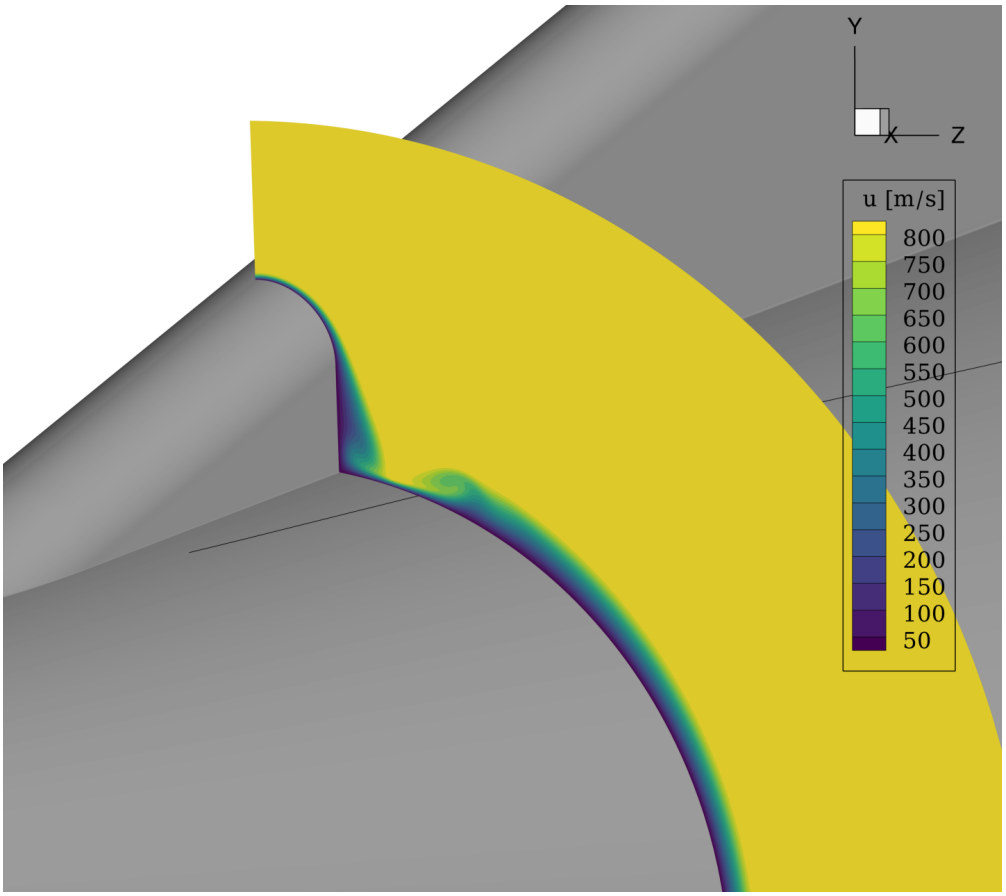

Figure 6.17: Basic-state $\bar{u}_C$ at $X = 0.150$ m. The vortex path is shown as the black line on the surface of the cone.

reaching from the wall to the boundary-layer edge. Also, the perturbation has a noticeable spread both into the fin vortex, as well as extending toward the larger cone boundary layer away from the fin. In figure 6.19e, 194 kHz is the dividing point between seemingly two different regions of the instability. $\left|\check{\hat{u}}_N\right|$ has a similar footprint as in 6.19a, but rotated counter-clockwise. The strongest region stays in the same high-shear region, which is true across the other two higher frequencies shown as well. $|\hat{p}|$ displays a larger change, beginning to extend to the top of the vortex as well as the left side. At $f = 252$ kHz, the pressure perturbation begins to separate from the wall and is mostly concentrated at the top of the vortex. The perturbation has also withdrawn from the fin boundary layer at the levels shown. This is consistent with a general trend, namely that the instabilities with a tighter spatial distribution tend to be more unstable. At 360 kHz, the velocity

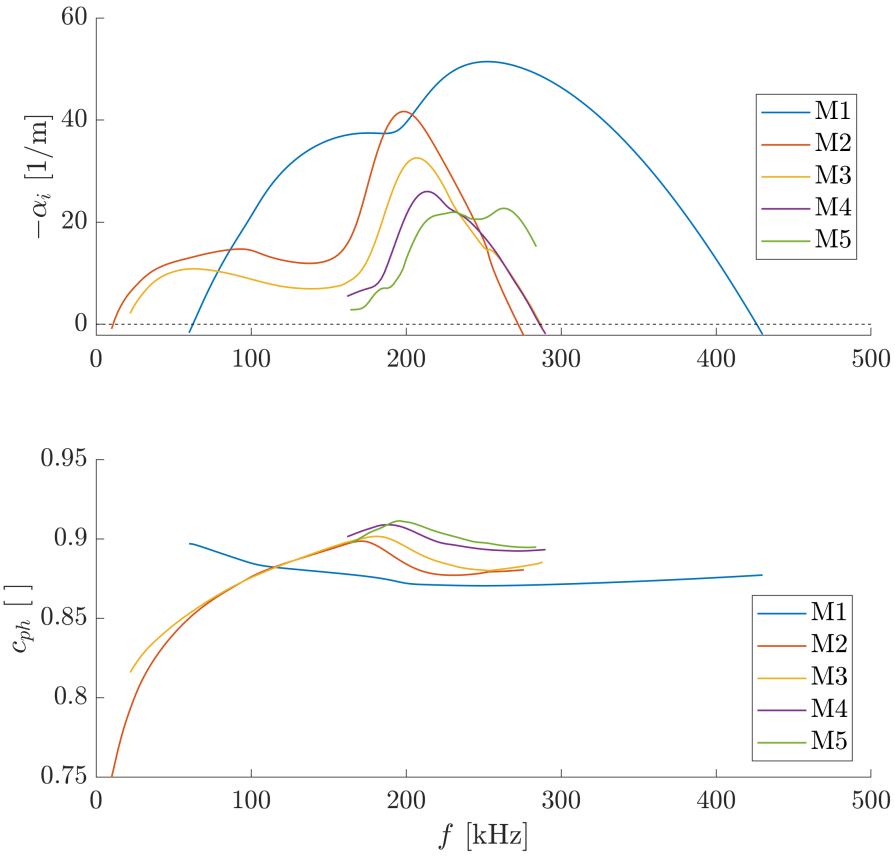

Figure 6.18: Modes present at $X = 0.150$ m as a function of frequency.

eigenfunction has shifted more to the left of the vortex, and the band opposite the center of rotation of the vortex has mostly disappeared. This frequency also sees $|\hat{p}|$ largely concentrated at the top of the vortex. It would seem that this shift in the pressure component of the instability correlates the best with the shift in behavior of α_i.

Mode 2 is also sampled at specific frequencies, denoted by black x's in figures 6.21. Velocity perturbations in the streamwise direction are shown in figures 6.22, and figures 6.23 have the corresponding pressure perturbations, in the same manner as was done for Mode 1. At 50 kHz, $\left|\check{\hat{u}}_N\right|$ has more of a teardrop shape than any modes seen thus far. The widening of the concentrated area appears to be related to the fact that it sits at boundary between the vortex and the more-2-D boundary layer away from the fin. The mass-flux lines in that region grow further apart slightly,

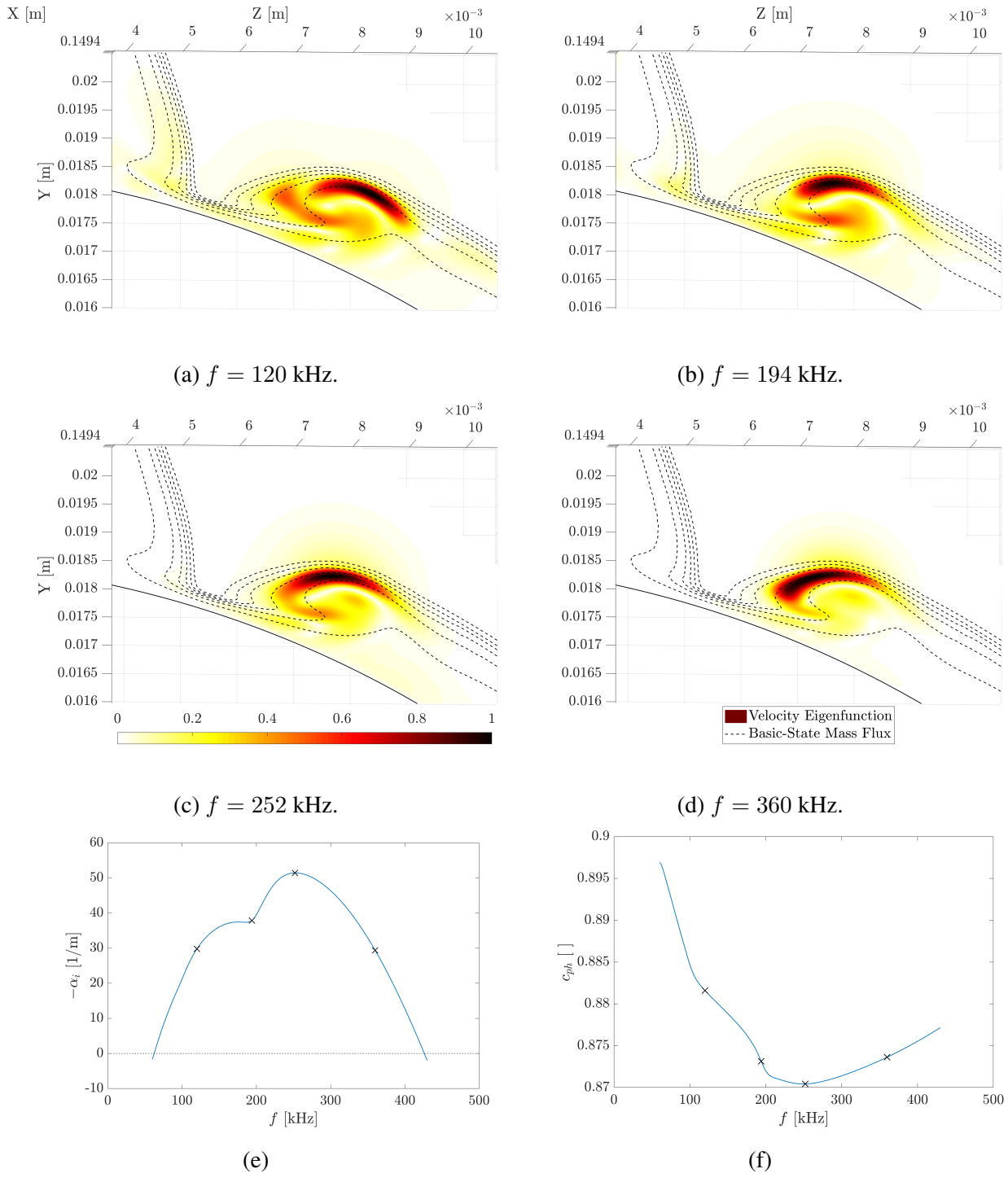

(a) $f = 120$ kHz.

(b) $f = 194$ kHz.

(c) $f = 252$ kHz.

(d) $f = 360$ kHz.

(e)

(f)

Figure 6.19: Figures a–d show the progression of Mode 1 with frequency. The color map is $\left|\check{\hat{u}}_N\right| / \max\left|\check{\hat{u}}_N\right|$ and the dashed black lines are contours of $\bar{\rho}\bar{u}_C$. Figures e and f show the growth rate and phase speed of Mode 1, respectively. The black x's mark the frequency locations of figures a–d.

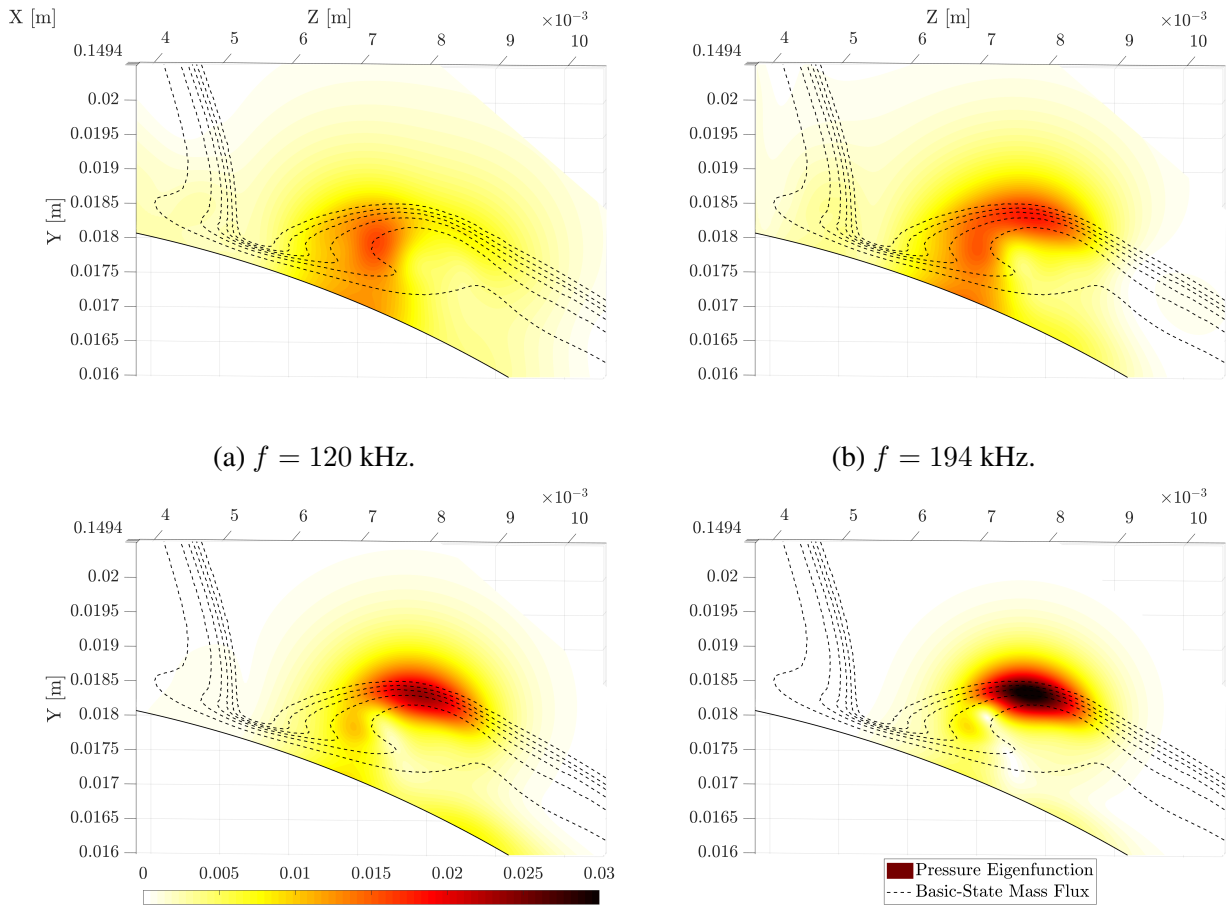

(a) $f = 120$ kHz.

(b) $f = 194$ kHz.

(c) $f = 252$ kHz.

(d) $f = 360$ kHz.

Figure 6.20: Figures a–d show the progression of Mode 1 with frequency. The color map is $|\hat{p}| \,/\, \max\left|\tilde{\hat{u}}_N\right|$ and the dashed black lines are contours of $\bar{\rho}\bar{u}_C$.

spreading out the velocity perturbation with it. The pressure eigenfunction at this frequency has a peak inside the vortex and outside the vortex, both relatively high in the boundary layer. It should be noted that the color scale had to be changed for figure 6.23a relative to the rest of the frequencies for Mode 2, as $|\hat{p}| \,/\, \max \left|\check{\hat{u}}_N\right|$ is an order of magnitude smaller. Figure 6.22b shows that at 100 kHz the velocity perturbation has moved back toward the center of the vortex. It appears similar to Mode 1 at 120 kHz in that a second peak appears lower in the vortex. The pressure signature is also sitting at the left side of the rollover, like in Mode 1. 140 kHz shows $\left|\check{\hat{u}}_N\right|$ developing a third peak near the wall as $|\hat{p}|$ grows stronger. At the most unstable frequency for Mode 2, the pressure signature changes significantly. The peak on the left of the vortex follows the edge of the vortex around to the top, and a second strong peak is seen at the wall in the quasi-2-D region. The velocity perturbation extends out of the vortex, but is still mainly concentrated in two bands within the vortex. By 240 kHz, the perturbation has mostly receded back into the vortex and the pressure peak at the wall has weakened substantially.

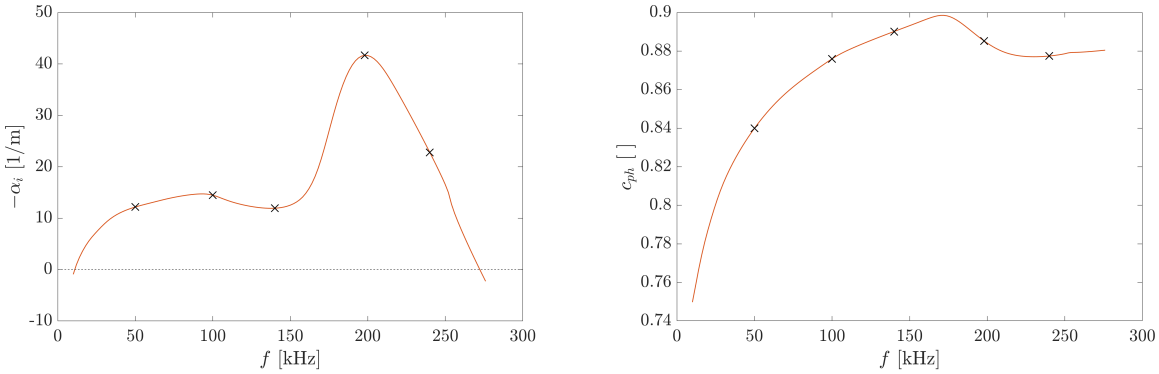

(a) (b)

Figure 6.21: Figures a and b show the growth rate and phase speed of Mode 2, respectively. The black x's mark the frequency locations of figures 6.22 and 6.23.

Modes 1 and 2 are difficult to categorize, as their eigenfunctions confirm that their characteristics do change with frequency, as opposed to simply shifting in the boundary layer. One of the main differences with this geometry with respect to other streamwise vortices that have

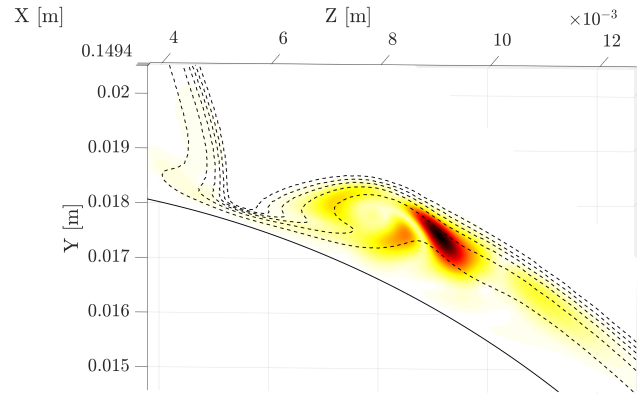

(a) $f = 50$ kHz.

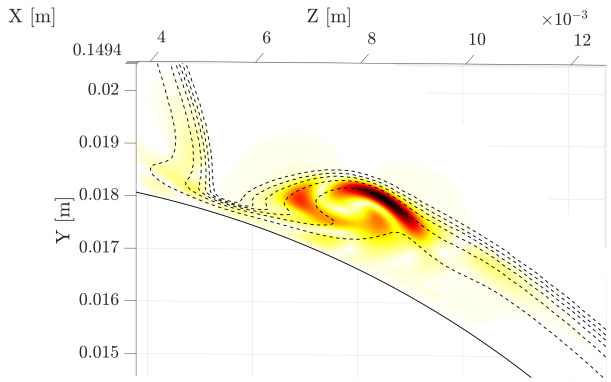

(b) $f = 100$ kHz.

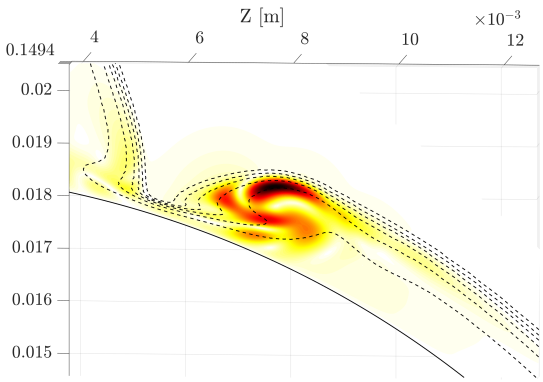

(c) $f = 140$ kHz.

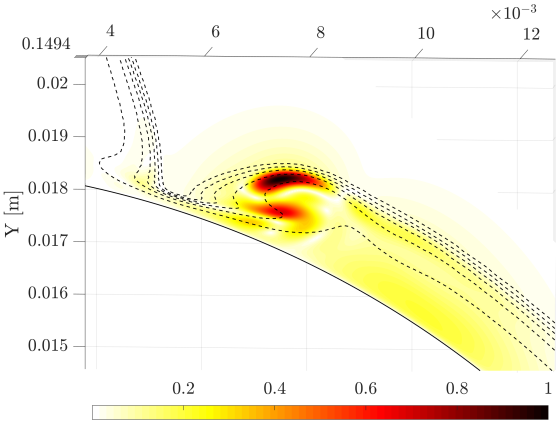

(d) $f = 198$ kHz.

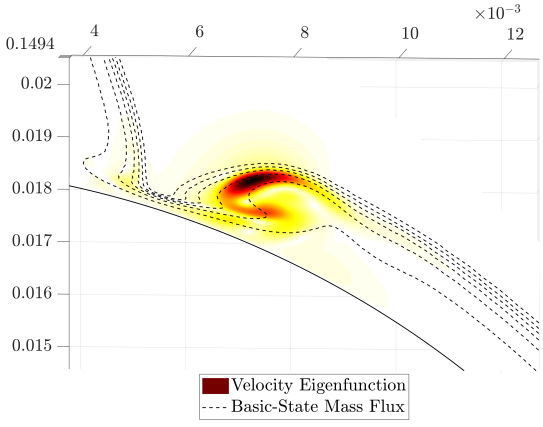

(e) $f = 240$ kHz.

Figure 6.22: Progression of Mode 2 with frequency. The color map is $\left|\check{\hat{u}}_N\right| / \max \left|\check{\hat{u}}_N\right|$ and the dashed black lines are contours of $\bar{\rho}\bar{u}_C$.

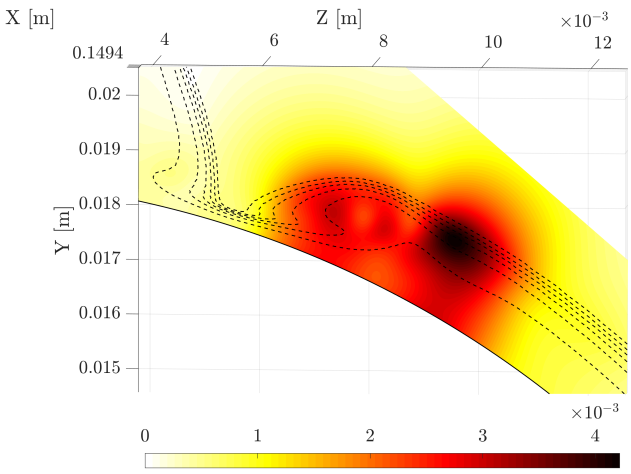

(a) $f = 50$ kHz.

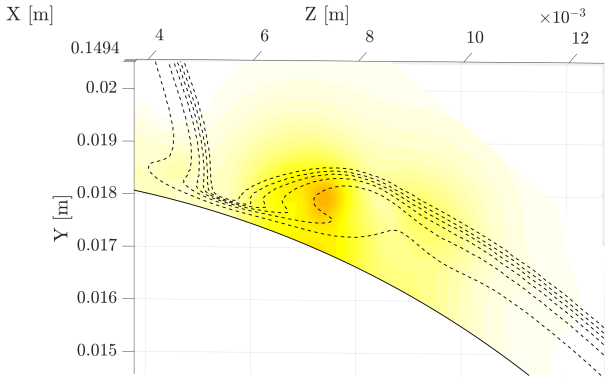

(b) $f = 100$ kHz.

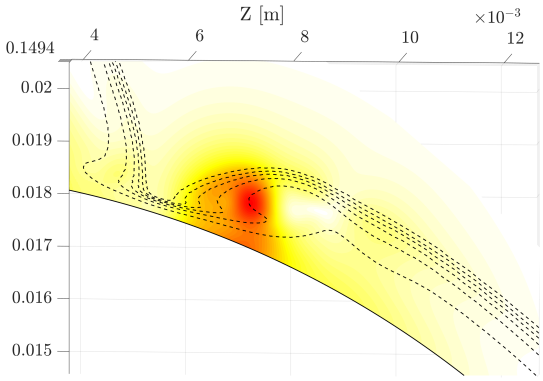

(c) $f = 140$ kHz.

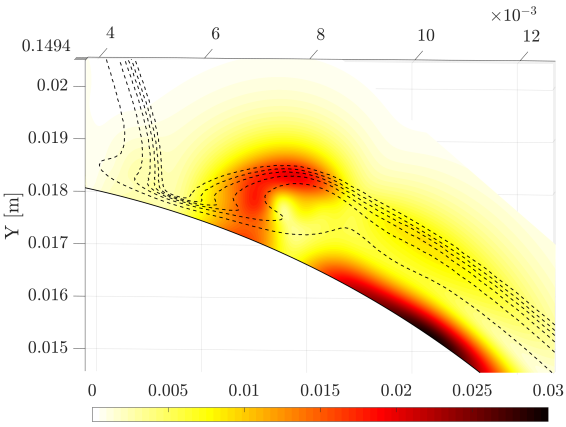

(d) $f = 198$ kHz.

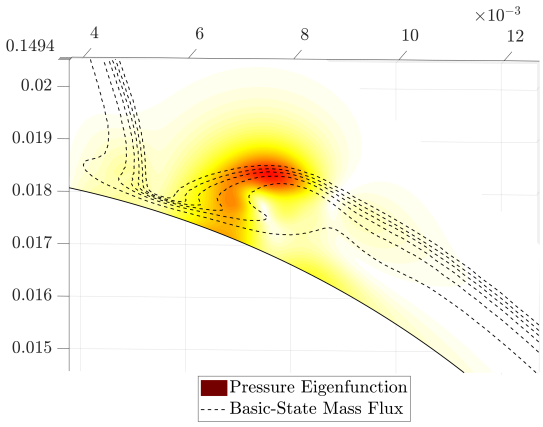

(e) $f = 240$ kHz.

Figure 6.23: Progression of Mode 2 with frequency. The color map is $|\hat{p}| \,/\, \max\left|\check{\hat{u}}_N\right|$ and the dashed black lines are contours of $\bar{\rho}\bar{u}_C$. The color scale under figure a only applies to that figure; the color scale under figure d applies to figures b–e.

been analyzed in previous literature is that these vortices have a distinct origin. Analyses of the yawed-cone [26, 28, 29], HIFiRE-5b [30], and HyTRV [34] configurations all had the benefit of tracking the vortices upstream to an undisturbed region of the flow, allowing for the identification of distorted second-mode and traveling crossflow-instabilities, for instance. Here, the vortex originates from the intersection of the fin and the cone, a very three-dimensional region with shock-boundary-layer interactions present as well. A more general tool than spatial BiGlobal is necessary to analyze that region. As a result, comparison with classical quasi-2-D boundary-layer instabilities is limited. Mode 1 at $f = 360$ kHz seems a likely candidate for a Type-II instability, as the streamwise-velocity perturbation is concentrated where wall-normal shear is high, and the pressure signature is also focused in that region. At the rest of the frequencies, Mode 1 does not fit nicely into well-known secondary- or distorted-primary-instability bins. Regarding Mode 2, the behavior of α_i in figure 6.21a resembles the figure 4b in Choudhari et al. [29]. The instability plotted in dashed green in this figure has the same two-parabola behavior. They note that their mode changes from resembling a distorted second mode from 140–250 kHz, and then switches to behave as a shear-dominated instability beyond 250 kHz. If this applies to Mode 2, then that would imply that it is second-mode-like between 150 and 275 kHz, and Type-I/II-like between 10 and 150 kHz. The strongest support for this theory comes from the strong pressure signature at the wall at $f = 198$ kHz, characteristic of distorted second modes. However, $\left|\check{\tilde{u}}_N\right|$ is somewhat different than what other researchers report these modes to look like [26, 28, 29], so this characterization is not definitive. A possible solution is to look at the distribution of perturbation energy. Categorizing which terms were contributing to the "energy budget" was what helped Malik et al. identify Type-I and -II modes [14]. More recently, Groot applied the idea to incompressible SBG solutions of crossflow vortices, and expanded on a number of the most-important terms [86]. Riha et al. applied this concept to compressible SBG in a limited manner on crossflow vortices on the HIFiRE-5b vehicle [87]. Patel also gave the full budget equations for compressible PSE, and demonstrated its use on a transonic swept wing [88]. Detailing the budget equations in full for compressible SBG would provide an extra tool to help categorize these instabilities.

6.3.2 Integrated Growth Results

Analyzing the locally most-unstable modes is only a part of the picture. In order to understand transition behavior at a certain point in the flow, instabilities must be integrated from upstream. Detailed pressure-fluctuation data is available at $Re' = 5.9 \times 10^6$ m^{-1} in Turbeville [72]. The results span $X = 0.258$–0.376 m on the cone, with multiple axial and azimuthal locations provided. In order to find the most-amplified mode computationally, eigenvalue computations were performed at multiple X locations. One of the more important locations for integration purposes is $X = 0.282$ m, shown in figure 6.24. As with $X = 0.150$ m, there are multiple unstable modes at a given location. After marching various modes upstream and downstream, Mode 6 was found to be the most amplified. It is also the mode that was used as a test instability throughout section 6.2. The results of the marched solutions are shown below.

Figure 6.25 shows the nondimensional phase speed and dimensional growth rate. c_{ph} is nondimensionalized by the freestream velocity outside the cone shock. Frequencies range from 100 kHz—the darkest color—to 390 kHz—the lightest color—in 10 kHz increments. When marching Mode 6 downstream, most frequencies converged quite easily unless the modes became stable. Stable modes are extremely difficult to converge with SBG (and LST). When marching the solution upstream, for frequencies from 100–240 kHz, all of the modes diverged within a few millimeters of $X = 0.211$ m. However, for frequencies from 250–390 kHz, the solutions successfully marched through this region, all the way to the furthest-upstream SBG surface at $X = 0.137$ meters from the nose. By $X = 0.150$, Mode 6 has smoothly merged with Mode 1, indicating that these are likely the same instability.

The fact that, starting from the same instability, some frequencies pass through $X = 0.211$ m and some do not is a curious one. Figure 6.25b shows a possible explanation. Near $X = 0.200$ m, the frequencies that smoothly pass this region are at a local minimum in growth rate. All frequencies have $-\alpha_i < 10$ 1/m, and the highest frequencies are even stable. For $f \leq 240$ kHz, their growth rates are similarly tracking downward. Three theories seem plausible to explain this. First, the two frequency bands could be tracking different features of the vortex, causing

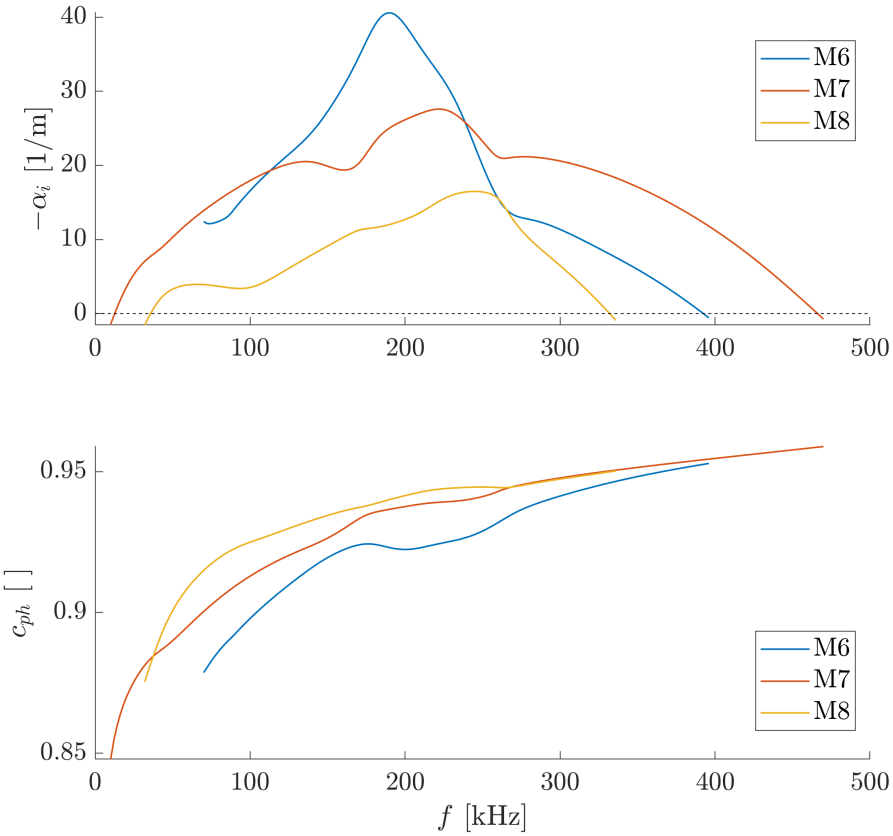

Figure 6.24: Modes present at $X = 0.282$ m as a function of frequency.

them to behave differently as the vortex evolves downstream. This would imply that while at $X = 0.282$ m Mode 6 is seen to smoothly vary through the frequency range, the eigenfunctions diverge enough that they are activated by different mechanisms. Another possibility is that the lower-frequency band has a two-maxima behavior for growth rate in X, similar to the upper-frequency band, but the minimum is so stable that SBG is unable to march through that region. A third hypothesis is that there are many similar eigenfunctions to Mode 6 for the lower-frequency band near $X = 0.200$ m. In other words, the problem could be numerical, instead of physical. This could cause the observed diverging behavior, and could potentially be rectified with careful application of the available numerical techniques in BLAST. Using a smaller ω_{relax}, taking smaller steps in X or doing a series of eigenvalue problems to reinitialize the modes are possible ways to

improve the solution convergence. These options could be explored in future work if the other two explanations do not appear plausible. However, the eigenfunctions for particular frequencies are analyzed in later sections and it is determined that there are likely physics-based explanations for the lower-frequency band diverging.

If it is assumed that the truncation of the lower frequencies at $X = 0.211$ m is valid, then the N factors for the two frequency bands can be compared as in figure 6.26. Only $f = 350$–390 kHz reached their neutral points, so the other frequencies have only parts of their full amplification captured with SBG. With this in mind, useful information can still be gleaned by comparing the N factors over the X-domains available. The upper frequency band reaches a maximum N of 5.0 at $f = 250$ kHz and $X = 0.340$ m. As mentioned before, these modes achieve most of their amplification in two distinct regions: from about $X = 0.14$ to $X = 0.19$ m and from about 0.23–0.28 meters from the nose. It is worth noting that the 250 kHz mode is the most-amplified and most-unstable mode from the upper-frequency band essentially over the entire domain. The modes respect their relative position in which frequency is more unstable throughout most of the flowfield. On the other hand, the lower-frequency band of modes are constantly trading which mode is both locally most-unstable and most-amplified. From LST and PSE experience, this is a common feature of modes that are particularly tuned in to a length measure, like the boundary-layer height. For instance, see figures 7.11 and 7.12 regarding Tollmein–Schlichting and traveling-crossflow LPSE N factors by Beyak on a swept wing [89]. The lower frequencies achieve a maximum N factor at the last X station, 0.387 m, with $f = 180$ kHz achieving an N of 5.4. Since the neutral point was not reached, it should be noted that frequencies 160–200 are within a ΔN of 0.25, with the lower could become the most-amplified instability with extra amplification upstream of $X = 0.211$ m. Recall that very similar results were obtained in section 5.3 under Case-I conditions, even though different N factors are obtained with fairly different methodologies. This is believed to be the same instability as the one tracked in those results.

These results can be compared to experimental data from Turbeville [72]. For $Re' = 5.9 \times 10^6$ m^{-1}, he measures root-mean-square (RMS) pressure-fluctuation levels at just shy of 2% of

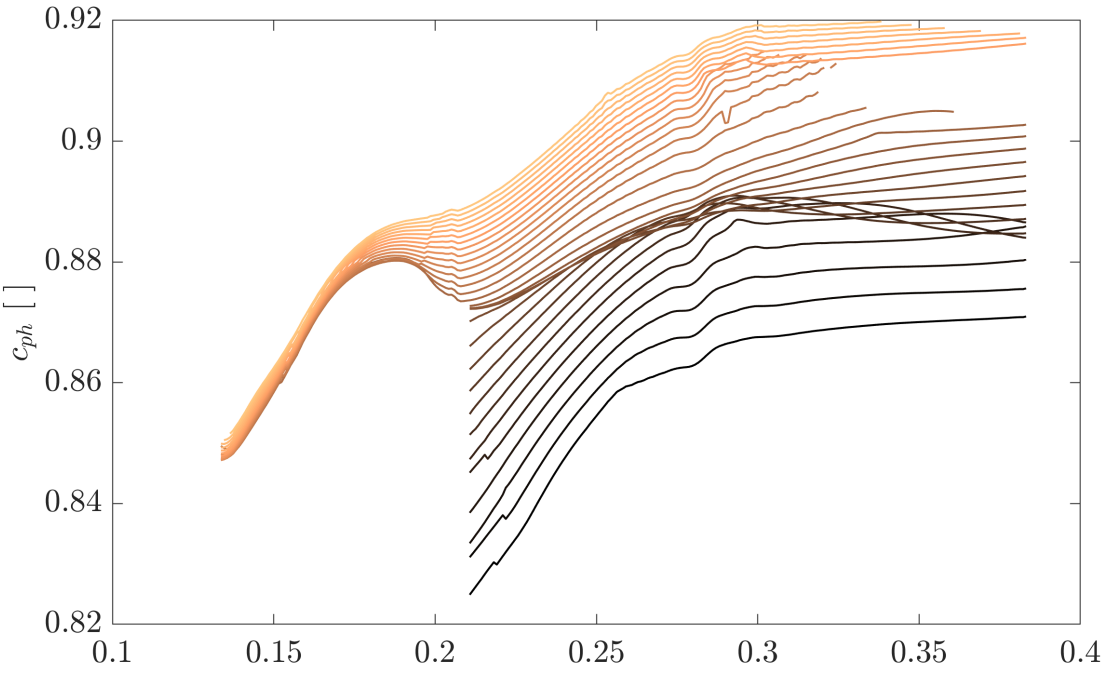

(a)

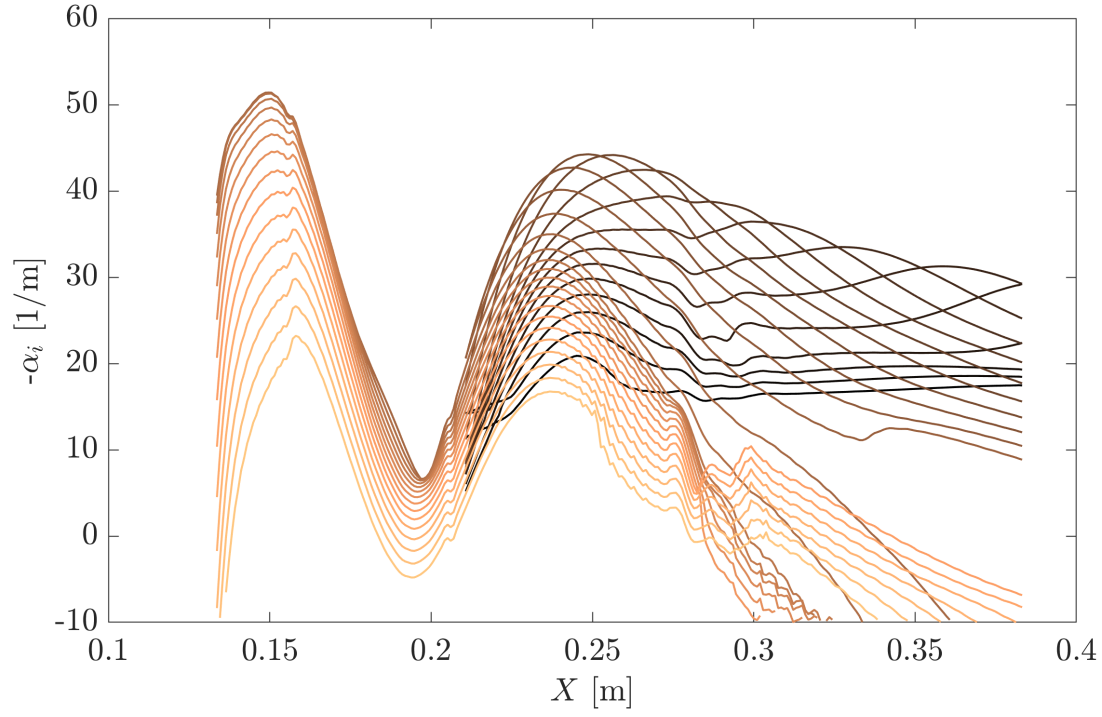

(b)

Figure 6.25: Phase speed (figure a) and growth rate (figure b) for Mode 6. There are two frequency bands: 100–240 kHz is calculated from $X = 0.211$–0.387 m and 250–390 kHz is calculated from $X = 0.137$–0.387 m. Frequencies increase from darker to lighter colors.

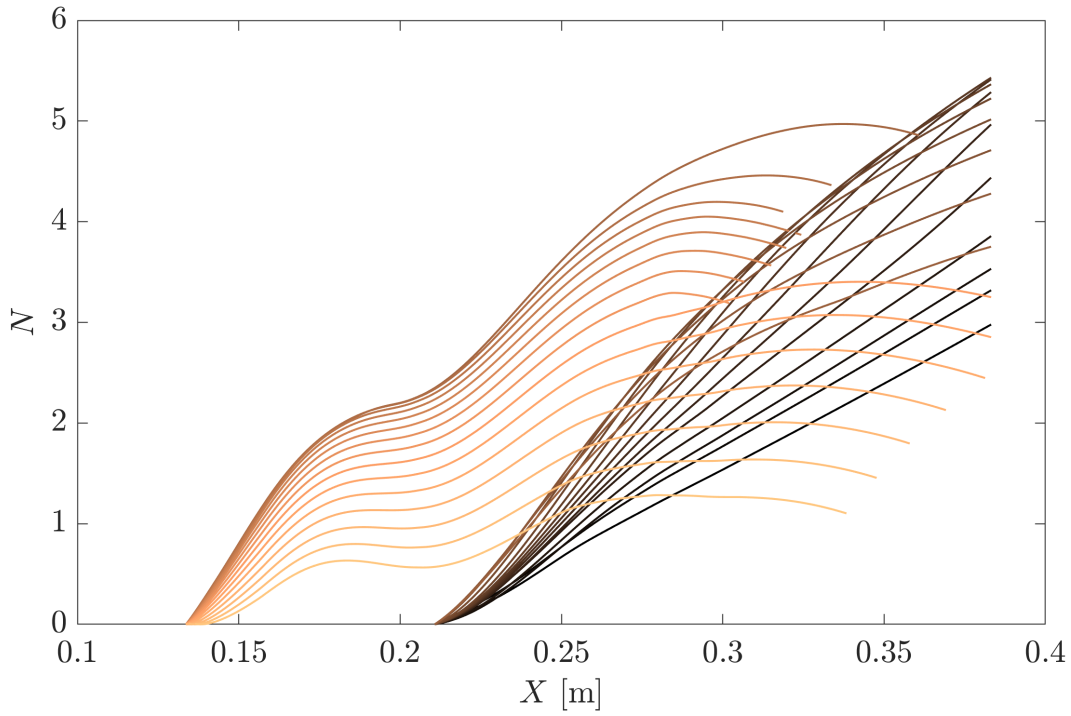

Figure 6.26: N factors for Mode 6. There are two frequency bands: 100–240 kHz is calculated from $X = 0.211$–0.387 m and 250–390 kHz is calculated from $X = 0.137$–0.387 m. Frequencies increase from darker to lighter colors.

the local wall pressure, with the azimuthal extent concentrated tightly in the vortex. Turbeville notes two main instabilities: one centered at 180 kHz and another at centered at 250 kHz. The higher frequency is detected first, and is strongest on the right side of the vortex (when looking downstream). At $X = 0.329$ m, it is observed that the 180 kHz mode begins to overtake the higher frequency, dominating the spectrum until transition onset. The lower frequency is also more prevalent on the middle-to-left side of the vortex. Figures 5.22 in the aforementioned work shows the Fourier transform of the pressure fluctuations at different axial and azimuthal locations. While the experiments covered in this work are of excellent quality and an invaluable resource for furthering the understanding of vortex-dominated transition, experimental runs at this particular Reynolds number were observed by Turbeville to have slightly higher variability in the hot-streak location as detected by infrared cameras. A combination of potential flexing in the fin and the

effective sensing area of the pressure sensors combine to provide an uncertainty in the azimuthal location of the streak relative to the sensor of up to 3–4 degrees. As a result, the angles provided for each azimuthal measurement of the vortex pressure spectra are of limited value, and the figures and contained spectra must be read as a whole.

The N factors discussed above strongly support the interpretation of the experimental data by Turbeville [72]. In figure 6.26, 250 kHz grows first, then 180 grows faster at the back of the cone and overtakes the higher frequency. There is no way to reproduce the azimuthal variation of amplification that is detected Turbeville's experiments with spatial BiGlobal, as α is constant across the domain and $|\hat{p}|$ cannot be compared between different frequencies or X stations. However, a plot similar to Turbeville's figures 5.22 can be created with N factors from SBG, just without the azimuthal variation. Figure 6.27 shows N vs f at the different X stations measured by Turbeville. Overall, direct comparison of instability amplification does not match the experiments well; the experiments detect much stronger amplification over the measured distance. However, this is a well-known property of parallel or quasi-parallel methods: they under-predict total growth compared to experiments, DNS computations, or even PSE results [7, 29]. The effects of nonparallelism in boundary layers are important for accurate prediction of instability growth. However, what quasi-parallel methods do usually predict correctly are the most-amplified frequencies, which is the case here. In addition, SBG predicts the 250 kHz mode becoming stable at around $X = 0.34$ m, which is also supported by the experiments detecting either a small increase or decrease in amplitude between $X = 0.329$ and 0.353 m, depending on the azimuthal location. So overall, the SBG computations agree well in comparison with Turbeville [72] in the categories expected of the method.

6.3.2.1 180 kHz Mode

To learn more about the $f = 180$ kHz mode, certain X locations are chosen to display its eigenfunction. In figure 6.28, 6 red x's are placed based on changes in the growth rate, as well as the first and last solutions in X. These correspond to the locations shown in Figures 6.29. In this set of figures, each row is a single ξ domain, the left column's color map is $\left|\check{\tilde{u}}_N\right| / \max\left|\check{\tilde{u}}_N\right|$, the

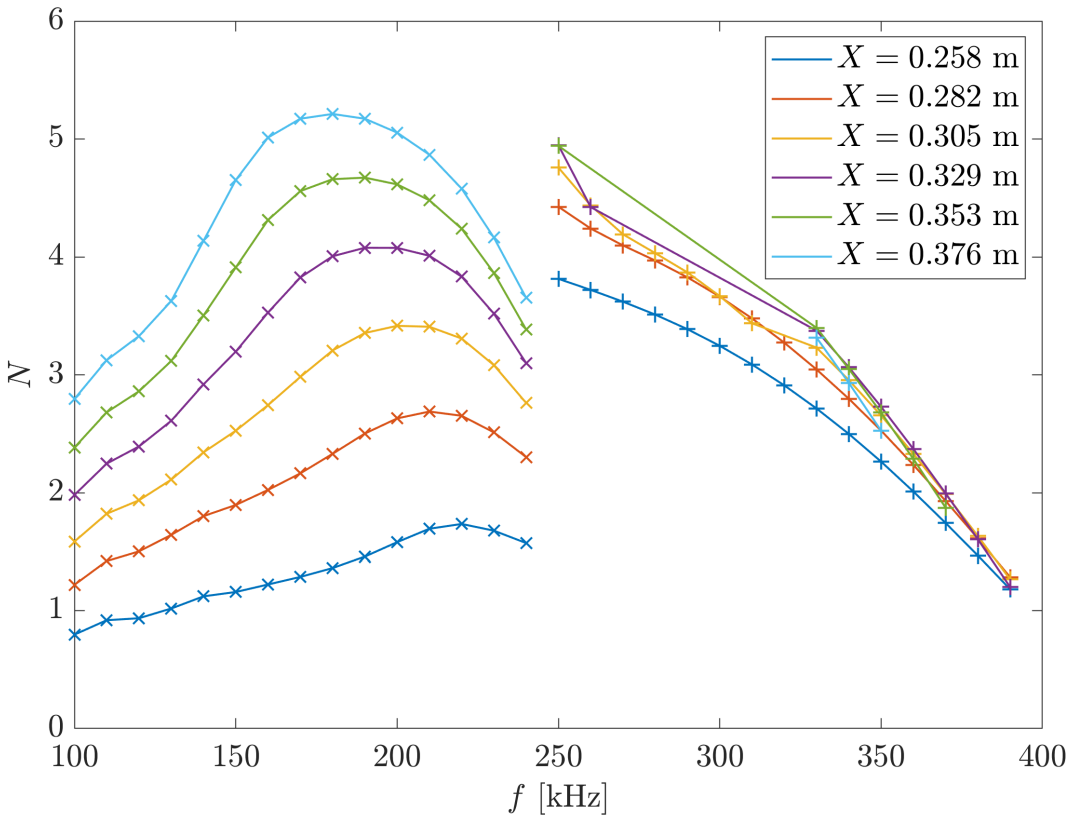

Figure 6.27: N factor versus frequency for Mode 6 at different X locations. The 'x' markers are the lower-frequency band and the '+' markers are the upper-frequency band. Locations correspond to pressure measurements in Turbeville [72].

right column's is $|\hat{p}| \,/\, \max \left|\check{\hat{u}}_N\right|$, and the dashed black lines are again $\bar{\rho}\bar{u}_C$.

Figures 6.29a and 6.29b show the most upstream solution for $f = 180$ kHz. Here, the mode appears most like a Type-II instability. $\left|\check{\hat{u}}_N\right|$ is concentrated at the top of the vortex, and there is a significant pressure signature there as well, although there is another weak local maximum in $|\hat{p}|$ at the wall. At $X = 0.246$ m, $-\alpha_i$ has nearly reached its peak and is transitioning between two different regimes of growth. This transition is also represented in figures 6.29c and 6.29d. $|\hat{p}|$ has begun to shift to the wall, which is now the location of its maximum. $\max |\hat{p}| \,/\, \max \left|\check{\hat{u}}_N\right|$ has also increased three times relative to $X = 0.211$ m. The velocity perturbation is still mostly at the top of the vortex, but a region within the vortex close to the wall is starting to grow. The next X station, 0.276 m, is this frequency's most-unstable location over the length of the cone. Figure 6.29f shows

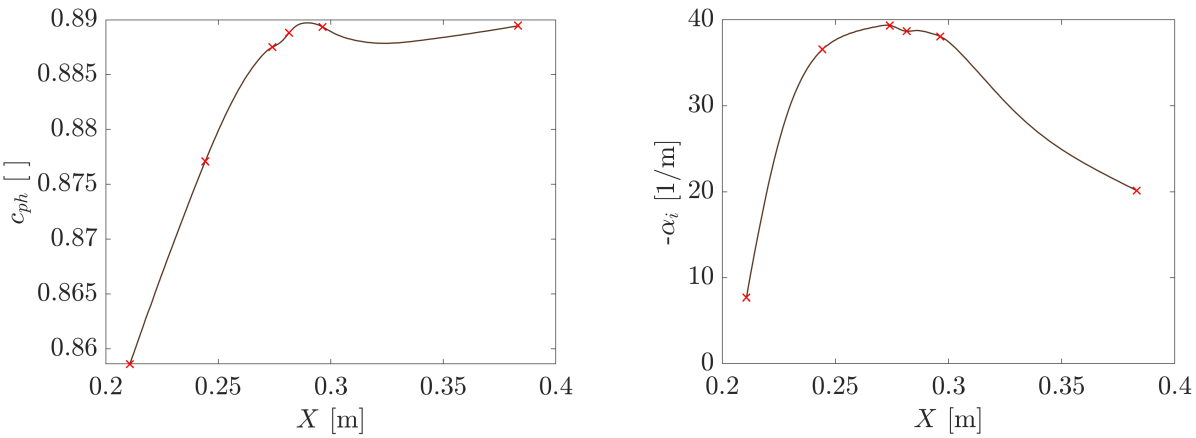

(a) (b)

Figure 6.28: Phase speed and growth rate versus X for $f = 180$ kHz. The red x's correspond to the locations shown in figure 6.29.

that pressure is now primarily concentrated at the wall, and again has roughly tripled in magnitude relative to $\max\left|\check{\hat{u}}_N\right|$. A peak near the wall in figure 6.29e is now fully formed. At this point, this instability resembles a distorted second mode more than the Type-II instability. Perturbations have been observed to resemble both of these instability types before, for instance in Moyes et al. [26]. At $X = 281$ m, there is a dip in the growth rate in figure 6.28b, but there does not seem to be an obvious change in figures 6.29g or 6.29h. The biggest change is a slight increase in the relative magnitude of the peak in $\left|\check{\hat{u}}_N\right|$, a trend that continues to $X = 0.299$ m. From here, the instability slows its growth all the way to the back of the cone. The final X location is shown in figures 6.29k and 6.29k. The same general structure of $\left|\check{\hat{u}}_N\right|$ and $|\hat{p}|$ is still there, but they both appear more distorted relative to $X = 0.299$ m, especially near the wall.

At $X = 0.299$ m, $f = 180$ kHz is the locally most-unstable mode across all frequencies. For the lower-frequency band, if the mode shapes are checked for the locally most-unstable frequency beyond $X = 0.250$ m, the mode shapes look nearly identical. Those frequencies also correspond to the coalescence of curves seen in 6.25a. Since the vortex seems particularly receptive to this form, the full eigenfunction is shown in figures 6.30. $\left|\check{\hat{u}}_N\right|$ and $|\hat{p}|$ have already been described with figures 6.29i and 6.29j, respectively. $\left|\check{\hat{v}}_N\right|$ in figure 6.30c has three major features. It has its

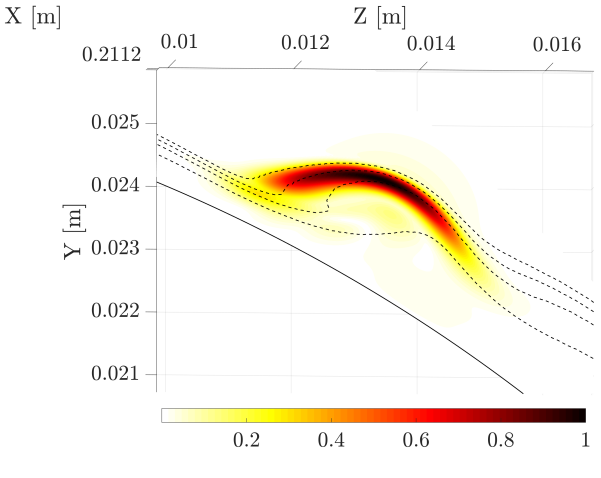

(a) $\left|\check{\hat{u}}_N\right| / \max\left|\check{\hat{u}}_N\right|$ at $X = 0.211$ m.

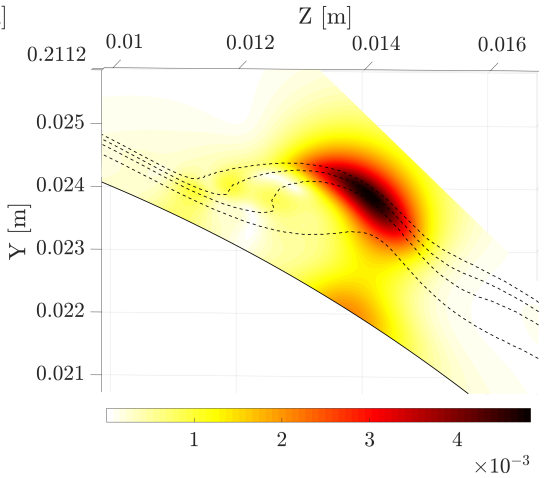

(b) $|\hat{p}| / \max\left|\check{\hat{u}}_N\right|$ at $X = 0.211$ m.

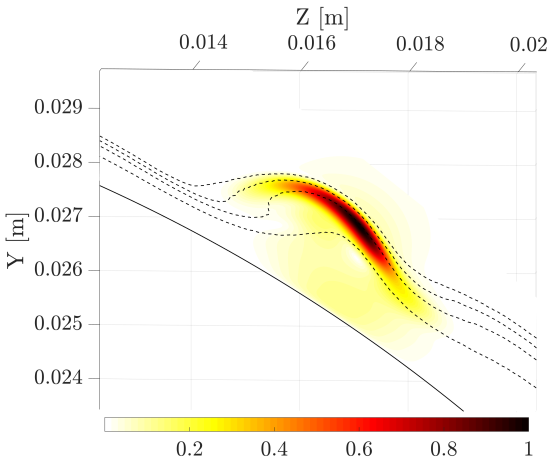

(c) $\left|\check{\hat{u}}_N\right| / \max\left|\check{\hat{u}}_N\right|$ at $X = 0.246$ m.

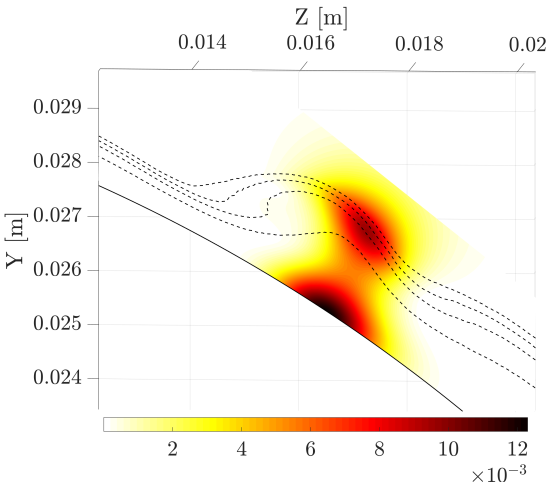

(d) $|\hat{p}| / \max\left|\check{\hat{u}}_N\right|$ at $X = 0.246$ m.

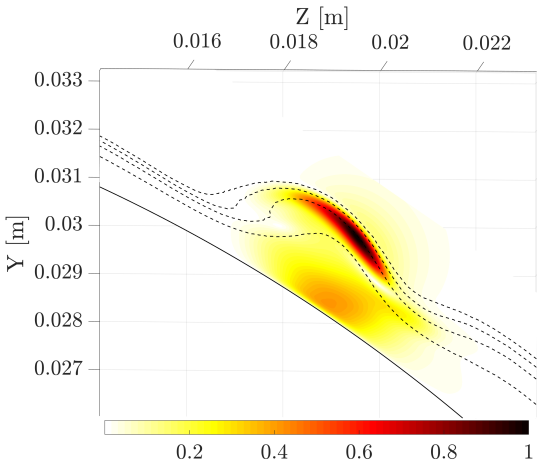

(e) $\left|\check{\hat{u}}_N\right| / \max\left|\check{\hat{u}}_N\right|$ at $X = 0.276$ m.

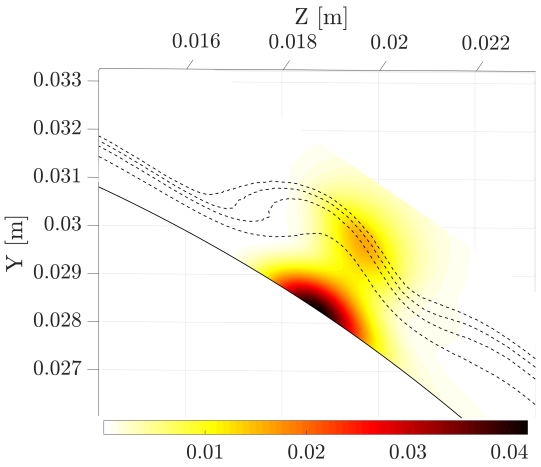

(f) $|\hat{p}| / \max\left|\check{\hat{u}}_N\right|$ at $X = 0.276$ m.

Figure 6.29: Eigenfunctions for $f = 180$ kHz from $X = 0.211$–0.387 m.

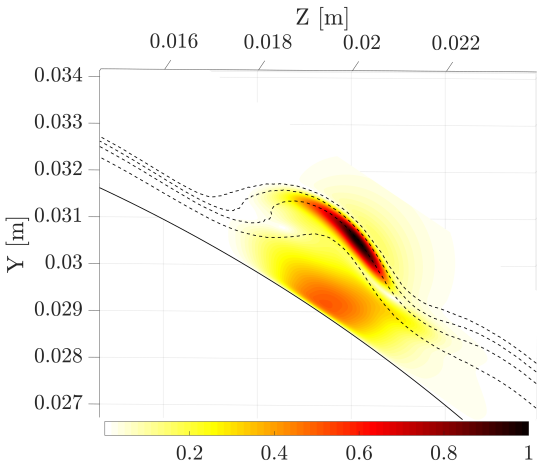

(g) $\left|\check{\hat{u}}_N\right| / \max \left|\check{\hat{u}}_N\right|$ at $X = 0.283$ m.

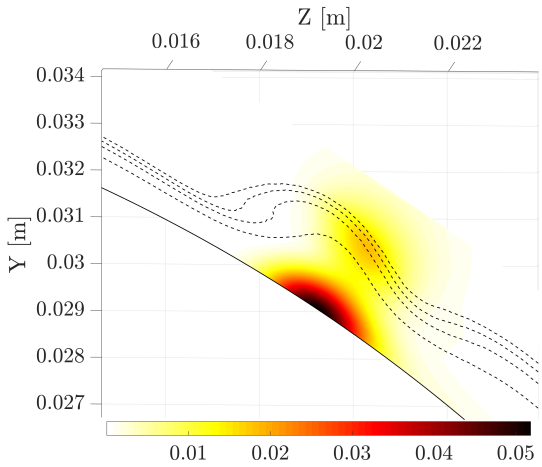

(h) $|\hat{p}| / \max \left|\check{\hat{u}}_N\right|$ at $X = 0.283$ m.

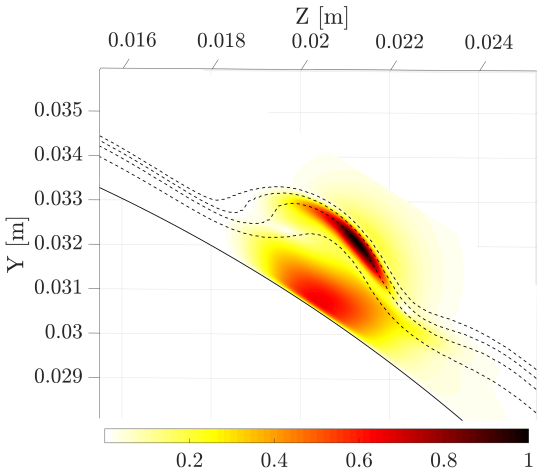

(i) $\left|\check{\hat{u}}_N\right| / \max \left|\check{\hat{u}}_N\right|$ at $X = 0.299$ m.

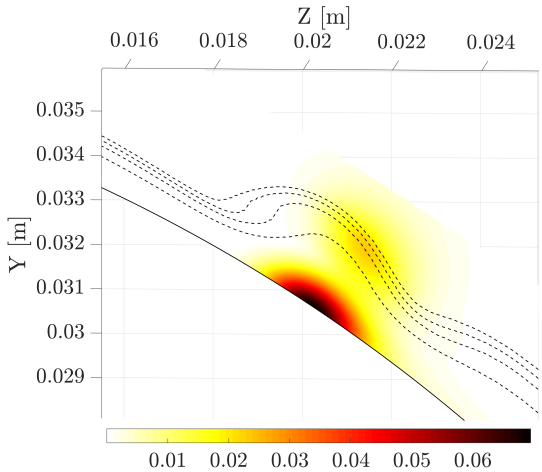

(j) $|\hat{p}| / \max \left|\check{\hat{u}}_N\right|$ at $X = 0.299$ m.

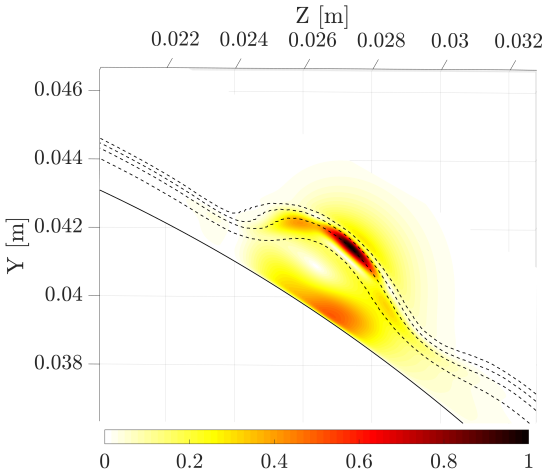

(k) $\left|\check{\hat{u}}_N\right| / \max \left|\check{\hat{u}}_N\right|$ at $X = 0.387$ m.

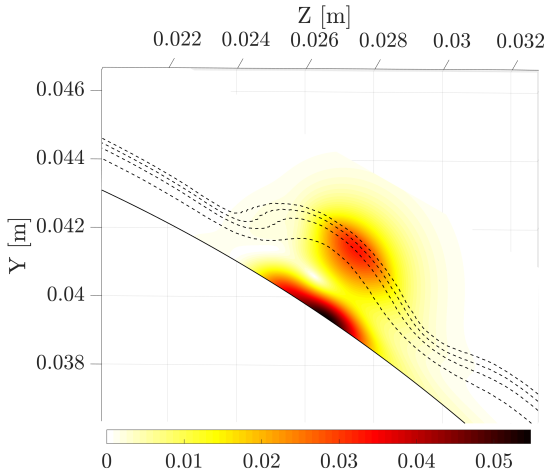

(l) $|\hat{p}| / \max \left|\check{\hat{u}}_N\right|$ at $X = 0.387$ m.

Figure 6.29: Eigenfunctions for $f = 180$ kHz from $X = 0.211$–0.387 m.

largest peak near the wall, centered in the uplift region of the vortex. Then, it has two weaker stretched peaks on either side of the high shear region near the shoulder of the vortex. Figure 6.30e shows that $\left|\check{\hat{w}}_N\right|$ also has peaks in the shoulder region and near the wall. The peaks in $\left|\check{\hat{w}}_N\right|$ seem to sit at the edges of the peaks in $\left|\check{\hat{v}}_N\right|$ in both locations in the vortex. Figures 6.30b and 6.30d have relatively benign shapes for $\left|\hat{T}\right|$ and $|\hat{\rho}|$, respectively, with both mode shapes concentrated on the shoulder of the vortex.

6.3.2.2 250 kHz Mode

For the 250 kHz mode, X locations are extracted from 0.137–0.318 m. The locations relative to the growth rate and phase speed are shown in figures 6.31. At the most upstream location, $X = 0.137$ m, the cone vortex is still tied to the fin vortex. The fin is actually visible in figures 6.32a and 6.32b at the very left edge of the figure, and both eigenfunctions extend all the way to the feature. Again, this underlines the importance of including the fin in the spatial BiGlobal domain in order to fully capture these instabilities. At this point, $\left|\check{\hat{u}}_N\right|$ has concentrations in the high-shear region at the top of the vortex and near its center of rotation. The $|\hat{p}|$ has a concentration at the top of the vortex as well, indicating that the instability is likely shear related at this location. The eigenfunctions are very similar to those shown in section 6.3.1, and in fact figures 6.32c and 6.32d are almost exactly the same mode as figures 6.19c and 6.20c, respectively. The only difference is 2 kHz: the modes are at 252 kHz in section 6.3.1 and 250 kHz here. By the time the vortex reaches $X = 0.175$ m, the vortex has moved farther away from the fin. It also appears to have been flattened on its top-left side relative to its previous form. The response of $\left|\check{\hat{u}}_N\right|$ to this change in shape is for the top peak to move further toward the boundary-layer edge while sliding more into the flattened region. The peak lower in the boundary layer has also been pulled toward the fin. The pressure perturbation increases in strength at the wall, but this feature is short-lived and reverses by $X = 0.198$ m. 0.198 meters from the nose is the location of a local minimum in growth rate for the 250 kHz mode. Here, it appears Type-II-like, with a single concentrated band of perturbation velocity near the top of the vortex, albeit shifted slightly left into the still-flattened region. $|\hat{p}|$ at the top of the vortex also supports the Type-II character. At $X = 0.238$ m, the growth rate

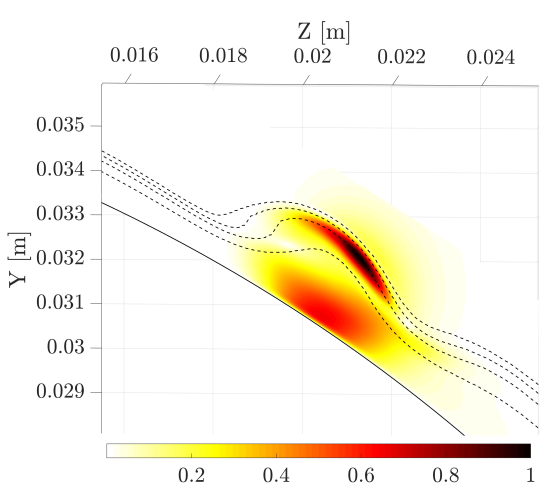

(a) $\left|\check{\tilde{u}}_N\right| / \max \left|\check{\tilde{u}}_N\right|$.

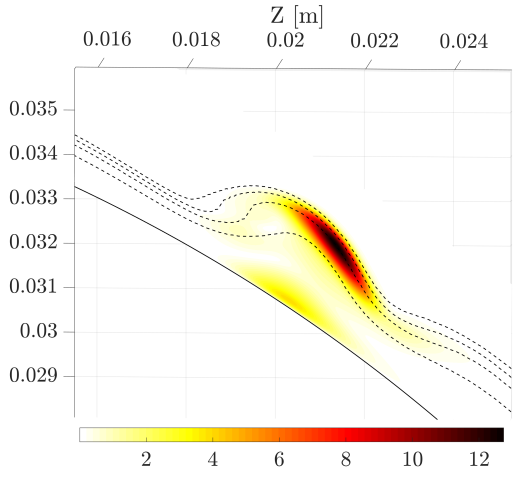

(b) $\left|\hat{T}\right| / \max \left|\check{\tilde{u}}_N\right|$.

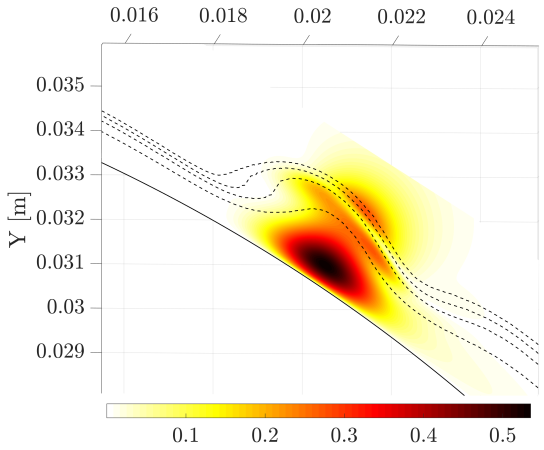

(c) $\left|\check{\tilde{v}}_N\right| / \max \left|\check{\tilde{u}}_N\right|$.

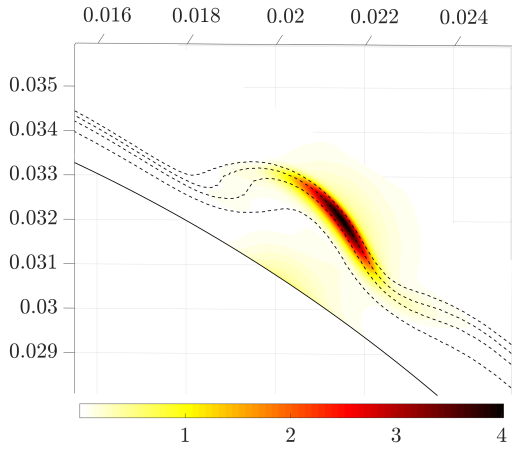

(d) $|\hat{\rho}| / \max \left|\check{\tilde{u}}_N\right|$.

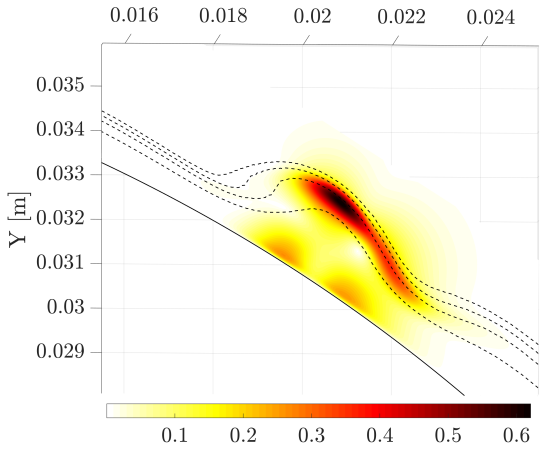

(e) $\left|\check{\tilde{w}}_N\right| / \max \left|\check{\tilde{u}}_N\right|$.

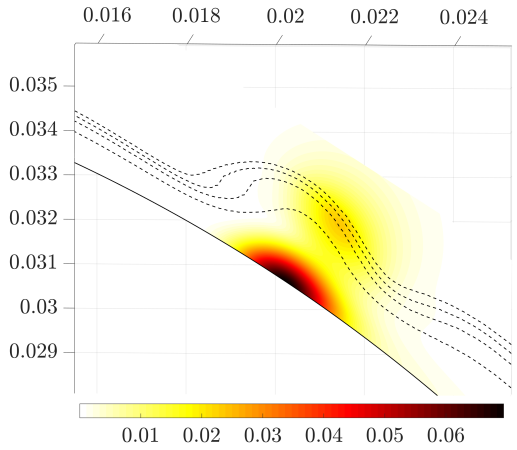

(f) $|\hat{p}| / \max \left|\check{\tilde{u}}_N\right|$.

Figure 6.30: Eigenfunctions for $f = 180$ kHz at $X = 0.299$ m.

hits another local maximum. The pressure and streamwise-velocity perturbation have increasing signatures near the wall, and both have shifted to the right. By the time the frequency has become stable near $X = 0.320$ m, the character of the instability has changed to resemble a second mode. The perturbation appears to tune in to a smaller region of the local boundary layer, both with $\left|\check{\hat{u}}_N\right|$ and $|\hat{p}|$ concentrated in this region.

The development of the 180 kHz and 250 kHz modes are not all that different. In the region around $X = 0.211$ where the lower-frequency band has difficulty converging, the mode shapes are similar. Comparing figures 6.32g and 6.32h ($f = 250$ kHz at $X = 0.198$ m) against figures 6.29a and 6.29b ($f = 180$ kHz at $X = 0.211$ m), both frequencies exhibit shear-dominated, Type-II characteristics. The main difference appears to be that the 250 kHz mode is shifted further left in the vortex, and is slightly more compact. Figures 6.32i–6.32j and 6.29c–6.29d both seem to show transition from a mode concentrated in the high-shear region of the vortex to one with a significant wall presence. At $X = 0.320$ m, the 250 kHz mode (figures 6.32k–6.32l) resembles a shifted version of the 180 kHz mode at $X = 0.299$ m (figures 6.29i–6.29j). Since the lower-frequency band has already been identified to be length-scale dependent in this region, it is no surprise that the higher-frequency 250 kHz mode would nest in a smaller part of the boundary layer. The similarity of the two frequencies' development supports the idea that these are the same instability that just tune in to different parts of the boundary layer. The character of the instability seems to evolve from shear-dominated or Type-II-like upstream to second-mode-like downstream. It also appears that the reason that the lower frequencies are difficult to converge in the ~ 0.2 m region is that they are driven by a slightly different part of the vortex that is weaker in that region.

The two-maxima behavior of the growth rate in X for the high-frequency modes is still a curious feature. It could be related to the change in character of the instability described earlier, but the modes seem to remain shear-related throughout the $X = 0.2$ m region. A possible explanation is offered, based on basic-state arguments. Looking at the mass-flux lines throughout figure 6.32, the vortex goes through a series of changes. At $X = 0.137$ m, the cone vortex is still attached to the fin boundary layer. The strong pressure gradients surrounding the fin-cone intersection

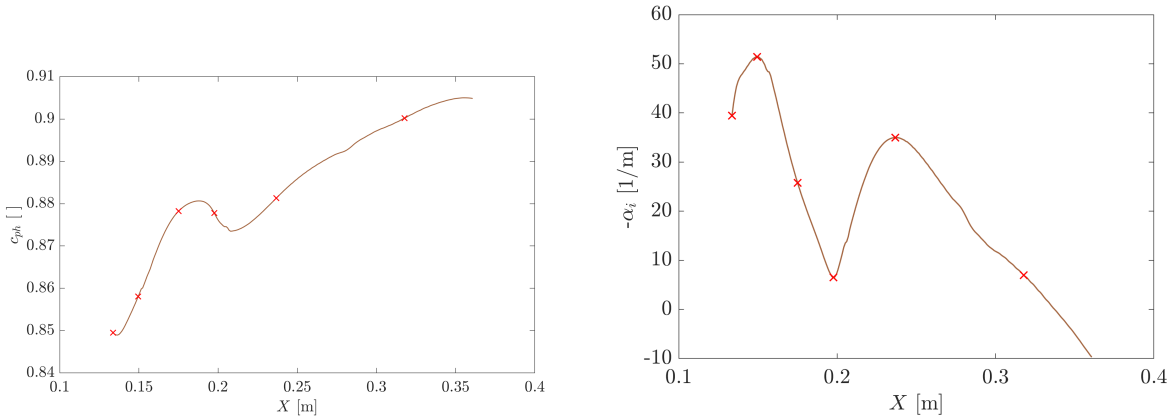

(a) (b)

Figure 6.31: Phase speed and growth rate versus X for $f = 250$ kHz. The red x's correspond to the locations shown in figure 6.32.

have resulted in vortex being fairly developed, with smooth curves visible around the edges of the boundary layer. At $X = 0.150$ m in figure 6.32c, the vortex separates from the fin boundary layer, with a very thin boundary layer on the cone in between the two. A pressure gradient caused by the presence of the fin pushes the cone vortex away, causing it to turn until roughly $X = 0.24$ m, as indicated in figure 6.4a. At that point, the pressure gradient has likely weakened to the point that it in equilibrium with the inertia of the boundary layer on the opposite side of the vortex. From $X = 0.150$–0.24, in figures 6.32c, 6.32e, 6.32g, and 6.32i, the vortex can be observed to have a slightly flattened top-left edge. This could imply that not only is the vortex being forced away from the fin azimuthally, but it is also being compressed toward the wall, changing how it evolves downstream. It was already noted previously that the 250 kHz mode responds to this basic-state feature. Starting at $X = 0.246$ m in figure 6.29c and beyond, the vortex returns to a more-gently curved boundary-layer edge in the region that was previously flattened. This coincides with the shift to second-mode-like behavior from the instability at both frequencies. After a short transition period, the modes display this behavior for the rest of the vortex' length. This theory could be further investigated in future work by analyzing pressure gradients around the vortex and its relative orientation to them. In addition, regions of wall-normal and spanwise shear could be

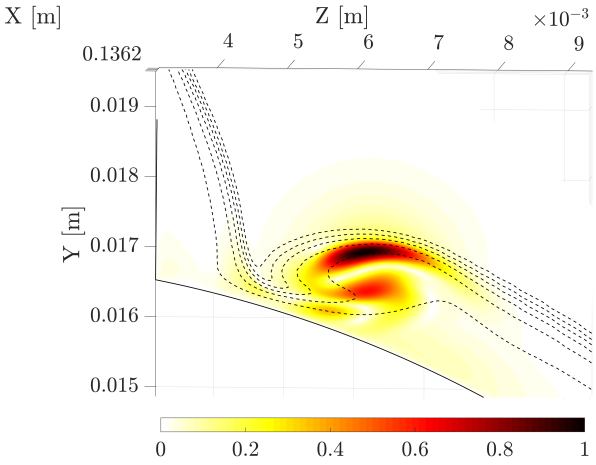

(a) $\left|\check{\hat{u}}_N\right| / \max\left|\check{\hat{u}}_N\right|$ at $X = 0.137$ m.

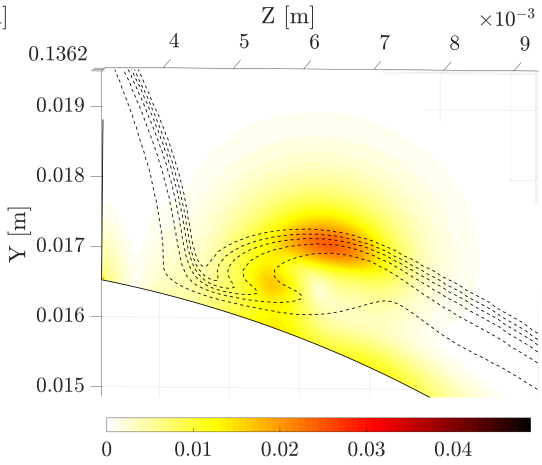

(b) $|\hat{p}| / \max\left|\check{\hat{u}}_N\right|$ at $X = 0.137$ m.

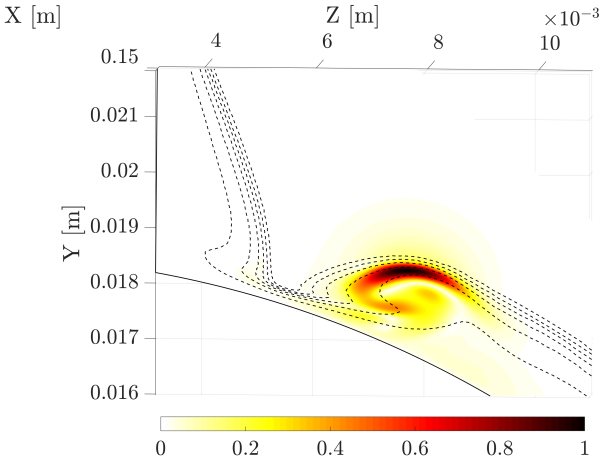

(c) $\left|\check{\hat{u}}_N\right| / \max\left|\check{\hat{u}}_N\right|$ at $X = 0.150$ m.

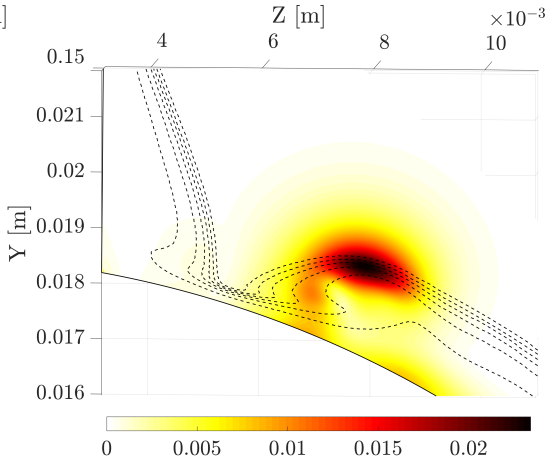

(d) $|\hat{p}| / \max\left|\check{\hat{u}}_N\right|$ at $X = 0.150$ m.

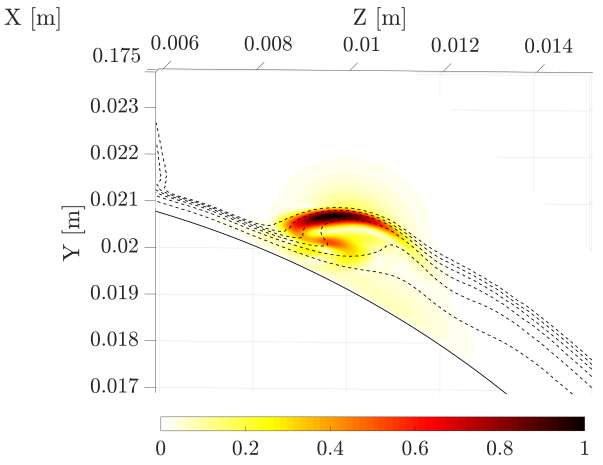

(e) $\left|\check{\hat{u}}_N\right| / \max\left|\check{\hat{u}}_N\right|$ at $X = 0.175$ m.

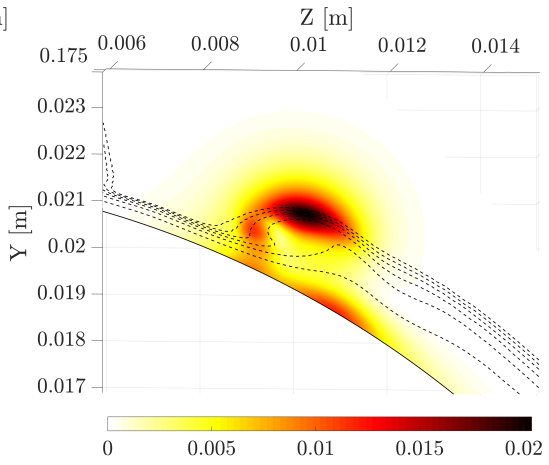

(f) $|\hat{p}| / \max\left|\check{\hat{u}}_N\right|$ at $X = 0.175$ m.

Figure 6.32: Eigenfunctions for $f = 250$ kHz from $X = 0.137$–0.320 m.

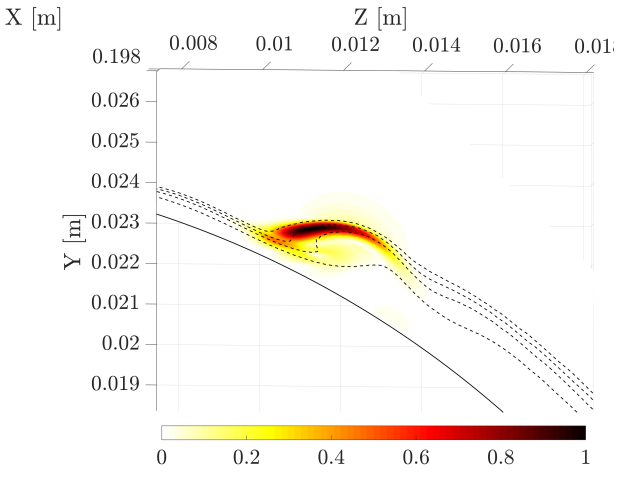

(g) $\left|\check{\hat{u}}_N\right| / \max \left|\check{\hat{u}}_N\right|$ at $X = 0.198$ m.

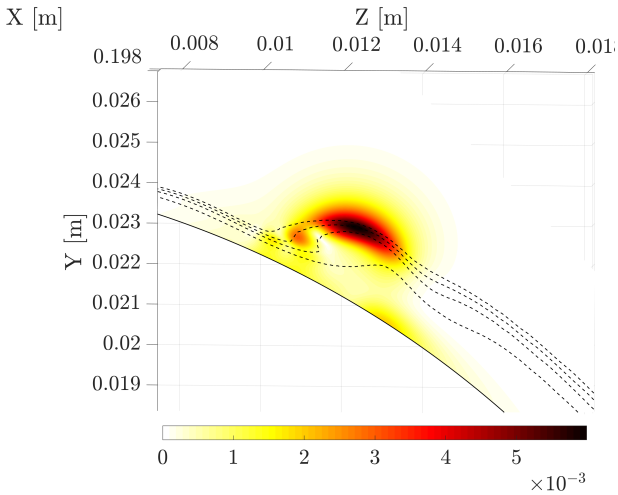

(h) $|\hat{p}| / \max \left|\check{\hat{u}}_N\right|$ at $X = 0.198$ m.

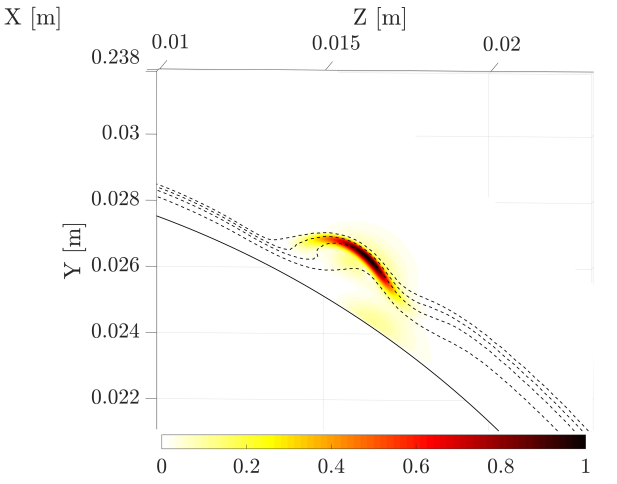

(i) $\left|\check{\hat{u}}_N\right| / \max \left|\check{\hat{u}}_N\right|$ at $X = 0.238$ m.

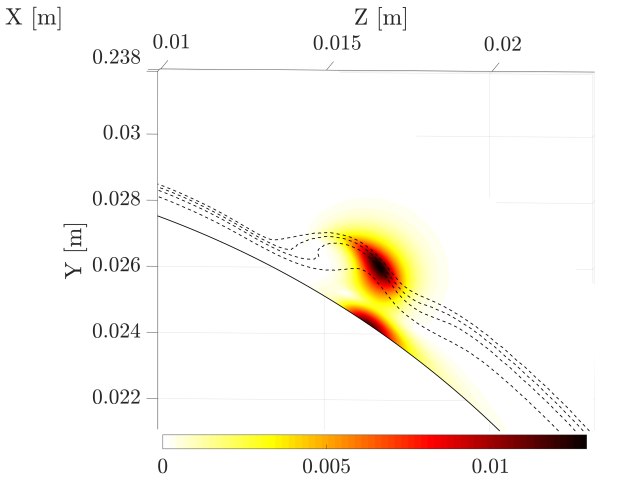

(j) $|\hat{p}| / \max \left|\check{\hat{u}}_N\right|$ at $X = 0.238$ m.

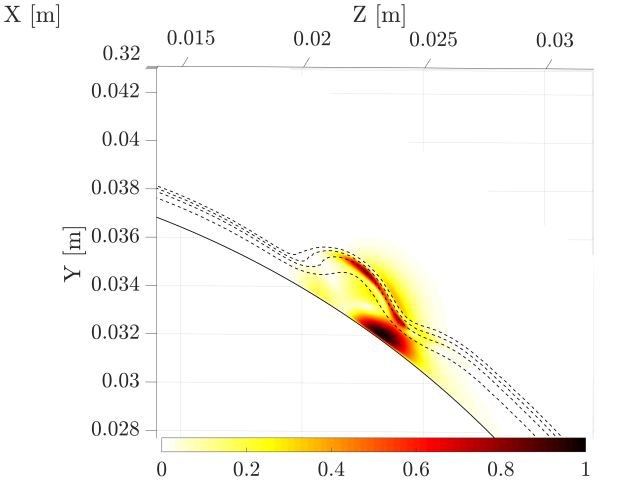

(k) $\left|\check{\hat{u}}_N\right| / \max \left|\check{\hat{u}}_N\right|$ at $X = 0.320$ m.

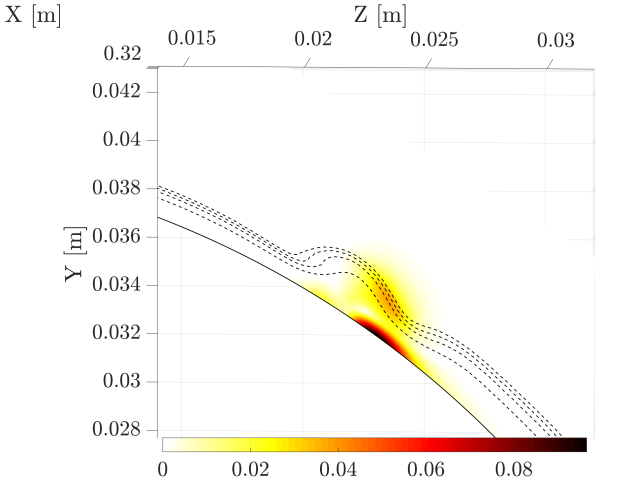

(l) $|\hat{p}| / \max \left|\check{\hat{u}}_N\right|$ at $X = 0.320$ m.

Figure 6.32: Eigenfunctions for $f = 250$ kHz from $X = 0.137$–0.320 m.

highlighted to help explain the shift away from shear-dominated mechanisms.

7. SUMMARY

7.1 Contributions

The goal of this work is to study boundary-layer stability and transition with spatial BiGlobal theory. This technique has continued to mature and has the potential to make regular linear stability analysis of complex vehicles possible. The finned cone is an excellent geometry on which to apply SBG, but it stretches the limits of the current usage. A few clarifications in its application have been addressed.

The difference between the wave vector, the growth vector, and the group-velocity vector have been reemphasized. The N factor for an orthonormal coordinate system has been derived for when group velocity changes as a function of ζ, or when it is constant in ζ but not aligned with ξ. If the in-plane group-velocity component is extracted from an SBG solution, then it can be integrated along a path separate from ξ, decoupling the choice of the two directions.

An SBG solver called BLAST has been explained in detail, with the capability to operate in either surface-based orthogonal coordinates on simple geometries, or generalized nonorthogonal coordinates on more-complex geometries. The use of nonorthogonal coordinates allows decoupling for the choice for $\boldsymbol{a}_\xi$ and the η-ζ surface with respect to a Cartesian reference frame. This capability was used on the finned cone to smoothly vary the minimum $\partial/\partial\xi$ direction from along the vortex to along a ray of the cone when the cone boundary layer becomes axisymmetric. Multiple intricacies of using a nonorthogonal coordinate system have been addressed, including reporting α and c_{ph} in a way that is consistent with orthonormal coordinates, and the translation of common boundary conditions into vector equations and index notation. The solution procedures were described for the initial eigenvalue problem and the convergence routine, along with common behaviors of each. The application of finite differences and the two methods used to deal with numerical difficulties were also described: buffers and filtering. The buffer region is a way to force the solution to ignore its natural response to the basic state in a specific region and has proved

useful to clean up eigenvalue spectra from domains that contain shocks. Filtering is applied when high-wavenumber errors from any number of sources otherwise degrade the accuracy of the solution. It helped damp oscillations in derivatives of the metrics on the fin cone when the Δ between one coordinate is larger than the others, like in ξ. The spectral behavior of the filter in combination with the finite differences was analyzed.

BLAST was verified against incompressible and hypersonic test cases. Plane Poiseuille flow was used to reproduce temporal Orr–Sommerfeld results from the literature. A Mach-10 second mode was reproduced on a flat plate using both orthogonal and nonorthogonal grids. Care was taken to ensure that the nonorthogonal grid case both isolated the nonorthogonal effect without introducing additional discretization error, and remained within n_y and n_z bounds where a converged numerical solution was possible. Excellent agreement was found in all cases and between published results and both coordinate systems within BLAST.

The horseshoe vortex on the finned cone was analyzed at two different unit Reynolds numbers: 6.3 and 5.9×10^6 1/m. At the higher Reynolds number, a grid-convergence study on the basic state was undertaken, showing that the solution was nearing grid-independence at 300 million cells. Stability analysis was undertaken from $X = 0.2$ m to the end of the cone based on the region where the vortex was closer to being in line with a generating line of the cone. A Y-Z plane was intersected with the cone, and the resulting curve was used to make a stability domain that was wall-normal to the cone surface and warped near the fin to be wall-normal to the leading edge. Eigenvalue computations at the back of the cone identified the locally most-unstable mode, which was then marched forward. The most-amplified frequency was found to be 180 kHz, which reached an N factor of 4.5 over the X domain analyzed. The 160–205 kHz band that was most amplified in the SBG results was detected in experiments at a comparable Reynolds number in the correct spatial range on the cone.

Lessons learned from Case I were applied to Case II. The basic-state solution was made more accurate by using axisymmetric solutions upstream of the fin, allowing more points to be concentrated in the 3-D regions. The vortex was extracted in a more-precise manner and used as the basis

for the stability grids instead of the X axis. To facilitate this choice, each stability surface was defined as a plane in Cartesian space, with its normal defined to be parallel to the vortex path at their intersection. In addition, streamwise derivatives of metrics were retained, and the effect of these choices was shown.

One of the main findings of this dissertation was that while the instabilities in question are localized by the vortex, the spatial extent of the solutions are very large. By using a series of different domains on a certain SBG solutions, it was shown that it is very important to include the fin in the accurate computation of instabilities in the cone vortex. The analyses contained within this work are the first spatial BiGlobal computations to include the effect of this type of feature. Further, the azimuthal extent of the solution extends to 130 degrees from the fin in some cases, indicating that the safest way to avoid adverse effects from boundary conditions encroaching on the solution is to allow the stability domain to extend from symmetry plane ($+Y$) to symmetry plane ($-Y$).

A series of instabilities at $X = 0.15$ m were analyzed in depth, and compared with instabilities previously seen in the literature. The development and growth of the most-amplified instability found was analyzed over the length of the vortex. Due to the instability peaking early upstream, becoming more stable downstream, then becoming unstable again still further downstream, some frequencies were calculated from $X = 0.137$–0.387 m and others were only calculated from $X = 0.211$–0.387 m. The frequencies that survived the stable region, between 250 and 390 kHz, achieved early amplification and reached a max N of 5.0 at 250 kHz and $X = 0.340$ m. The lower-frequency band, 100–240 kHz, experienced rapid growth toward the back of the cone. They eventually overtook the 250 kHz mode and the maximum N factor of 5.4 was achieved by $f = 180$ kHz at $X = 0.387$, the last X station computed. However, as in Case I, $f = 160$–200 are all within 0.25 N of each other, indicating that this entire band will experience significant amplification. These results compare well with experiments by Turbeville [72], where a 250 kHz mode is detected first, then overtaken by a 180 kHz mode around $X = 0.33$ m. SBG predicts these two frequencies as being most amplified in their respective regions, and predicts the lower frequency

eventually overtaking the higher frequency. This instability was also observed to change from behaving like a Type-II mode upstream to having second-mode-like characteristics downstream. A possible explanation for the local minimum in growth rate near $X = 0.2$ was offered based on basic-state pressure gradients and vortex development.

7.2 Remaining Challenges

A major challenge remains to be the identification the different families of instabilities. There are prototypical secondary and distorted primary instabilities in the literature, but often the result is found to be some combination of the different categories. Better categories are needed, and methods to place instabilities in these categories; this is crucial to being able to affect the growth of an instability. Post-processing SBG solutions to calculate the perturbation's energy budget is a promising tool in this regard.

Another useful improvement can be made to the SBG problem through a general way to extract the ζ component of group velocity. This will allow application of the general equation for the N factor that was derived earlier. It will also completely decouple the integration path, the direction of ξ, and the orientation of the stability surface.

Finally, converging one SBG solution to the next still requires a significant amount of human oversight. Even with extrapolation and seemingly small steps in frequency or ξ, the mode is often lost. Adaptive techniques are needed to help detect when a mode has been lost and react appropriately, or provide additional "guide rails" to keep the solution from diverging. This must be addressed before SBG use can become more common.

In demonstrating the SBG analysis on the finned cone, it is hoped that further developing best practices for the regular and well-defined use of nonorthogonal grids will allow for broader applicability and insight into stability problems that regularly occur on real-world vehicles. This would then provide engineers with another tool to chip away at the ultimate goal of general boundary-layer-transition prediction and control.

REFERENCES

[1] M. V. Morkovin, E. Reshotko, and T. Herbert, "Transition in open flow systems: A reassessment," *Bulletin of the American Physical Society*, vol. 39, no. 9, p. 1882, 1994.

[2] E. Reshotko, "Transition issues for atmospheric entry," *Journal of Spacecraft and Rockets*, vol. 45, no. 2, pp. 161–164, 2008.

[3] W. S. Saric, R. Carillo, and M. Reibert, "Leading-edge roughness as a transition control mechanism," *AIAA Paper 1998-0871*, 1998.

[4] T. S. Haynes and H. L. Reed, "Simulation of swept-wing vortices using nonlinear parabolized stability equations," *Journal of Fluid Mechanics*, vol. 405, pp. 325–349, 2000.

[5] F. D. Turbeville and S. P. Schneider, "Boundary-layer instability on a slender cone with highly swept fins," *2018 Fluid Dynamics Conference, AIAA Paper 2018-3070*, 2018.

[6] L. M. Mack, "Boundary-layer linear stability theory," Tech. Rep. 709, AGARD, June 1984. Special Course on Stability and Transition of Laminar Flow.

[7] W. S. Saric, E. B. White, and H. L. Reed, "Stability and transition of three-dimensional boundary layers," *Annual Review of Fluid Mechanics*, vol. 35, pp. 413–440, 2003.

[8] W. S. Saric, "Görtler vortices," *Annual Review of Fluid Mechanics*, vol. 26, pp. 379–409, 1994.

[9] A. Fedorov, "Transition and stability of high-speed boundary layers," *Annual Review of Fluid Mechanics*, vol. 43, pp. 79–95, 2011.

[10] H. L. Reed and W. S. Saric, "Transition mechanisms for transport aircraft," *38th Fluid Dynamics Conference & Exhibit, AIAA Paper 2008-3743*, 2008.

[11] H. Deyhle and H. Bippes, "Disturbance growth in an unstable three-dimensional boundary layer and its dependence on environmental conditions," *Journal of Fluid Mechanics*, vol. 316, pp. 73–113, 1996.

[12] E. B. White, W. S. Saric, R. D. Gladden, and P. M. Gabet, "Stages of swept-wing transition," *39th Aerospace Sciences Meeting & Exhibit, AIAA Paper 2001-0271*, 2001.

[13] D. I. A. Poll, "Some observations of the transition process on the windward face of a long yawed cylinder," *Journal of Fluid Mechanics*, vol. 150, pp. 329–356, 1985.

[14] M. R. Malik, F. Li, and C.-L. Chang, "Crossflow disturbances in three-dimensional boundary layers: nonlinear development, wave interaction and secondary instability," *Journal of Fluid Mechanics*, vol. 268, pp. 1–36, 1994.

[15] E. B. White and W. Saric, "Secondary instability of crossflow vortices," *Journal of Fluid Mechanics*, vol. 525, pp. 275–308, 2005.

[16] T. Herbert, "Secondary instability of plane channel flow to subharmonic three-dimensional disturbances," *Physics of Fluids*, vol. 26, no. 4, pp. 871–874, 1983.

[17] S. Balachandar, C. L. Street, and M. R. Malik, "Secondary instability in rotating-disk flow," *Journal of Fluid Mechanics*, vol. 242, pp. 223–347, 1992.

[18] R. T. Pierrehumbert, "Universal short-wave instability of two-dimensional eddies in an inviscid fluid," *Physical Review Letters*, vol. 57, no. 17, pp. 2157–2160, 1986.

[19] V. Theofilis, "Advances in global linear instability analysis of nonparallel and three-dimensional flows," *Progress in Aerospace Sciences*, vol. 39, pp. 249–315, 2003.

[20] V. Theofilis, "Global linear instability," *Annual Review of Fluid Mechanics*, vol. 43, pp. 319–352, 2011.

[21] F. Li and M. M. Choudhari, "Spatially developing secondary instabilities in compressible swept airfoil boundary layers," *Theoretical and Computational Fluid Dynamics*, vol. 25, pp. 65–84, 2011.

[22] M. R. Malik, F. Li, and C.-L. Chang, "Nonlinear crossflow disturbances and secondary instabilities in swept-wing boundary layers," in *Nonlinear Instability and Transition in Three-Dimensional Boundary Layers* (P. W. Duck and P. Hall, eds.), vol. 35 of *Fluid Mechanics and*

its Applications, pp. 257–266, Dordecht, The Netherlands: Kluwer Academic Publishers, 1996.

[23] M. R. Malik, F. Li, M. M. Choudhari, and C.-L. Chang, "Secondary instability of crossflow vortices and swept-wing boundary-layer transition," *Journal of Fluid Mechanics*, vol. 399, pp. 85–115, 1999.

[24] S. A. Craig and W. S. Saric, "Crossflow instability in a hypersonic boundary layer," *Journal of Fluid Mechanics*, vol. 808, pp. 224–244, 2016.

[25] C. A. C. Ward, R. O. Henderson, and S. P. Schneider, "Possible secondary instability of stationary crossflow vortices on an inclined cone at Mach 6," *45th AIAA Fluid Dynamics Conference, AIAA Paper 2015-2773*, 2015.

[26] A. J. Moyes, P. Paredes, T. S. Kocian, and H. L. Reed, "Secondary instability analysis of crossflow on a hypersonic yawed straight circular cone," *Journal of Fluid Mechanics*, vol. 812, pp. 370–397, 2017.

[27] T. S. Kocian, A. J. Moyes, H. L. Reed, S. A. Craig, W. S. Saric, S. P. Schneider, and J. B. Edelman, "Hypersonic crossflow instability," *Journal of Spacecraft and Rockets*, vol. 56, no. 2, pp. 432–446, 2019.

[28] F. Li, M. Choudhari, P. Paredes, and L. Duan, "High-frequency instabilities of stationary crossflow vortices in a hypersonic boundary layer," *Physical Review Fluids*, vol. 1, no. 5, pp. 053603–1–32, 2016.

[29] M. Choudhari, F. Li, P. Paredes, and L. Duan, "Spatially developing secondary instabilities in compressible swept airfoil boundary layers," *Theoretical and Computational Fluid Dynamics*, vol. 36, pp. 181–204, 2022.

[30] M. Choudhari, F. Li, and P. Paredes, "Streak instabilities on HIFiRE-5 elliptic cone," *AIAA SciTech 2020 Forum, AIAA Paper 2020-0828*, 2020.

[31] P. Paredes, R. Gosse, V. Theofilis, and R. Kimmel, "Linear modal instabilities of hypersonic flow over an elliptic cone," *Journal of Fluid Mechanics*, vol. 804, pp. 442–466, 2016.

[32] B. M. Wheaton, D. C. Berridge, T. D. Wolf, R. T. Stevens, , and B. E. McGrath, "Boundary layer transition (BOLT) flight experiment overview," *2018 Fluid Dynamics Conference, AIAA Paper 2018-2892*, 2018.

[33] F. Li, M. Choudhari, and P. Paredes, "Streak instability analysis for BOLT configuration," *AIAA Aviation 2020 Forum, AIAA Paper 2020-3028*, 2020.

[34] X. Chen, S. Dong, G. Tu, X. Yuan, and J. Chen, "Boundary layer transition and linear modal instabilities of hypersonic flow over a lifting body," *Journal of Fluid Mechanics*, vol. 938, pp. A8–1–52, 2022.

[35] F. M. White, *Viscous Fluid Flow*. New York City, NY, USA: McGraw Hill, 3rd ed. ed., 2006.

[36] M. Gaster, "A note on the relation between temporally-increasing and spatially-increasing disturbances in hydrodynamic stability," *Journal of Fluid Mechanics*, vol. 14, no. 2, pp. 222–224, 1962.

[37] A. H. Nayfeh and A. Padhye, "Relation between temporal and spatial stability in three-dimensional flows," *AIAA Journal*, vol. 17, no. 10, pp. 1084–1090, 1979.

[38] A. H. Nayfeh, "Stability of three-dimensional boundary layers," *AIAA Journal*, vol. 18, no. 4, pp. 406–416, 1980.

[39] L. M. Mack, "Boundary-layer stability theory," Tech. Rep. 900-207 Rev. A, Jet Propulsion Laboratory, November 1969.

[40] D. Arnal, "Boundary layer transition: Predictions based on linear theory," *AGARD Report*, vol. 793, no. 2, pp. 1–63, 1994. Special Course on Progress in Transition Modelling.

[41] H. L. Reed, W. S. Saric, and D. Arnal, "Linear stability theory applied to boundary layers," *Annual Review of Fluid Mechanics*, vol. 28, pp. 389–428, 1996.

[42] T. J. Bridges and P. J. Morris, "Differential eigenvalue problems in which the parameter appears nonlinearly," *Journal of Computational Physics*, vol. 55, no. 3, pp. 437–460, 1984.

[43] N. B. Oliviero, T. S. Kocian, A. J. Moyes, and H. L. Reed, "EPIC: NPSE analysis of hypersonic crossflow instability on yawed straight circular cone," *45th AIAA Fluid Dynamics Conference, AIAA Paper 2015-2772*, 2015.

[44] T. S. Kocian, *Computational Hypersonic Boundary-Layer Stability and the Validation and Verification of EPIC*. PhD thesis, Texas A&M University, May 2018.

[45] A. J. Moyes, E. S. Beyak, T. S. Kocian, and H. L. Reed, "Accurate and efficient modeling of boundary-layer instabilities," *AIAA SciTech 2019 Forum, AIAA Paper 2019-1907*, 2019.

[46] R. Aris, *Vectors, Tensors, and the Basic Equations of Fluid Dynamics*. Mineola, NY, USA: Dover Publications, Inc, 1989.

[47] M. R. Malik, "Numerical methods for hypersonic boundary layer stability," *Journal of Computational Physics*, vol. 86, pp. 376–413, 1990.

[48] C. Truesdell, "The physical components of vectors and tensors," *ZAMM - Journal of Applied Mathematics and Mechanics*, vol. 33, no. 10–11, pp. 345–356, 1953.

[49] P. J. Schneider and D. H. Eberly, *Geometric Tools for Computer Graphics*. San Francisco, CA, USA: Morgan Kaufmann Publishers, 2003.

[50] D. H. Eberly, "Least squares fitting of data by linear or quadratic structures." Available at `https://www.geometrictools.com/Documentation/LeastSquaresFitting.pdf` (2021/11/30), July 1999.

[51] A. Riha, M. McMillan, and H. L. Reed, "Linear stability of a boundary-layer vortex on a hypersonic finned cone," *AIAA Aviation 2021 Forum, AIAA Paper 2021-2890*, 2021.

[52] G. B. Whitham, *Linear and Nonlinear Waves*. New York City, NY, USA: John Wiley & Sons, Inc., 1st ed., 1999.

[53] L. Zanus, *Numerical study of chemically reacting hypersonic boundary layers by means of non-linear parabolized stability equations*. PhD thesis, Université Libre de Bruxelles, September 2021.

[54] Y. Saad, "SPARSKIT: a basic tool kit for sparse matrix computations," Tech. Rep. 90.20, Research Institute for Advanced Computer Science, May 1990.

[55] W. E. Arnoldi, "The principle of minimized iterations in the solution of the matrix eigenvalue problem," *Quarterly of Applied Mathematics*, vol. 9, pp. 17–29, April 1951.

[56] Y. Saad, "Variations on Arnoldi's method for computing eigenelements of large unsymmetric matrices," in *Linear Algebra and its Applications* (R. A. Brualdi and H. Schneider, eds.), vol. 34, pp. 269–295, New York City, NY: Elsevier New Holland, Inc., 1980.

[57] P. R. Amestoy, I. S. Duff, J.-Y. L'Excellent, and J. Koster, "A fully asynchronous multifrontal solver using distributed dynamic scheduling," *SIAM Journal on Matrix Analysis and Applications*, vol. 23, no. 1, pp. 15–41, 2001.

[58] E. Anderson, Z. Bai, C. Bischof, S. Blackford, J. Demmel, J. Dongarra, J. Du Croz, A. Greenbaum, S. Hammarling, A. McKenney, and D. Sorensen, *LAPACK Users' Guide*. Philadelphia, PA: Society for Industrial and Applied Mathematics, 3 ed., 1999.

[59] C. J. Roy, "Grid convergence error analysis for mixed-order numerical schemes," *AIAA Journal*, vol. 41, no. 4, pp. 595–604, 2003.

[60] D. V. Gaitonde, J. Shang, and J. Young, "Practical aspects of high-order accurate finite-volume schemes for electromagnetics," *35th AIAA Aerospace Sciences Meeting, AIAA Paper 1997-363*, 1997.

[61] D. V. Gaitonde and M. R. Visbal, "High-order schemes for Navier–Stokes equations: Algorithm and implementation into FDL3DI," Tech. Rep. 1998-3060, Air Force Research Laboratory, August 1998.

[62] M. R. Visbal and D. V. Gaitonde, "High-order-accurate methods for complex unsteady subsonic flows," *AIAA Journal*, vol. 37, pp. 1231–1239, October 1999.

[63] D. V. Gaitonde and M. R. Visbal, "Padé-type higher-order boundary filters for the Navier–Stokes equations," *AIAA Journal*, vol. 38, pp. 2103–2112, November 2000.

[64] L. H. Thomas, "The stability of plane Poiseuille flow," *Physical Review*, vol. 91, no. 4, pp. 780–783, 1953.

[65] S. A. Orzag, "Accurate solution of the Orr–Sommerfeld stability equation," *Journal of Fluid Mechanics*, vol. 50, no. 4, pp. 689–703, 1971.

[66] N. P. Kirchner, "Computational aspects of the spectral Galerkin FEM for the Orr–Sommerfeld equation," *International Journal for Numerical Methods in Fluids*, vol. 32, no. 4, pp. 119–137, 2000.

[67] K. J. Groot, F. Miró Miró, E. S. Beyak, A. J. Moyes, F. Pinna, and H. L. Reed, "DEKAF: spectral multi-regime basic-state solver for boundary layer stability," *2018 Fluid Dynamics Conference, AIAA Paper 2018-3380*, 2018.

[68] S. J. Alter, "A structured-grid quality measure for simulated hypersonic flows," *42nd AIAA Aerospace Sciences Meeting and Exhibit, AIAA Paper 2004-0612*, 2004.

[69] M. R. Visbal and D. V. Gaitonde, "On the use of higher-order finite-difference schemes on curvilinear and deforming meshes," *Journal of Computational Physics*, vol. 181, pp. 115–185, 2002.

[70] F. D. Turbeville and S. P. Schneider, "Transition on a cone with a highly-swept fin at Mach 6," *AIAA Aviation 2019 Forum, AIAA Paper 2019-3217*, 2019.

[71] C. D. Mullen, F. D. Turbeville, H. L. Reed, and S. P. Schneider, "Computational and experimental boundary-layer stability analysis on a hypersonic finned cone," *AIAA SciTech 2019 Forum, AIAA Paper 2019-1381*, 2019.

[72] F. D. Turbeville, *Measurements of Transition Near the Corner Formed by a Highly-Swept Fin and a Cone at Mach 6*. PhD thesis, Purdue University, December 2021.

[73] F. D. Turbeville and S. P. Schneider, "Measurements of instability and transition on a slender cone with a highly-swept fin at Mach 6," *AIAA SciTech 2022 Forum, AIAA Paper 2022-0599*, 2022.

[74] L.-c. E. Steen, "Characterization and development of nozzles for a hypersonic wind tunnel," Master's thesis, Purdue University, West Lafayette, IN, December 2010.

[75] C. D. Mullen, A. Moyes, T. S. Kocian, and H. L. Reed, "Parametric boundary-layer stability analysis on a hypersonic finned circular cone," *2018 Fluid Dynamics Conference, AIAA Paper 2018-3072*, 2018.

[76] A. Knutson, S. Gs, and G. V. Candler, "Direct numerical simulation of Mach 6 flow over a cone with a highly swept fin," *2018 AIAA Aerospace Sciences Meeting, AIAA Paper 2018-0379*, 2018.

[77] C. J. Baker, "The laminar horseshoe vortex," *Journal of Fluid Mechanics*, vol. 95, no. 2, pp. 347–367, 1979.

[78] J. D. Gillerlain Jr., "Fin-cone interference flow field," *17th Aerospace Sciences Meeting, AIAA Paper 1979-200*, 1979.

[79] M. J. Wright, G. V. Candler, and D. Bose, "Data-parallel line relaxation method for the Navier–Stokes equations," *AIAA Journal*, vol. 36, no. 9, pp. 1603–1609, 1998.

[80] M. MacLean and M. Holden, "Validation and comparison of WIND and DPLR results for hypersonic, laminar problems," *42nd AIAA Aerospace Sciences Meeting and Exhibit, AIAA Paper 2004-529*, 2004.

[81] J. L. Steger and R. F. Warming, "Flux vector splitting of the inviscid gasdynamic equations with application to finite-difference methods," *Journal of Computational Physics*, vol. 40, no. 2, pp. 263–293, 1981.

[82] H. C. Yee, "A class of high-resolution explicit and implicit shock-capturing methods," Tech. Rep. Technical Memorandum 101088, NASA Ames Research Center, February 1989.

[83] H. L. Reed, E. Perez, J. Kuehl, T. Kocian, and N. Oliviero, "Verification and validation issues in hypersonic stability and transition," *Journal of Spacecraft and Rockets*, vol. 52, no. 1, pp. 29–37, 2015.

[84] M. M. Peck, D. Mullen, H. L. Reed, F. D. Turbeville, and S. P. Schneider, "Heat flux on a hypersonic cone with a highly swept fin," *Journal of Spacecraft and Rockets*, pp. 1–20, Article in Advance, 2022.

[85] N. Gregory, J. T. Stuart, and W. S. Walker, "On the stability of three-dimensional boundary layers with application to the flow due to a rotating disk," *Philosophical Transactions of the Royal Society of London. Series A, Mathematical and Physical Sciences*, vol. 248, no. 943, pp. 155–199, 1955.

[86] K. J. Groot, *BiGlobal Stability of Shear Flows*. PhD thesis, Delft University of Technology, December 2018.

[87] A. K. Riha, K. J. Groot, A. J. Moyes, and H. L. Reed, "Secondary-instability-mode identification in hypersonic crossflow-dominated boundary layers," *AIAA SciTech 2020 Forum, AIAA Paper 2020-2242*, 2020.

[88] J. M. Patel, "Boundary-layer stability analysis for a yawed cone and a swept, slotted airfoil," Master's thesis, Texas A&M University, College Station, TX, August 2022.

[89] E. S. Beyak, *Transition Physics and Boundary-Layer Stability: Computational Modeling in Compressible Flow*. PhD thesis, Texas A&M University, August 2022.